

LINEAR AND NONLINEAR SPECTROSCOPY OF SELECTED II-VI  
COMPOUND BULK AND QUANTUM  
WELL STRUCTURES

By

JOHN M. HAYS

Bachelor of Science  
Southwest Missouri State University  
Springfield, Missouri  
1987

Submitted to the Faculty of the  
Graduate College of the  
Oklahoma State University  
in partial fulfillment of  
the requirements for  
the Degree of  
DOCTOR OF PHILOSOPHY  
December, 1994

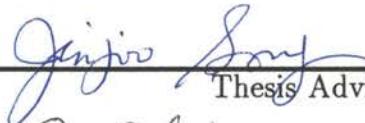
COPYRIGHT  
by


John M. Hays

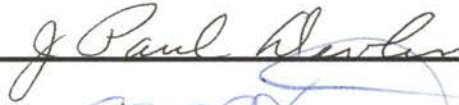
December, 1994

LINEAR AND NONLINEAR SPECTROSCOPY OF SELECTED II-VI  
COMPOUND BULK AND QUANTUM  
WELL STRUCTURES

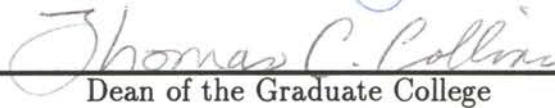
Thesis Approved:

  
\_\_\_\_\_  
Thesis Adviser

  
\_\_\_\_\_

  
\_\_\_\_\_

  
\_\_\_\_\_

  
\_\_\_\_\_  
Dean of the Graduate College

## ACKNOWLEDGEMENTS

It is difficult in this space to express the amount of encouragement and support I have received from various people in my life, although I will attempt the task. Many people whom I have relied upon are not named here, for the list would grow too long to be printed.

My sincerest thanks goes to Dr. Jin-Joo Song, for the opportunity to work in her laboratory. I am grateful for the freedom she gave me to work on many different projects, those which did and those which did not work. I would also like to thank her for her support and contributions to my education, in both theoretical and experimental fields. My committee members, Drs. Bruce J. Ackerson, J. Paul Devlin, and Robert J. Hauenstein are also worthy of my gratitude, for their care and attention. I would like to thank all of the teachers in the physics departments at Oklahoma State University and Southwest Missouri State University; they have always encouraged me in research and in the classroom. Special thanks goes to all of the sample growers whose products I and my co-workers have studied in the last several years. Outstanding in their contributions are Drs. J.F. Schetzina, and J.K. Furdyna, for ZnCdSe/ZnSe quantum wells, Dr. O.K. Wu, for CdTe epilayers, and especially, Mr. Gene Cantwell of Eagle Picher Research Laboratories, for any material we requested. Without these people none of this work would have been possible.

I would also like to express my thanks to all of my co-workers in Dr. Song's laboratory: Arthur Fischer, Theodore Schmitt, Drs. Seon-Ju Hwang, Xiao Hua Yang, Wei Shan, Dai-Sik Kim, John Jacob, Abdellatif Bouchalkha, Jin Fu Zhou, and Pan Sang Jung. I owe them for their explanations and for listening whilst I wondered aloud and explained to myself. More importantly, I owe them for their friendship. I also would like to thank Dr. Wei Shan for the ZnSe:Ga near-gap

PL used in this thesis. Dr. Seon Ju Hwang contributed the envelope function calculations mentioned in Chapter II.

My greatest gratitude is to my family. Thanks to my brothers and sisters who never doubted the wisdom of this endeavor: Bill, Jim, Theresa, Cecilia, Tommy, Cathy, Carolyn, and Susie. As well as being my siblings, they have also been my most constant friends. Thanks to my parents, Jim and June Hays, whose support goes beyond encouragement. They impressed the importance of an education upon me at an early age, and taught me, through their example, that education is a lifelong process.

Lastly, I would like to thank my wife, Dr. Kathy Swallows, whose love and support I cannot find any words to describe. She has been, and is, my love, my companion, and my best friend.

## TABLE OF CONTENTS

Chapter	Page
I. Introduction . . . . .	1
Crystal and band structure of ZnSe and CdTe . . . . .	2
Bulk structure . . . . .	2
Basic Electronic properties . . . . .	4
Quantum Wells . . . . .	9
Optical Transitions . . . . .	14
Bulk materials . . . . .	14
Quantum Wells . . . . .	19
II. Third-order nonlinearities in II-VI compounds. . . . .	27
Introduction . . . . .	27
Theory of third-order processes. . . . .	27
The density matrix formulation . . . . .	27
Two-photon photoluminescence excitation spectroscopy . . . . .	36
Introduction . . . . .	36
Theory of two-photon absorption . . . . .	38
Experimental . . . . .	43
Discussion of results . . . . .	64
Conclusions . . . . .	72
Non-degenerate four-wave mixing spectroscopy . . . . .	73
Single-photon resonances . . . . .	75
Two-photon resonances . . . . .	77
Conclusions . . . . .	80
III. Stimulated emission and gain measurements in CdTe grown by molecular beam epitaxy . . . . .	82
Introduction . . . . .	82
Brief theory . . . . .	82
Experimental . . . . .	86
Stimulated emission studies . . . . .	88
Optical gain measurements . . . . .	98
Conclusions . . . . .	103

Chapter	Page
IV. Photoluminescence of bulk and thin films of ZnSe . . . . .	105
Introduction . . . . .	105
Theoretical . . . . .	106
Experimental . . . . .	111
Crystal growth and sample preparation . . . . .	111
Photoluminescence measurements . . . . .	112
Conclusions . . . . .	127
V. Conclusions . . . . .	131
BIBLIOGRAPHY . . . . .	139

## LIST OF TABLES

Table	Page
I. Periodic part of the Bloch functions for bands of a zinc blende semiconductor near $\vec{k} = 0$ . . . . .	6
II. Relative oscillator strength of the HH, LH and SO band transitions to the conduction band. . . . .	15
III. The results of the binding energy measurements and peak positions of important transitions are summarized. . . . .	68
IV. Samples, growth information, and gain values for the CdTe samples.	87
V. Growth parameters, ionization energies of $I_1$ and net hole concentrations for ZnSe:Li grown on GaAs. . . . .	128



## LIST OF FIGURES

Figure	Page
1. Cubic structure of a zinc blende compound. . . . .	3
2. Representation of the band structure of a zinc blende compound. . . . .	5
3. Schematic representation of a quantum well . . . . .	10
4. The joint density of states for a bulk semiconductor. . . . .	17
5. The joint density of states for a two-dimensional quantum well. . . . .	23
6. Energy resonances which arise from various terms in $\chi^{(3)}$ . . . . .	35
7. Processes which contribute to the two-photon absorption in a QW. . . . .	42
8. Effect of strain on bulk semiconductor band states. . . . .	45
9. Photoluminescence excitation spectroscopy of a quantum well. . . . .	47
10. Two-photon and single-photon photoluminescence excitation spectroscopy system. . . . .	49
11. Single photon photoluminescence and absorption spectra for sample D59. . . . .	50
12. Single photon photoluminescence and absorption spectra for sample D58. . . . .	51
13. PL and absorption spectra for sample D63A. . . . .	52
14. Single photon photoluminescence and reflectance spectra for the 300 Å ZnCdSe QW. . . . .	54
15. Reflectivity and PL data for the $L_z = 500$ Å sample. . . . .	55
16. Single photon PLE and PL spectra for the 2ML CdSe/ZnSe sample. . . . .	56
17. Energy diagram for TP-PLE of a QW. . . . .	58

Figure	Page
18. Two-photon photoluminescence excitation spectrum for sample D59. . . . .	59
19. TP-PLE spectrum of sample D58 with the PL set to the lowest HH exciton. . . . .	61
20. TP-PLE spectrum of sample D58 with the PL set to the highest energy HH exciton. . . . .	62
21. Two-photon photoluminescence spectrum for sample D63A. . . . .	63
22. Two-photon photoluminescence spectrum for the 300 Å QW. . . . .	65
23. Two-photon PLE and reflectance spectra for the 500 Å sample. . . . .	66
24. Photoluminescence and TP-PLE spectra for the 2ML sample. . . . .	67
25. Variation of the exciton binding energy with well width. . . . .	70
26. System diagram for NDFWM spectroscopy. . . . .	74
27. Nondegenerate FWM for CdTe at room temperature and 175 K. . . . .	76
28. The energy diagram for NDFWM in CdTe in the near-infrared regime. . . . .	78
29. The $\chi^{(3)}$ spectrum of ZnSe in the near-infrared. . . . .	79
30. Two-photon resonant spectrum of a ZnCdSe/ZnSe QW. . . . .	81
31. Excitation and stimulated emission for a two-band semiconductor. . . . .	83
32. Side pumping configuration for SE and gain measurement . . . . .	89
33. SE observed in the backscattering direction for sample I. . . . .	90
34. Side-pumping data from a CdTe sample. . . . .	91
35. Semi-log plot of signal intensity -vs- power density for CdTe grown on ZnCdTe. . . . .	93
36. Spectral dependance upon incident power density. . . . .	95
37. Semi-log plot of emission intensity -vs- excitation power density. . . . .	96
38. Power dependance of bulk CdTe. . . . .	97
39. Spectral dependence of SE on excitation length. . . . .	100
40. Intensity dependence of stimulated emission on excitation length. . . . .	101

Figure	Page
41. Intensity dependence of the stimulated emission on excitation length, exhibiting saturation effects. . . . .	102
42. Luminescent transitions in a semiconductor. . . . .	107
43. A typical PL spectrum from as-grown ZnSe. . . . .	114
44. A spectrum of Zn-extracted ZnSe. . . . .	116
45. A spectrum of Se-enriched ZnSe. . . . .	117
46. The PL spectrum from low resistivity ZnSe. . . . .	119
47. The PL spectrum from ZnSe:Cl. . . . .	120
48. Photoluminescence spectra taken from bulk ZnSe:Ga, with 50 ppm Ga. . . . .	122
49. Photoluminescence spectra taken from bulk ZnSe:Ga, with 100 ppm Ga. . . . .	123
50. The PL spectra from undoped ZnSe grown on GaAs. . . . .	124
51. The PL spectra from ZnSe:Li grown on GaAs. . . . .	125
52. The PL spectra from a more highly Li doped ZnSe grown on GaAs. . . . .	126
53. The PL spectrum from ZnSe:Li on GaAs, with a doublet I <sub>1</sub> . . . . .	129
54. Possible phonon scattering mechanisms in a QW. . . . .	133
55. Room temperature absorption and luminescence for a ZnCdSe/ZnSe sample. . . . .	135
56. Two different techniques to observe the polarization selection rules. . . . .	136

## CHAPTER I

### Introduction

Various II-VI compounds have been extensively studied in recent years. The driving force behind this interest has been the possibility of technological devices made from these materials. In particular, ZnSe and CdTe are currently in use in such devices as electro-optic modulators. ZnSe-based quantum wells have also been demonstrated for use in laser diodes in the blue-green region of the spectrum. Diode lasers in the blue-green region are of technological importance due to their applications in higher density optical data storage, communications and displays. For these applications to become reality, however, fundamental knowledge of the basic parameters governing the behavior of these materials is necessary.

Doping of II-VI materials is of critical importance due to the necessity of manufacturing p-n junctions for laser diodes (LD's), light emitting diodes (LED's) or other applications such as electro-optical switches. The defect states which are formed in semiconductors with intentional or unintentional introduction of impurities during the growth process dominate the conductivity of the material. For this reason, the formation and depth of these states are of critical importance both for their physical interest and for device manufacturing.

The nonlinear behavior of these materials is important both for direct application of the nonlinearity and avoidance of losses by such mechanisms as two-photon absorption. Additionally, nonlinear studies can give information which is not available in linear studies. Stimulated emission studies can be used to delineate the various parameters involved in the development of lasers as well as to study the fundamental carrier interactions.

Linear and nonlinear spectroscopic techniques can give complementary information. For example, linear absorption spectroscopy requires that the parity of

the initial and final states of the carriers be different, while two-photon absorption spectroscopy probes those states for which the parity is the same. Further, linear spectroscopy is usually concerned with low power density, and thus for semiconductors, low carrier density. In nonlinear spectroscopy, the carrier densities may reach such levels that the one-electron approximation is no longer applicable. Indeed, in stimulated emission studies, such as are discussed in Chapter III, the carrier densities become such that the population in a given energy range is inverted from the thermal equilibrium situation.

In this study, both linear and nonlinear spectroscopic techniques are employed to study the basic interactions within these material structures. Two-photon spectroscopic techniques are employed to study the electronic structure of bulk ZnSe and ZnSe/Zn<sub>1-x</sub>Cd<sub>x</sub>Se quantum wells, and single-photon resonant nonlinearities are utilized to study CdTe. Stimulated emission spectroscopy is used to study the high carrier density behavior of CdTe, and linear luminescent techniques are utilized to study the doping characteristics of bulk and epilayer ZnSe.

## Crystal and band structure of ZnSe and CdTe

### Bulk structure

ZnSe and CdTe are both zinc blende materials with a direct band gap. The zinc blende structure consists of a diamond-type cubic lattice in which the atoms within the volume (as opposed to those on the surface) of the cube have been replaced with another species. Another way of viewing this structure is as two interpenetrating face-centered cubic crystals of differing species, one with a cube corner at (0,0,0) and the other at  $a/4(1,1,1)$ , where  $a$  is the cubic lattice parameter. This zinc blende structure is shown in Fig. 1. An important point to be noticed is that materials of this structure do not possess inversion symmetry. This point will be an important consideration in later discussions of the nonlinear behavior.

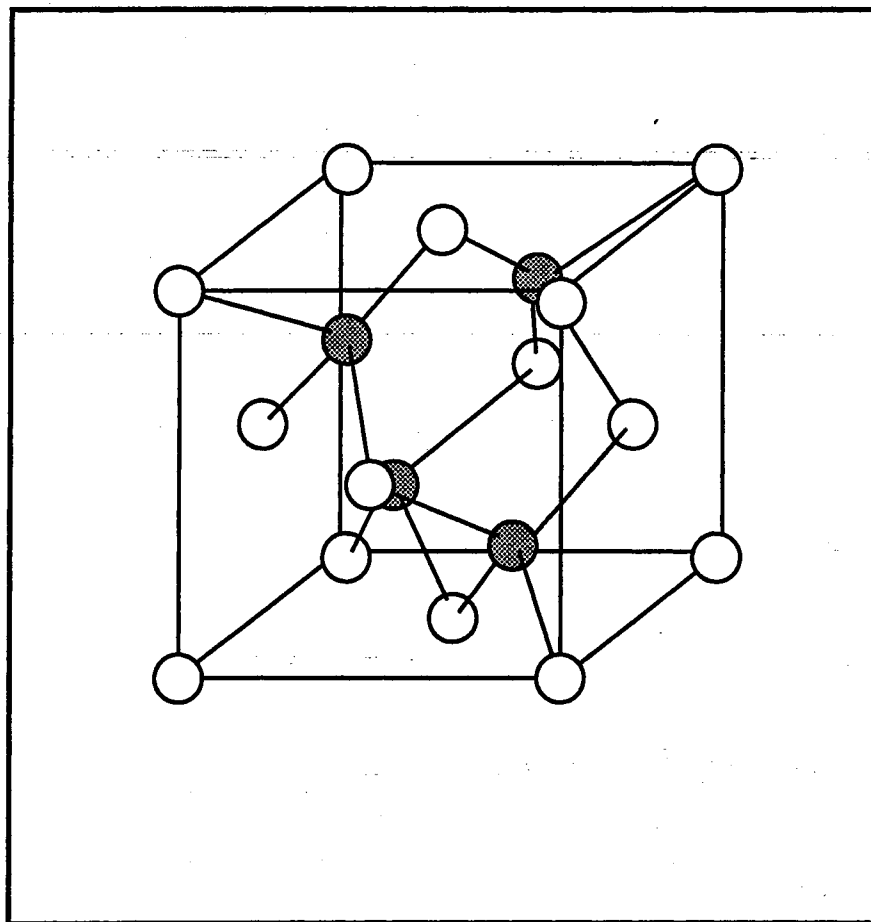


Figure 1. Cubic structure of a zinc blende compound. A zinc blende compound can be pictured as two interpenetrating face-centered cubic lattices. In this figure, the white circles represent atoms of one species and the shaded circles another species.

## Basic Electronic properties

**Band Structure.** The band gap of ZnSe is about 2.8201 eV [1], while that of CdTe is approximately 1.604 eV [2]. The band structure of CdTe and ZnSe bulk materials are quite similar in spite of the large difference in the fundamental gap. Both materials exhibit a direct energy gap and degenerate heavy- and light holes (denoted HH and LH, respectively) at the zone center ( $\vec{k} = 0$ ) and a spin-orbit split-off valence band (SO band) with energy offset  $\Delta$ . The split-off energies are given by  $\Delta = 450$  meV for ZnSe and  $\Delta = 890$  meV for CdTe. [3] The conduction band, heavy- and light hole valence and the split-off valence bands are of symmetry  $\Gamma_6$ ,  $\Gamma_8$ , and  $\Gamma_7$ , respectively [3]. The band structure near the zone center is shown schematically in Fig. 2. More exact band structures have been calculated for bulk CdTe and ZnSe. These band structures are displayed, for example, in Cohen and Chelikowsky [3]. These symmetry designations are those of the double group, which takes into account the degeneracy due to spin. Using  $\vec{k} \cdot \vec{p}$  analysis within the Kane model [4–6], bands of this symmetry allow the periodic part of the Bloch functions ( $u_i$ ), near  $\vec{k} = 0$ , to be written as shown in Table I. The approximate mathematical form of the wavefunctions can be derived using the bond orbital (BO) or the linear combination of atomic orbitals (LCAO) methods. [7,8] Since the primary concerns here are the allowed transitions and their relative strengths, the explicit formulation of the wavefunctions is not necessary.

In Table I, the  $u_{1,2}$  with  $|\frac{1}{2}, \pm\frac{1}{2}\rangle$  are the conduction band,  $u_{3,4}$  with  $|\frac{3}{2}, \pm\frac{1}{2}\rangle$  are the light hole valence band,  $u_{5,6}$  with  $|\frac{3}{2}, \pm\frac{3}{2}\rangle$  are the heavy hole, and  $u_{7,8}$  with  $|\frac{1}{2}, \pm\frac{1}{2}\rangle$ , are the split-off band Bloch functions, respectively. These functions, and the  $\vec{k} \cdot \vec{p}$  analysis from which they are derived, are only valid near the  $\Gamma$  points of the band extrema. The  $S$ ,  $X$ ,  $Y$ , and  $Z$  functions have the symmetry of the atomic  $s$ ,  $p_x$ ,  $p_y$ , and  $p_z$  functions, respectively, under symmetry operations of the tetrahedral group. [4,6,9]

**Excitons.** A factor that is ignored in the foregoing discussion is the Coulombic attraction between the electrons and holes. This attraction can form a bound

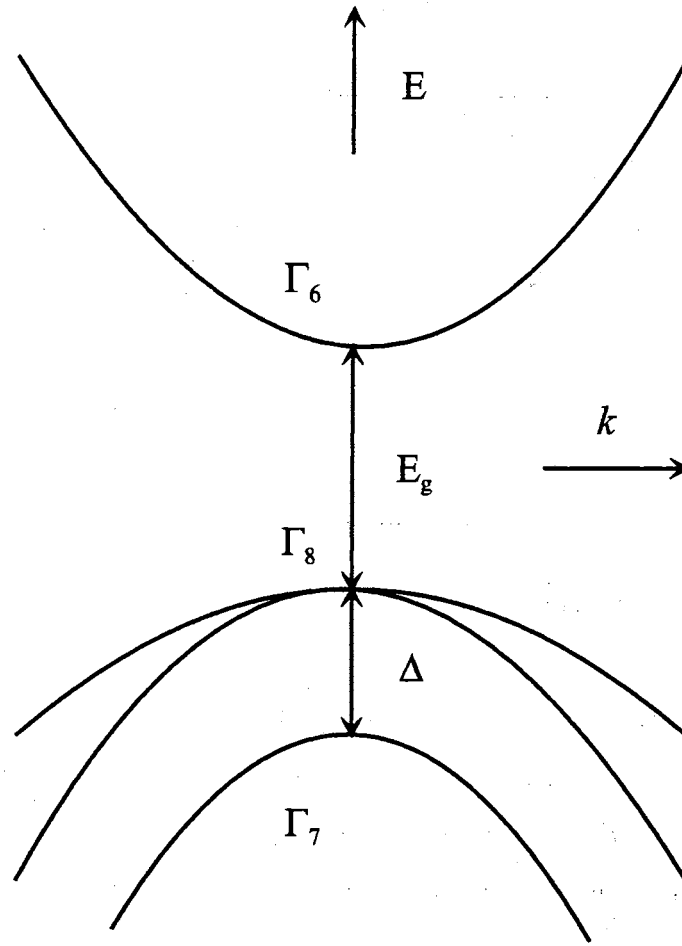


Figure 2. Representation of the band structure of a zinc blende compound near  $\vec{k} = 0$ . The conduction band, heavy and light hole valence and the split-off valence bands are of symmetry  $\Gamma_6$ ,  $\Gamma_8$ , and  $\Gamma_7$ , respectively.



TABLE I.

Periodic part of the Bloch functions for bands of a zinc blende semiconductor  
near  $\vec{k} = 0$ .

Bloch function $u_i$	$ J, m_j\rangle$	$\psi_{J, m_j}$	Band
$u_1$	$ \frac{1}{2}, \frac{1}{2}\rangle$	$i  S \uparrow\rangle$	Conduction
$u_2$	$ \frac{1}{2}, -\frac{1}{2}\rangle$	$i  S \downarrow\rangle$	Conduction
$u_3$	$ \frac{3}{2}, \frac{1}{2}\rangle$	$+\frac{1}{\sqrt{6}}  (X + iY) \downarrow\rangle - \sqrt{\frac{2}{3}}  Z \uparrow\rangle$	Light Hole
$u_4$	$ \frac{3}{2}, -\frac{1}{2}\rangle$	$-\frac{1}{\sqrt{6}}  (X - iY) \uparrow\rangle - \sqrt{\frac{2}{3}}  Z \downarrow\rangle$	Light Hole
$u_5$	$ \frac{3}{2}, \frac{3}{2}\rangle$	$+\frac{1}{\sqrt{2}}  (X + iY) \uparrow\rangle$	Heavy Hole
$u_6$	$ \frac{3}{2}, -\frac{3}{2}\rangle$	$+\frac{1}{\sqrt{2}}  (X - iY) \downarrow\rangle$	Heavy Hole
$u_7$	$ \frac{1}{2}, \frac{1}{2}\rangle$	$+\frac{1}{\sqrt{3}}  (X + iY) \downarrow\rangle + \frac{1}{\sqrt{3}}  Z \uparrow\rangle$	Split-off
$u_8$	$ \frac{1}{2}, -\frac{1}{2}\rangle$	$-\frac{1}{\sqrt{3}}  (X - iY) \uparrow\rangle + \frac{1}{\sqrt{3}}  Z \downarrow\rangle$	Split-off

system which is called an exciton. The similarity between an exciton and an atom of hydrogen or positronium can be exploited to develop an elementary theory of excitons, including their binding and excited state energies. This similarity can be put into more rigorous terms using the envelope function approximation. For the case of spherically symmetric bands near  $\vec{k} = 0$ , the wavefunction for the exciton can be expanded as a sum of direct products of the electron and hole wavefunctions [10–12]:

$$\psi(\vec{r}_e, \vec{r}_h) = \sum_{\vec{k}, \vec{k}'} a_{\vec{k}, \vec{k}'} \psi_{c\vec{k}}(\vec{r}_e) \psi_{v\vec{k}'}(\vec{r}_h). \quad (1)$$

In this equation, the  $\psi_{c\vec{k}}(\vec{r}_e)$  is the wavefunction corresponding to the electron in the conduction band, while the  $\psi_{v\vec{k}'}(\vec{r}_h)$  is the wavefunction corresponding to the hole in the valence band. The Schrödinger equation for the two particle wavefunction is written

$$\left[ -\frac{\hbar}{2m_e^*} \nabla_e^2 - \frac{\hbar}{2m_h^*} \nabla_h^2 + V_C(\vec{r}_e - \vec{r}_h) \right] \psi(\vec{r}_e, \vec{r}_h) = E\psi(\vec{r}_e, \vec{r}_h), \quad (2)$$

where  $V_C$  is the Coulombic potential due to the mutual attraction of the electrons and holes. In the envelope function approximation, the external or applied potential (in this case, the Coulombic potential) is written separately from that potential which is due to the periodicity of the lattice. The external potential is assumed to vary slowly over the unit cell of the material, i.e., much more slowly than the periodic potential of the lattice. With the envelope function defined as

$$\phi(\vec{r}_e, \vec{r}_h) \equiv \frac{1}{\sqrt{Vol}} \sum_{\vec{k}, \vec{k}'} a_{\vec{k}, \vec{k}'} \exp [i(\vec{k} \cdot \vec{r}_e + \vec{k}' \cdot \vec{r}_h)] \quad (3)$$

and  $a_{\vec{k}, \vec{k}'}$  determined by the double Fourier transform

$$a_{\vec{k}, \vec{k}'} = \frac{1}{Vol} \int_{Vol} d\vec{r}_e \int_{Vol} d\vec{r}_h \phi(\vec{r}_e, \vec{r}_h) \exp [i(\vec{k} \cdot \vec{r}_e + \vec{k}' \cdot \vec{r}_h)] \quad (4)$$

The Schrödinger equation for the envelope function then becomes

$$\left[ -\frac{\hbar}{2m_e^*} \nabla_e^2 - \frac{\hbar}{2m_h^*} \nabla_h^2 + V_C(\vec{r}_e - \vec{r}_h) \right] \phi(\vec{r}_e, \vec{r}_h) = (E - E_g)\phi(\vec{r}_e, \vec{r}_h), \quad (5)$$

The Coulombic attraction between the electron and hole may be written

$$V_C(\vec{r}_e - \vec{r}_h) = -\frac{e^2}{\epsilon |\vec{r}_e - \vec{r}_h|}, \quad (6)$$

where  $|\vec{r}_e - \vec{r}_h|$  is the distance between the electron and the hole, and  $\epsilon$  is the (static) dielectric constant of the material.

The system then may be solved as in the hydrogen atom [13], yielding the energy levels [11]

$$E_n = E_g + \frac{\hbar^2 K^2}{2m_T} - \frac{e^4 m_r}{32\pi^2 \epsilon_0^2 \epsilon^2 \hbar^2 n^2}. \quad (7)$$

In the above equation, the energy reference point is taken to be the top of the valence band,  $n$  is the principal quantum number,  $\vec{K}$  is the center of mass momentum vector (with corresponding  $\vec{R}$  center of mass vector), and  $m_r$  ( $m_T$ ) is the reduced mass (total mass) defined as

$$\frac{1}{m_r} = \frac{1}{m_c} + \frac{1}{m_v} \text{ and} \quad (8)$$

$$m_T = m_c + m_v \quad (9)$$

Here,  $m_c$  is the effective mass of the conduction band, while  $m_v$  is the effective mass of the valence band. The effective masses considered here are those near the appropriate band edges, which, for a direct gap material with the gap at  $\vec{k} = 0$ , are the effective masses near  $\vec{k} = 0$ . For a semiconductor with degenerate or near degenerate bands at  $\vec{k} = 0$ , a weighted average effective mass for the valence band may be used, but a more complete description requires consideration of the contributions from the different bands. This complication will not be considered here, since it does not impact the selection rules which are the ultimate goal of this development. Eq. 7 shows that the binding energy of the exciton (that is, the binding energy of the 1s exciton) in this model is  $-e^4 m_r / 32\pi^2 \epsilon_0^2 \epsilon^2 \hbar^2$ .

The envelope functions can also be found, and have the hydrogenic form [12,14]

$$\phi_{Knlm_l}(\vec{R}, \vec{r}) = \frac{1}{\sqrt{V_{ol}}} \exp(i\vec{K} \cdot \vec{R}) R_{nl}(r) Y_l^{m_l}(\theta, \phi). \quad (10)$$

In Eq. 10, the  $R_{nl}(r) Y_l^{m_l}(\theta, \phi)$ 's are the hydrogen wavefunctions with principal quantum number  $n$ , angular momentum  $l$ , and azimuthal quantum number  $m_l$ . The  $R_{nl}(r)$  is the radial function, and the  $Y_l^{m_l}(\theta, \phi)$  are the spherical harmonics. The factor of  $\exp(i\vec{K} \cdot \vec{R})$  denotes plane waves corresponding to the center of mass

motion of the exciton. The wavefunction for the exciton may then be found via the Fourier transform Eq. 3 and Eq. 10 as [15,14]

$$\psi(\vec{r}_e, \vec{r}_h) = \frac{1}{\sqrt{V_{ol}}} u_c(\vec{r}_e) u_v(\vec{r}_h) \phi_{Knlm_l}(\vec{R}, \vec{r}). \quad (11)$$

The success and validity of the envelope function approximation in semiconductors is due to the spatial extent of the electron-hole pair. This spatial extent allows the effective mass approximation to be made. This spatial extent can be approximated by the effective Bohr radius

$$a_H^* = \frac{m\epsilon}{\mu^*\epsilon_0} a_{0H}, \quad (12)$$

where  $a_{0H}$  is the Bohr radius  $4\pi\epsilon_0\hbar^2/me^2 \sim 0.528 \text{ \AA}$ . Another approximation that has been made in the above discussion is that of spherically symmetric bands. Obviously, this is not the case for any real semiconductor. However, for the small values of  $\vec{k}$  which are the most important for the optical properties treated here, this is not a bad approximation.

It should also be noted here that the shallow impurities in semiconductors can be handled in a similar fashion using the envelope function approximation, but with only the conduction (for donors) or valence bands (for acceptors) contributing to the impurity wavefunctions.

## Quantum Wells

Band States. Quantum wells (QW's) can be constructed by growth of two semiconducting materials with dissimilar energy gaps upon one another. The resulting structure will, in general, form wells in both the conduction band and valence bands, as is shown in Fig. 3. As is shown in the figure, the confinement of the carriers produces the well-known quantum mechanical energy levels due to the spatial variation in the potential [13]. The wavefunctions corresponding to these energy levels, however, in difference to the elementary quantum mechanics text situation, are derived from the extant bands in the semiconductor which makes up the well. The difference in energies of the conduction ( $\Delta E_c$ ) and valence ( $\Delta E_v$ )

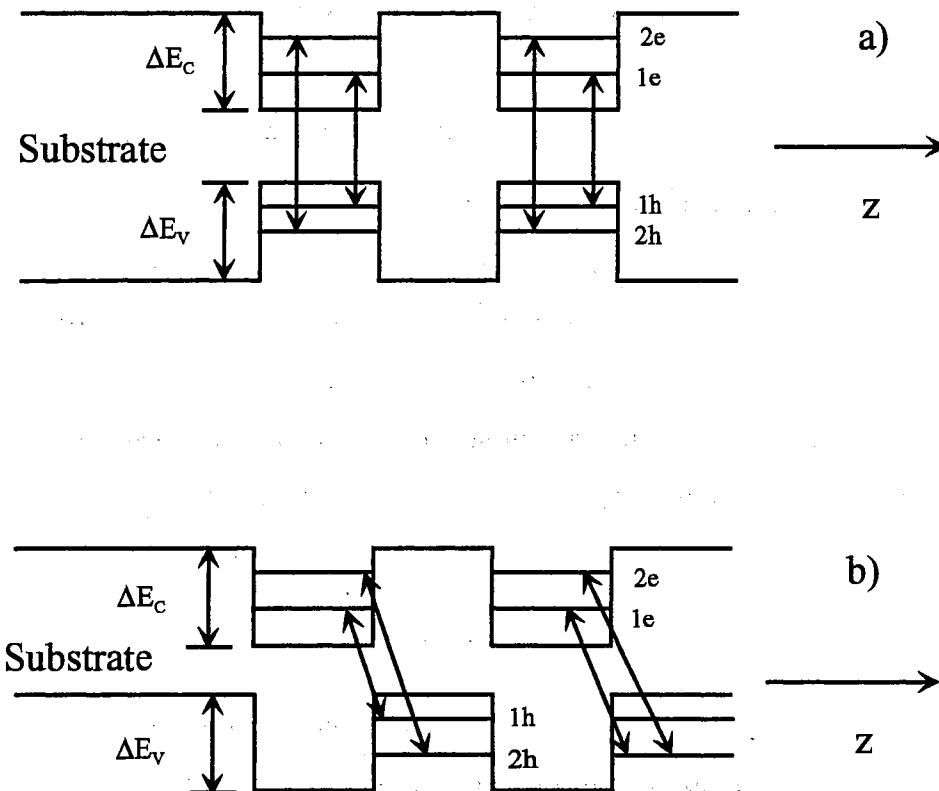


Figure 3. Schematic representation of a semiconductor quantum well. The growth of two semiconducting materials with differing band gaps can form quantum wells in both the conduction and valence bands. A Type I MQW is shown in a), and a Type II in b).

bands of the well and the barrier material is called the band offset as is indicated in Fig. 3. If the layer in which the conduction band minima and the valence band maxima (with respect to the electron energies) occur coincide, as in Fig. 3a, the system is called a Type I QW. If the conduction band minima and the valence band maxima are in different layers, the system is a Type II QW, as is shown in Fig. 3b. Obviously, there will be a tremendous difference in the electronic and optical properties of the two situations. With the electrons and holes spatially separated as in a Type II QW, the optical absorption will be greatly reduced at the lowest energy levels as compared to Type I QW's. In a Type II QW, the exponential tail of the wavefunctions for the electrons and holes dominate the optical properties, while the opposite situation holds for a Type I QW.

The electronic properties of semiconducting quantum wells will be treated here in terms of the envelope function approximation in quantum wells due to Bastard [16,6]. This approximation closely follows the development given above for excitons, and utilizes the same approximations. The wavefunction of a carrier in the quantum well can be written [6]

$$F_n(\vec{r}) = \frac{1}{\sqrt{S}} u_{\nu_n}(\vec{r}) \exp(i\vec{k}_\perp \cdot \vec{r}_\perp) \chi_n(z), \quad (13)$$

where  $u_{\nu_n}(\vec{r})$  is the periodic part of the Bloch functions at the zone center for the particular band ( $\nu_i$ ) from which the QW state arises, and  $\chi_n(z)$  is the envelope function for subband  $n$  in the quantum well. The Bloch functions in the above equation are the functions discussed in the above section on bulk semiconductors. The  $\vec{k}_\perp, \vec{r}_\perp$  are the wave- and position vectors within the plane of the well. Utilizing the effective mass approach, the Schrödinger equation for an electron or hole in a QW can be written [6]

$$\left[ -\frac{\hbar^2}{2m_{e,h}^*} \nabla^2 + V(z) \right] \phi(\vec{r}) = E\phi(\vec{r}). \quad (14)$$

Solutions of this equation are of the form [6]

$$\phi_{n,\vec{k}}(\vec{r}) = \chi_n(z) \exp(i\vec{k}_\perp \cdot \vec{r}_\perp). \quad (15)$$

Substituting this form into Eq. 14 yields the Schrödinger equation for the  $z$ -dependent part  $\chi_n(z)$  [6]:

$$\left[ -\frac{\hbar^2}{2m_{e,h}^*} \frac{d^2}{dz^2} + V(z) \right] \chi_n(z) = \left( E - \frac{\hbar^2 k^2}{2m_{e,h}^*} \right) \chi_n(z). \quad (16)$$

The exact solution for  $\chi_n(z)$  may be difficult depending upon the form of  $V(z)$  assumed. If an infinitely deep well is assumed, the solution is of the simple form found in introductory quantum mechanics texts (see for example, Cohen-Tannoudji [17] or Winter [18]). With the center of the well taken as  $z = 0$  the solutions are of the form [17,18]

$$\chi_n(z) = A \cos \frac{n\pi z}{L_z}, \quad (17)$$

with  $A$  as a normalization constant, and

$$E_n = \frac{\hbar^2}{2m_{e,h}^*} \left( \frac{n\pi}{L_z} \right)^2, \quad n = 1, 2, 3... \quad (18)$$

The equation for the energy (Eq. 18), implies that the heavy and light hole bands, which are degenerate at  $\vec{k} = 0$ , will be split by  $V(z)$  due to the factor of  $m_h^*$  in the denominator. This is indeed the case for real QW's. In fact, it can occur that the HH QW bands are of Type I while the LH bands are Type II. Note also that the energy  $E_n$  is inversely proportional to the square of the well width, so that the "confinement energy" is greater for narrower wells. The infinite well has only even (odd) solutions if the center of the well is taken to be  $z = 0$  ( $z = L_z/2$ ).

For real semiconductor QW's, the infinite well is obviously a very rough approximation. A better solution may be made by substitution of a finite potential well, which unfortunately, requires a graphical or numerical solution to find the allowed energies [19,17,18]. Since the QW is symmetric about the center of the well, the bound states have even or odd solutions within the well of the form [6]

$$\chi_n(z) \sim \cos kz + \sin kz. \quad (19)$$

Since  $V(z)$  is even, then the allowed (stationary) states in the QW will be either even or odd. This well-defined parity of the states in the QW has important repercussions in the optical properties.

Excitons. The case of excitons in QW's is exactly soluble for the limit of a strictly two-dimensional ( $2D$ ) system. [20,21] The appropriate Schrödinger equation to be solved for this situation is

$$-\frac{\hbar}{2\mu_{\perp}} \left( \frac{\partial^2}{\partial^2 x} + \frac{\partial^2}{\partial^2 y} \right) \phi - \frac{e^2}{\epsilon\sqrt{x^2 + y^2}} \phi = E\phi, \quad (20)$$

where the  $\mu_{\perp}$  is the effective (reduced) mass in the plane, and  $x$  and  $y$  are the coordinates in the plane. This equation should be expected to be valid only in the regime in which the effective Bohr radius of the exciton is large relative to the well width [20,21]. This equation can be solved using a method analogous to that used in solving the hydrogen atom. When this is done, the results are

$$E_n = -\frac{Ry}{[(n-1) + 1/2]^2}, \quad n = 1, 2, 3, \dots, \quad (21)$$

with wavefunctions of the form

$$\begin{aligned} \phi_{nm}(\vec{r}) = & \left[ \frac{[(n-1) - |m|]!}{\pi a^2 [(n-1) + 1/2]^3 \{(n + |m|)!\}^3} \right]^2 \\ & \cdot \exp(-\rho/2) \rho^{|m|} L_{(n-1)+|m|}^{2|m|}(\rho) \exp(im\varphi). \end{aligned} \quad (22)$$

In Eq. 21, the  $Ry$  is the exciton Rydberg. In Eq. 22, the  $L_{(n-1)+|m|}^{2|m|}$  are the associated Laguerre polynomials,  $a$  is the effective Bohr radius, and

$$\rho = \frac{r}{a} \lambda, \quad \lambda^{-2} = -\frac{4E}{Ry}. \quad (23)$$

The exciton Rydberg is given by

$$Ry = \frac{\mu e^4}{2\hbar^2 \epsilon^2}. \quad (24)$$

The usage of  $n$  here is consistent with current usage, and differs from that given in Shinada and Sugano and Ralph [20,21]. It should be noted from Eq. 21 that the binding energy of the  $2D$  ( $1s$ ) exciton is four times as great as that in the bulk material.



## Optical Transitions

### Bulk materials

Band-to-band transitions. The primary optical properties of bulk materials are governed by the dipole-dipole transition matrix element between the initial and final states given by

$$\mathbf{p}_{fi} = \langle f | \boldsymbol{\epsilon} \cdot \mathbf{p} | i \rangle, \quad (25)$$

where the  $\mathbf{p}$  is the dipole momentum operator and  $f, i$  are wavefunctions of the Bloch type discussed above. In semiconductors, the dominant absorption feature is that due to electronic transitions from the valence bands to the conduction bands, in which case the above integral is often denoted  $\mathbf{p}_{cv}$  to emphasize the nature of the transition. This arises due to the use of the electric dipole approximation in which the stationary states of the system are perturbed with a potential  $V$ . Within this approximation, the potential is [6]

$$V = \frac{ie\mathcal{E}}{2m_0\omega} \boldsymbol{\epsilon} \cdot \mathbf{p}, \quad (26)$$

where  $\mathcal{E}$  is the magnitude of the electric field.

The non-vanishing matrix elements have been evaluated for the  $S$ ,  $X$ ,  $Y$ , and  $Z$  functions given above in Table I [22]:

$$\langle S | \mathbf{p}_x | X \rangle = \langle S | \mathbf{p}_y | Y \rangle = \langle S | \mathbf{p}_z | Z \rangle \equiv D, \quad (27)$$

where  $\mathbf{p}_x$ ,  $\mathbf{p}_y$ ,  $\mathbf{p}_z$  are the dipole operators in the  $x$ ,  $y$ , and  $z$  directions, respectively. This result follows from 1) the previously mentioned fact that the dipole operator connects states of opposite parity, 2) momentum is conserved, and 3) the spin functions are orthogonal. Using the above, one can then calculate the relative strengths of the various transitions without knowledge of the absolute value of  $D$ . The results are shown in Table II [22].

Obviously, the most fundamental optical measurement in any material is absorption spectroscopy. The absorption coefficient due to band to band transitions for three-dimensional (3D) bulk semiconductors may be written as (see for

TABLE II.

Relative oscillator strength of the HH, LH and SO band transitions to the conduction band near  $\vec{k} = 0$ .

Valence band	Conduction Band	$u_1$	$u_2$
Light hole	$u_3$	$\sqrt{\frac{2}{3}}z$	$-\frac{1}{\sqrt{6}}(x + iy)$
	$u_4$	$\frac{1}{\sqrt{6}}(x - iy)$	$\sqrt{\frac{2}{3}}z$
Heavy hole	$u_5$	$-\frac{1}{\sqrt{2}}(x + iy)$	0
	$u_6$	0	$-\frac{1}{\sqrt{2}}(x - iy)$
Split-off	$u_7$	$-\frac{1}{\sqrt{3}}z$	$-\frac{1}{\sqrt{3}}(x + iy)$
	$u_8$	$-\frac{1}{\sqrt{3}}(x - iy)$	$\frac{1}{\sqrt{3}}z$

example, ref. [11])

$$\alpha = \frac{\pi e^2 |\mathbf{p}_{cv}|^2}{n_0 \epsilon_0 c m^2 \omega} \rho_{cv}(\hbar\omega), \quad (28)$$

where  $\rho_{cv}(\hbar\omega)$  is the joint density of states (JDOS). The joint density of states can be calculated by

$$\rho_{cv}(\hbar\omega) = \frac{2}{8\pi^3} \int_{\text{all } k} d\vec{k} \delta[E_c(\vec{k}) - E_v(\vec{k}) - \hbar\omega]. \quad (29)$$

With the approximation of parabolic bands, the energy of the carriers a function of  $k$  can be written as

$$\begin{aligned} E_c(\vec{k}) &= E_g + \frac{\hbar^2 k^2}{2m_c}, \\ E_v(\vec{k}) &= -\frac{\hbar^2 k^2}{2m_v}, \end{aligned} \quad (30)$$

where the zero of energy is taken to be at the top of the valence band. In the above, the  $m_c$  and  $m_v$  are the effective mass of the electrons and holes, respectively. The argument of the delta function in Eq. 29 can then be written

$$\begin{aligned} E_c(\vec{k}) - E_v(\vec{k}) - \hbar\omega &= E_g + \frac{\hbar^2 k^2}{2} \left( \frac{1}{m_c} + \frac{1}{m_v} \right) - \hbar\omega \\ &= E_g + \frac{\hbar^2 k^2}{2} \frac{1}{m_r} - \hbar\omega. \end{aligned} \quad (31)$$

The joint density of states is then

$$\begin{aligned} \rho_{cv}(\hbar\omega) &= \frac{2}{8\pi^3} \int_0^\infty 4\pi k^2 dk \delta\left[E_g + \frac{\hbar^2 k^2}{2} \frac{1}{m_r} - \hbar\omega\right] \\ &= \frac{m_r}{\pi^2 \hbar^2} \sqrt{\frac{2m_r}{\hbar^2} [\hbar\omega - E_g]}, \end{aligned} \quad (32)$$

which exhibits the much quoted square root dependence upon the incident photon energy. This density of states is shown in Fig. 4, as a solid line. Note that in the above the implicit assumption of vertical transitions is made, as well as ignoring the effects of nonspherical bands.

A comment should be made regarding the type of critical point being considered in the above. Only parabolic, direct, and spherically symmetric bands have been considered in the foregoing calculation. In addition to these critical points, a real semiconductor band structure may have critical points in the form of saddle

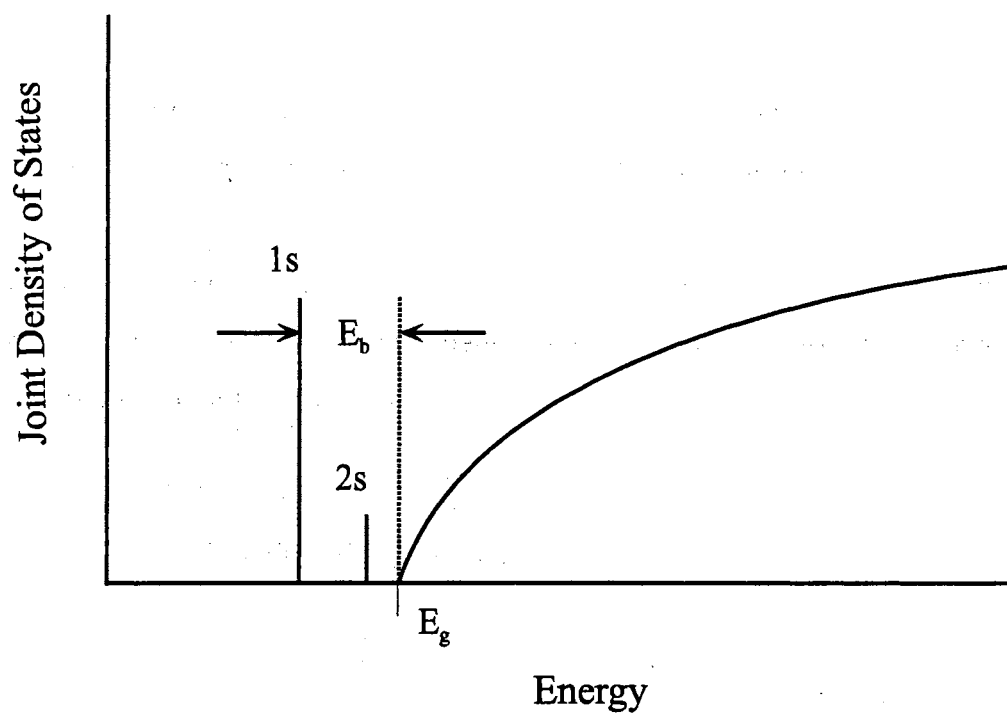


Figure 4. The joint density of states for band-to-band transitions in a bulk semiconductor is indicated by the solid line. The vertical lines at lower energies represent the excitonic states. The binding energy of the  $1s$  exciton is the difference in energy from the band-to-band edge and the exciton state.

points. A further complication can be the enhanced density of states due to nearly parallel conduction and valence bands. Having mentioned this, however, the primary optical features studied in this work are those which derive from the direct gap near  $\vec{k} = 0$ .

Optical properties of excitons. The Coulombic attraction of the electron-hole pair has consequences in the absorption spectra of a semiconductor. To calculate the absorption due to the existence of excitons requires calculation of the matrix element using the dipole moment operator,  $\langle \psi(r_e, r_h) | \epsilon \cdot \mathbf{p} | \psi_v(r_e) \rangle$ . Note that this matrix element poses some conceptual difficulty due to the single particle nature of both the electron state in the valence band and that of the dipole moment operator, while the final state is that of a two particle system. This difficulty is due to the one electron approximation which has been used implicitly in the above. Despite this intrinsic inconsistency in the theory, the one electron approximation has been used in many developments of exciton theory [10,12,11,14] and will be followed here. The matrix element is written using Eq. 11

$$\langle \psi(r_e, r_h) | \epsilon \cdot \mathbf{p} | \psi_v(r_e) \rangle = \int d\vec{r}_e \phi_{Knlm_l}(\vec{R}, \vec{r}) u_c(\vec{r}_e) u_v(\vec{r}_h) \epsilon \cdot \mathbf{p} \psi_v(\vec{r}_e). \quad (33)$$

In the above, the electron is considered to start in the valence band and, through the dipole operator, be excited into the conduction band leaving a hole in the valence band. Using  $\vec{K} = 0$ , i.e., ignoring the photon momentum (and using conservation of momentum), using the one-particle approximation, and assuming that the electron-hole pair are formed at the same position, the matrix element becomes

$$\begin{aligned} \langle \psi(r_e, r_h) | \epsilon \cdot \mathbf{p} | \psi_v(r_e) \rangle &\sim \phi_{Knlm_l}(\vec{R}, 0) \int d\vec{r}_e \psi_c(\vec{r}_e) \epsilon \cdot \mathbf{p} \psi_v(\vec{r}_e) \delta_{K,0} \\ &= \mathbf{p}_{cv} \phi_{Knlm_l}(\vec{R}, 0) \delta_{K,0} \\ &= \sqrt{V} \mathbf{p}_{cv} R_{nl}(r=0) Y_l^{m_l}(\theta, \phi) \delta_{K,0}. \end{aligned} \quad (34)$$

Since only the  $s$ -states of the hydrogenic wavefunctions are nonvanishing at  $\vec{r} = 0$  [23,11,14], this result exhibits the selection rule that only  $s$ -states are observed

in single-photon absorption from the ground state of the crystal or recombination (luminescence) of the exciton.

In addition to the generation of discrete states within the band gap, the mutual attraction between the electrons and holes modifies the above gap absorption. The energy dependent factor by which the absorption is modified is termed the Sommerfeld factor. This may be calculated in a manner similar to the development above for bound states, but allowing  $E > 0$ . For the three dimensional system, this factor goes as [24]

$$S(E - E_g) = \frac{\pi}{\sqrt{R_y/E - E_g}} \frac{\exp(\pi\sqrt{R_y/E - E_g})}{\sinh(\pi\sqrt{R_y/E - E_g})}. \quad (35)$$

The Sommerfeld factor has been excluded in the Fig. 4, although the excitons have been included in the figure.

### Quantum Wells

Band-to-band optical properties. The linear interband absorption of quantum wells are dominated by the  $\Delta n = 0$  (where  $n$  denotes the subband as discussed above) transitions of the heavy hole and light hole excitons. The term intersubband refers to transitions between states which arise from the valence and conduction bands. The  $\Delta n = 0$  rule strictly applies only to the case of infinitely deep QW's and in the electric dipole approximation [25,6,19]. It applies in this case because the parity is well defined with respect to the center of the well. The overlap integral  $\langle \chi_n | \chi_m \rangle$  (where  $\chi_n$  and  $\chi_m$  are the envelope functions for the electrons and holes, respectively) is only nonzero for  $n = m$  for this case.

This is easily demonstrated, for example, in absorption due to interband transitions [6]:

$$\alpha(\omega) = A \sum_{i,f} \left( \frac{1}{m_0} \right) | \epsilon \cdot p_{fi} |^2 \rho_{2D}, \quad (36)$$

with

$$A = \frac{4\pi^2 e^2}{ncm_0\omega Vol}. \quad (37)$$

In the above,  $\epsilon$  is the electric field (polarization) direction and  $Vol$  is the effective sample volume. The term  $\epsilon \cdot \mathbf{p}_{fi}$  is the matrix element of the momentum operator in the direction of the electric field.

Since the envelope functions are slowly varying, the matrix element of the momentum operator may be written [11]

$$\mathbf{p}_{n'n} \cong \int_{Vol} d\vec{r} u_f^*(\vec{r}) \chi_{n'k'}^*(z) \exp(-i\vec{k}'_{\perp} \cdot \vec{r}_{\perp}) (-i\hbar \nabla) u_i(\vec{r}) \chi_{nk}(z) \exp(i\vec{k}_{\perp} \cdot \vec{r}_{\perp}), \quad (38)$$

where  $u_c(\vec{r})$  and  $u_v(\vec{r})$  denote the Bloch functions at the extrema of the conduction and valence band, respectively. Note that the envelope function  $\chi_{nk}(z)$  has no  $x$  or  $y$  dependence, and so is unaffected by dipole operators in these directions. The  $\perp$  symbol on the  $k$  subscript of the envelope function has been dropped for clarity of notation, but it should be remembered that the  $k$  dependence of the envelope function is that parallel to the well.

$$\begin{aligned} \mathbf{p}_{n'n} &\cong \int_{Vol} d\vec{r} \chi_{n'k'}^*(z) \chi_{nk}(z) u_f^*(\vec{r}) (-i\hbar \nabla) u_i(\vec{r}) \\ &\quad + \int_{Vol} d\vec{r} u_f^*(\vec{r}) u_i(\vec{r}) \chi_{n'k'}^*(z) \exp(-i\vec{k}'_{\perp} \cdot \vec{r}_{\perp}) (-i\hbar \nabla) \chi_{nk}(z) \exp(i\vec{k}_{\perp} \cdot \vec{r}_{\perp}) \\ &= \langle \chi_{n'k'}(z) | \chi_{nk}(z) \rangle \langle u_f | \epsilon \cdot \mathbf{p} | u_i \rangle \\ &\quad + \langle u_f | u_i \rangle \langle \chi_{n'k'}(z) \exp(i\vec{k}'_{\perp} \cdot \vec{r}_{\perp}) | \epsilon \cdot \mathbf{p} | \chi_{nk}(z) \exp(i\vec{k}_{\perp} \cdot \vec{r}_{\perp}) \rangle \end{aligned} \quad (39)$$

Since the Bloch function overlap integral  $\langle u_c | u_v \rangle = 0$ , the integral can be written, for interband transitions, (for any polarization direction)

$$p_{n'n} \cong \int_{Vol} d\vec{r} \chi_{n'k'}^*(z) \chi_{nk}(z) u_c^*(\vec{r}) (-i\hbar \nabla) u_v(\vec{r}), \quad (40)$$

Carrying out the integral over the unit cell for the Bloch functions and summing over all unit cells gives

$$p_{n'n} \cong \sum_{\vec{R}} \chi_{n'k'}^*(\vec{R}) \chi_{nk}(\vec{R}) p_{cv} \frac{V_c}{Vol}, \quad (41)$$

which becomes

$$p_{n'n} \cong \frac{p_{cv}}{Vol} \int_{Vol} d\vec{r} \chi_{n'k'}^*(z) \chi_{nk}(z). \quad (42)$$

For infinitely deep QW's,

$$\begin{aligned}
 p_{n'n} &\simeq \frac{p_{cv}}{Vol} \int_{Vol} \cos\left(\frac{n'\pi z}{L}\right) \cos\left(\frac{n\pi z}{L}\right) d\vec{r} \\
 &= p_{cv} \delta_{n'n}
 \end{aligned}
 \tag{43}$$

It should be clear that for an infinitely deep QW  $\Delta n = 0$  or no transition occurs. Since, as is shown in Eq. 42, the dipole moment matrix element for QW's is dependent upon the value of  $\mathbf{p}$  for bulk, the selection rules in Table II hold, with  $z$  the growth axis of the QW. This means that for light polarized perpendicular to  $\hat{z}$ , the growth axis, the HH-e, LH-e, and split-off-e transitions are allowed since both the HH and the LH states have  $|X\rangle$  and  $|Y\rangle$  function dependencies. With the light polarized parallel to  $\hat{z}$ , the LH-e and split-off-e transitions are allowed but the HH-e transition is not. This can be seen from Eq. 27, since the HH states have no  $|Z\rangle$  dependence.

It must be stressed that the above  $\Delta n = 0$  rule strictly holds only for the interband transitions in an infinitely deep, Type I rectangular quantum well, considering only the dipole-dipole interaction. Any deviation from this special case will result in a finite probability of "forbidden" transitions. However, it is also true that the dominant features of finite Type I quantum wells are determined by this selection rule. For these finite Type I QW's, the well-defined parity allows the overlap integral,  $\langle \chi_{nk}(z) | \chi_{n'k}(z) \rangle$ , to be nonzero only for  $n + n'$  even [6].

The joint density of states for quantum wells can be found in a manner analogous to that for bulk semiconductors given above, with

$$E_f = E_g + \frac{\hbar^2 k_{\perp}^2}{2m_{cf}} \tag{44}$$

and

$$E_i = -\frac{\hbar^2 k_{\perp}^2}{2m_{vi}}. \tag{45}$$



The  $k_{\perp}$  denotes the carrier momentum within the plane of the quantum well. Using the above, the 2D density of states may then be written

$$\begin{aligned}
\rho_{2D}(\hbar\omega) &= \frac{2}{4\pi^2} \int_{\text{all } k} d\vec{k} \delta [E_f(\vec{k}) - E_i(\vec{k}) - \hbar\omega] \\
&= \frac{2}{4\pi^2} \int 2\pi k_{\perp} dk_{\perp} \delta \left[ E_g + \frac{\hbar^2 k_{\perp}^2}{2m_r} - \hbar\omega \right] \\
&= \frac{m_r}{\pi \hbar^2}.
\end{aligned} \tag{46}$$

The above density of states holds for each subband  $n$ . We therefore must add the contribution for each subband to find the total density of states at energy  $\hbar\omega$ :

$$\rho_{2D,n}(\hbar\omega) = \frac{m_r}{\pi \hbar^2} \cdot n. \tag{47}$$

This joint density of states is schematically represented in Fig. 5 as the solid line with equal steps. The bulk density of states is also shown in the figure as a dotted curve. The offset from the bulk energy gap is due to the confinement energy of the quantum well. The offset shown in Fig. 5 is due to the confinement of both the electrons and holes in the QW. For simplicity, in the forgoing calculation and in the figure, only one of the hole bands is considered. For a nominally unstrained system such as GaAs/AlGaAs, the lowest energy transitions will be due to the HH band. As will be discussed in Chapter II, this also holds for compressively strained systems. [26]

For the case of intraband transitions, the Bloch function overlap integral in Eq. 39 is  $\langle u_v | u_v \rangle = \langle u_c | u_c \rangle = 1$ , for normalized Bloch functions. In this case, the second term in the sum of Eq. 39 is nonzero and the dipole moment matrix element becomes [6]

$$\begin{aligned}
p_{n'n} &\cong \left\langle \chi_{n'k'}(z) \exp(i\vec{k}'_{\perp} \cdot \vec{r}_{\perp}) \left| \epsilon_x \mathbf{p}_x + \epsilon_y \mathbf{p}_y + \epsilon_z \mathbf{p}_z \right| \chi_{nk}(z) \exp(i\vec{k}_{\perp} \cdot \vec{r}_{\perp}) \right\rangle \\
&= (\epsilon_x \hbar k_x + \epsilon_y \hbar k_y) \langle \chi_{n'k'}(z) | \chi_{nk}(z) \rangle \\
&\quad + \epsilon_z \langle \chi_{n'k'}(z) \exp(i\vec{k}'_{\perp} \cdot \vec{r}_{\perp}) | \mathbf{p}_z | \chi_{nk}(z) \exp(i\vec{k}_{\perp} \cdot \vec{r}_{\perp}) \rangle \\
&= (\epsilon_x \hbar k_x + \epsilon_y \hbar k_y) \delta_{n'n} \delta_{k'k} \\
&\quad + \epsilon_z \langle \chi_{n'k'}(z) | \mathbf{p}_z | \chi_{nk}(z) \rangle \delta_{k'k}
\end{aligned} \tag{48}$$

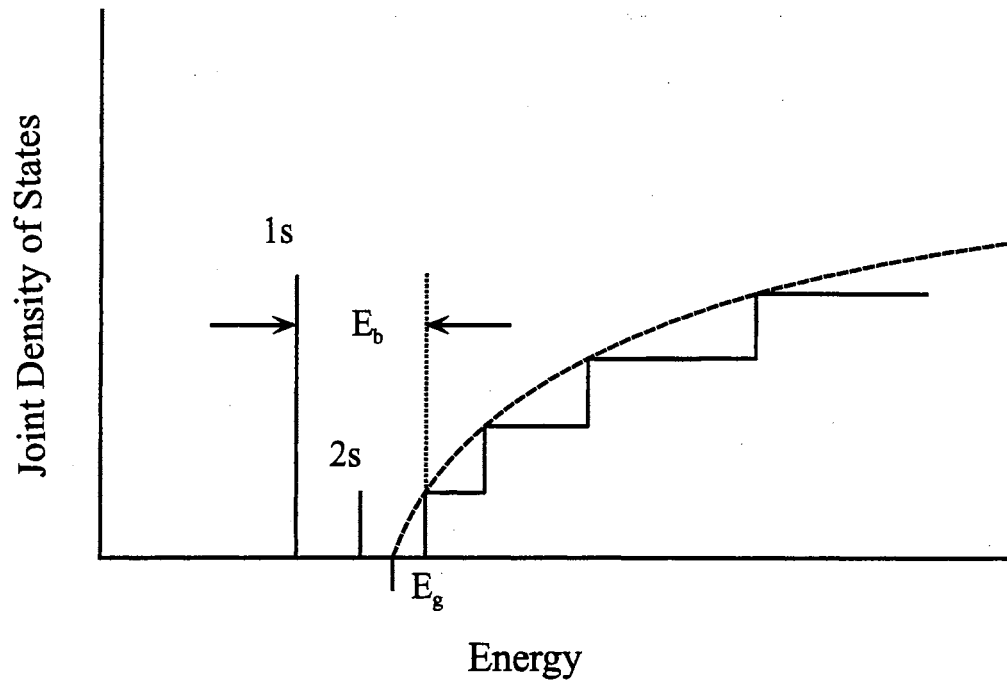


Figure 5. The joint density of states for a two-dimensional quantum well is shown by the solid line with equal steps, while the line with long dashes represents the 3D DOS. The lines at lower energies represent the excitonic states. The binding energy of the 1s exciton is indicated.

Note that for the polarization of the light in the plane of the QW, intraband transitions are only allowed if the initial and final states are coincident, that is, for DC fields. However, these transitions may occur if the momentum can be taken up by defect states or interface roughness in the QW. This type of transitions may also be viewed as being allowed due to the breakdown of the periodicity in  $k$ . The dipole moment for these transitions is directly proportional to  $k_{x,y}$ . For light with a component of the polarization in the well, optical transitions are allowed between subband states with opposite parity, that is, between even and odd envelope functions, and with the same  $k$ .

Consequences of excitons in QW's. As in the bulk case, excitonic effects play a major role in the near-band edge optical properties. In fact, the excitonic features are enhanced in quantum wells due to the confinement of the carriers which allows a greater spatial overlap of the carrier wavefunctions. The interband optical transitions of the excitons in quantum wells follow the same selection rules as discussed above for the bulk case. This can be seen by

$$p_{n'n} \sim \int_{Vol} d\vec{r} \chi_{nk}^{*e}(z) u_c^*(\vec{r}) \phi_{n,m}(\vec{R}, \vec{r}) (-i\hbar \nabla) \chi_{n'k}^h(z) u_v(\vec{r}) \quad (49)$$

which becomes [6]

$$p_{n'n} \sim \langle u_c | \epsilon \cdot \mathbf{p} | u_v \rangle \langle \chi_{nk}^{*e}(z) | \chi_{n'k}^h(z) \rangle \phi_{n,m}(\vec{R}, 0). \quad (50)$$

Thus, all of the selection rules discussed earlier hold, including only the  $s$ -excitons being one photon allowed.

The case of intraband excitonic transitions do not follow directly from the above, however. The treatment of intraband transitions follows as in Eq. 48:

$$\begin{aligned} p_{n'n} &\cong \langle \chi_{n'k'}(z) \exp(i\vec{k}'_{\perp} \cdot \vec{r}_{\perp}) \phi'(x, y) | \epsilon \cdot \mathbf{p} | \chi_{nk}(z) \exp(i\vec{k}_{\perp} \cdot \vec{r}_{\perp}) \phi(x, y) \rangle \\ &= \langle \chi_{n'k'}(z) \exp(i\vec{k}'_{\perp} \cdot \vec{r}_{\perp}) | \epsilon \cdot \mathbf{p} | \chi_{nk}(z) \exp(i\vec{k}_{\perp} \cdot \vec{r}_{\perp}) \rangle \\ &\quad \cdot \langle \phi'(x, y) | \phi(x, y) \rangle \\ &\quad + \langle \chi_{n'k'}(z) \exp(i\vec{k}'_{\perp} \cdot \vec{r}_{\perp}) | \chi_{nk}(z) \exp(i\vec{k}_{\perp} \cdot \vec{r}_{\perp}) \rangle \\ &\quad \cdot \langle \phi'(x, y) | \epsilon \cdot \mathbf{p} | \phi(x, y) \rangle \end{aligned} \quad (51)$$

If the polarization of the light is in the plane of the QW (assume in the  $\hat{x}$  direction for definiteness),

$$\begin{aligned} p_{n'n} &\cong \epsilon_x \hbar k_x \delta_{n'n} \delta_{k'k} \delta_{\phi'\phi} + \langle \chi_{n'k'}(z) | \chi_{nk}(z) \rangle \langle \phi'(x, y) | \epsilon_x \mathbf{p}_x | \phi(x, y) \rangle \\ &= \epsilon_x \hbar k_x \delta_{n'n} \delta_{k'k} \delta_{\phi'\phi} + \langle \phi'(x, y) | \epsilon_x \mathbf{p}_x | \phi(x, y) \rangle \delta_{n'n} \delta_{k'k}, \end{aligned} \quad (52)$$

where, as in the band-to-band case, the first term corresponds to forbidden intra-subband transitions. The second term corresponds to transitions from excitonic states of different parity, e.g.,  $1s$  to  $2p$  exciton transitions within a subband. The dependence upon the overlap of the envelope functions requires that  $\Delta n = 0$  for both terms.

When the polarization of the light is perpendicular to the plane of the QW, the dipole matrix element becomes

$$\begin{aligned} p_{n'n} &\cong \langle \chi_{n'k'}(z) | \epsilon_z \mathbf{p}_z | \chi_{nk}(z) \rangle \langle \phi'(x, y) | \phi(x, y) \rangle \\ &\quad + \langle \chi_{n'k'}(z) | \chi_{nk}(z) \rangle \langle \phi'(x, y) | \epsilon_z \mathbf{p}_z | \phi(x, y) \rangle \\ &= \langle \chi_{n'k'}(z) | \epsilon_z \mathbf{p}_z | \chi_{nk}(z) \rangle \delta_{\phi'\phi} \\ &\quad + \langle \phi'(x, y) | \epsilon_z \mathbf{p}_z | \phi(x, y) \rangle \delta_{n'n} \delta_{k'k} \end{aligned} \quad (53)$$

The first term in the above corresponds to intersubband transitions between envelope functions of different parity, i.e.,  $\Delta n$  is odd. Note that the direct product in this term requires that the excitonic state remain unchanged, so that a  $1s$  exciton remains a  $1s$  exciton. The second term is identically zero if the excitonic wavefunction is assumed to be  $2D$ . If the exciton is allowed to have some  $z$  dependence, then this term does not vanish and is due to forbidden transitions.

As discussed in the bulk case, the above-gap Coulombic attraction cannot be ignored. In the  $2D$  case, the Sommerfeld factor becomes [21,24]

$$S(E - E_g) = \frac{\exp\left(\pi \sqrt{R_y/E - E_g}\right)}{\cosh\left(\pi \sqrt{R_y/E - E_g}\right)}. \quad (54)$$

The additional excitonic structure is shown in Fig.47, as a sharp line at an energy below the onset of interband absorption. Again, the Sommerfeld factor has

been ignored in the JDOS given above. As in bulk materials, the energy difference between the onset of the interband absorption and the appearance of the exciton feature is the  $1s$  exciton binding energy  $E_b^{1s}$ . For a strictly  $2D$  exciton,  $E_b^{1s}$  will be 4 times as great as in the bulk case. The actual value is of theoretical importance in fitting of spectral features in actual semiconductor quantum wells to theory as well as a device parameter pertaining to the thermal stability of the exciton. Thus determining this value is of great importance for a particular QW structure. This point will be discussed in further detail in the next chapter.

## CHAPTER II

### Third-order nonlinearities in II-VI compounds.

#### Introduction

The third-order polarization results in such processes as third-harmonic generation, two-photon absorption, the optical Kerr effect, DC field induced second harmonic generation, four-wave mixing processes, intensity-dependent refractive index effects and many others [11,27]. The material parameter that governs the third-order polarization is the third-order susceptibility,  $\chi^{(3)}$ .

The possibility of using NDFWM and two-photon absorption (or other third-order nonlinear processes) as a spectroscopic technique is due to the resonances found in the various terms contributing to the value of  $\chi^{(3)}$  for a given material system. The derivation of the full expression for  $\chi^{(3)}$  has been covered extensively elsewhere [28–30] and will only be sketched here in order to exhibit the nature of the resonances observed. The development here will be limited to the dipole approximation. Two different viewpoints of the nonlinear polarization will be taken, which, when correlated, yield the microscopic form for the third-order polarization. First, a brief review of the density matrix formulation will be given.

#### Theory of third-order processes.

##### The density matrix formulation

For some arbitrary operator  $\hat{O}$  the expectation value of the operator is given by [11]

$$\langle \hat{O} \rangle = \sum_n p_n \text{Tr} [P(\psi_n) \hat{O}], \quad (55)$$

where  $p_n$  is the probability of the system being in state  $\psi_n$ ,  $Tr [P(\psi_n)\hat{O}]$  is the trace over the resulting elements, and  $P(\psi_n)$  is the projection operator [13,11]:

$$P(\psi)\Phi = [\langle\psi|\Phi\rangle|\psi\rangle]. \quad (56)$$

The expectation value of  $\hat{O}$  can then be written as

$$\langle\hat{O}\rangle = Tr [\hat{\rho}\hat{O}], \quad (57)$$

where  $\hat{\rho}$  is defined by

$$\hat{\rho} \equiv \sum p_n P(\psi_n). \quad (58)$$

The definition in Eq. 58 is sometimes given by the expression  $\hat{\rho} \equiv \overline{|\psi\rangle\langle\psi|}$ , where the overbar represents the ensemble average. The equation of motion for  $\hat{\rho}$  can be simply found by substitution into the Schrödinger equation. The resulting equation is

$$i\hbar\frac{d\hat{\rho}}{dt} = [\hat{H}, \hat{\rho}], \quad (59)$$

where  $\hat{H}$  is the relevant Hamiltonian for the system. It is usually assumed that this Hamiltonian can be written as a sum of the unperturbed Hamiltonian ( $\hat{H}_0$ ), an interaction Hamiltonian ( $\hat{H}_I(t)$ ) and a relaxation Hamiltonian ( $\hat{H}_R(t)$ ), as shown below [11]

$$\hat{H} = \hat{H}_0 + \hat{H}_I(t) + \hat{H}_R(t). \quad (60)$$

As is implied in the above equation, the unperturbed Hamiltonian is assumed to be time independent, allowing stationary states of the system. The equation of motion becomes

$$i\hbar\frac{d\hat{\rho}}{dt} = [\hat{H}_0, \hat{\rho}] + [\hat{H}_I, \hat{\rho}] + [\hat{H}_R, \hat{\rho}]. \quad (61)$$

The relaxation processes are usually handled in a phenomenological way, which leaves the total Hamiltonian as

$$H = H_0 + H_I(t). \quad (62)$$

For a given matrix element  $nm$ , the equation of motion can be written [27]

$$\begin{aligned} i\hbar\dot{\rho}_{nm} &= [H_0, \hat{\rho}]_{nm} + [H_I, \hat{\rho}]_{nm} + \gamma_{nm}\rho_{nm}, \quad n \neq m \\ i\hbar\dot{\rho}_{nn} &= [H_0, \hat{\rho}]_{nn} + [H_I, \hat{\rho}]_{nn} + \sum_{E_m < E_n} \Gamma_{nm}\rho_{mm} - \sum_{E_m < E_n} \Gamma_{mn}\rho_{nn}, \end{aligned} \quad (63)$$

where the  $\gamma_{nm}$  and the  $\Gamma_{nm}$  are the phenomenological transverse and longitudinal relaxation rates, respectively [27,11,31].

The perturbation series may be found by writing the density operator as a power series in  $\hat{H}_I(t)$ :

$$\hat{\rho}(t) = \hat{\rho}^{(0)} + \hat{\rho}^{(1)}(t) + \hat{\rho}^{(2)}(t) + \hat{\rho}^{(3)}(t) + \dots \hat{\rho}^{(n)}(t) \dots, \quad (64)$$

where  $\hat{\rho}^{(0)}$  is given by the equilibrium situation (i.e. no perturbation), while  $\hat{\rho}^{(1)}(t)$  is linear in  $\hat{H}_I(t)$ ,  $\hat{\rho}^{(2)}(t)$  is quadratic in  $\hat{H}_I(t)$ , and so on for the rest of the terms. The above equation is subject to the restrictions that  $\hat{\rho}^{(i)}(-\infty) = 0$  for  $i = 1, 2, 3, \dots, \infty$  [11].

The equation of motion for the individual  $\hat{\rho}^{(i)}$ s is found by plugging into the equation of motion for the density operator, Eq. 63 [27]:

$$\dot{\rho}_{nm}^{(i)} = -(i\Omega_{nm} + \gamma_{nm}) \rho_{nm}^{(i)} - \frac{i}{\hbar} [\hat{H}_I, \hat{\rho}^{(i-1)}(t)]_{nm}. \quad (65)$$

In the above equation,  $\Omega_{nm}$  is the frequency corresponding to the stationary state energy eigenvalue. Assuming solutions of the form  $\rho_{nm}^{(i)} = S_{nm}^{(i)} \exp[-(i\omega_{nm} + \gamma_{nm})t]$ , the solution of the differential equation Eq. 65 is [27,31]

$$\rho_{nm}^{(i)} = -\frac{i}{\hbar} \exp[-(i\Omega_{nm} + \gamma_{nm})t] \int_{-\infty}^t dt' [\hat{H}_I, \hat{\rho}^{(i-1)}(t')]_{nm} \exp(i\Omega_{nm} + \gamma_{nm})t'. \quad (66)$$

Application to dipole transitions. The energy of a dipole in an electric field is given by the interaction Hamiltonian

$$H_I = -\mu \cdot \vec{E}(\vec{r}, t), \quad (67)$$

where the  $\mu = -e\vec{r}$  ( $= \frac{i}{m\omega_0} \nabla$ ) [32] denotes the electric dipole moment operator. The commutator in Eq. 66 is written [27]

$$\begin{aligned} [\hat{H}_I, \hat{\rho}^{(i-1)}(t)]_{nm} &= \sum_{\nu} [\mu_{n\nu} \rho_{\nu m}^{(i-1)}(t) - \rho_{n\nu}^{(i-1)}(t) \mu_{\nu m}] \cdot \vec{E}(\vec{r}, t) \\ &= -(\rho_{mm}^{(i-1)} - \rho_{nn}^{(i-1)}) \mu_{nm} \cdot \vec{E}(\vec{r}, t), \end{aligned} \quad (68)$$



With the electric field written as

$$\vec{E}(\vec{r}, t) = \sum_p \vec{E}(\omega_p) \exp [i(\vec{k}_p \cdot \vec{r} - \omega_p t)], \quad (69)$$

Eq. 66 becomes

$$\begin{aligned} \rho_{nm}^{(i)} &= -\frac{i}{\hbar} \exp [-(i\Omega_{nm} + \gamma_{nm})t] \\ &\cdot \int_{-\infty}^t dt' \left\{ \sum_p -(\rho_{mm}^{(i-1)} - \rho_{nn}^{(i-1)}) \mu_{nm} \cdot \vec{E}(\omega_p) \right. \\ &\cdot \exp i(\vec{k}_p \cdot \vec{r}) \cdot \exp [i(\Omega_{nm} - \omega_p) + \gamma_{nm}]t \left. \right\}. \end{aligned} \quad (70)$$

From this equation, the form of  $\rho_{nm}^{(i)}$  can be seen. Since each integration includes such terms as  $\exp [i(\Omega_{nm} - \omega_p) + \gamma_{nm}]t$ , the resulting  $\rho_{nm}^{(i)}$  will contain such terms as  $((\Omega_{nm} - \omega_p) - i\gamma_{nm})^{-1}$ , for each iteration through the integral for the next higher order (including the factor of  $i$  in this denominator). In each iteration, another field term and frequency will contribute, as will another material resonance frequency. As will be seen below, these factors in  $\rho_{nm}^{(i)}$  become factors in  $\chi^{(i)}$ . It can also be seen that the  $\exp i(\vec{k}_p \cdot \vec{r})$  terms, with successive iterations, will form such terms as  $\exp [i(\vec{k}_p + \vec{k}_q + \vec{k}_r + \dots) \cdot \vec{r}]$ . This factor determines the direction of the emitted wave and the phase matching condition for wave mixing.

The expectation value of the induced dipole moment is given by

$$\langle \hat{\mu}(\vec{r}, t) \rangle = \text{tr}(\rho \hat{\mu}) = \sum_{nm} \rho_{nm} \mu_{mn}. \quad (71)$$

This expectation value may be written as the Fourier series

$$\langle \hat{\mu}(\vec{r}, t) \rangle = \sum_{\sigma} \langle \hat{\mu}(\omega_{\sigma}) \rangle \exp [i(\vec{k} \cdot \vec{r} - \omega_{\sigma} t)], \quad (72)$$

and the total polarization at  $\omega_s$  written (for a system of noninteracting particles with number density  $N$ )

$$\vec{P}(\vec{k}, \omega_{\sigma}) = N \langle \hat{\mu}(\vec{k}, \omega_{\sigma}) \rangle. \quad (73)$$

For third-order effects, terms with frequencies such as  $\omega_1 + \omega_2 + \omega_3$  are of concern. The polarization at this frequency can be written

$$\vec{P}^{(3)}(\vec{k}_1 + \vec{k}_2 + \vec{k}_3, \omega_1 + \omega_2 + \omega_3) = N \langle \hat{\mu}^{(3)}(\omega_1 + \omega_2 + \omega_3) \rangle, \quad (74)$$

with

$$\langle \hat{\mu}^{(3)}(\omega_1 + \omega_2 + \omega_3) \rangle = \sum_{nm} \rho_{nm}^{(3)} \hat{\mu}_{mn}. \quad (75)$$

Classical description of the nonlinear polarization. The total polarization due to the applied electric fields in the limit of sufficiently weak fields may also be written [29,33,11]:

$$\begin{aligned} \vec{P}(\vec{r}, t) = & \int_{-\infty}^{+\infty} \chi^{(1)}(\vec{r} - \vec{r}', t - t') \cdot \vec{E}(\vec{r}', t') d\vec{r}' dt' \\ & + \int_{-\infty}^{+\infty} \chi^{(2)}(\vec{r} - \vec{r}_1, t - t_1; \vec{r} - \vec{r}_2, t - t_2) : \vec{E}(\vec{r}_1, t_1) \vec{E}(\vec{r}_2, t_2) d\vec{r}_{1,2} dt_{1,2} \\ & + \int_{-\infty}^{+\infty} \chi^{(3)}(\vec{r} - \vec{r}_1, t - t_1; \vec{r} - \vec{r}_2, t - t_2; \vec{r} - \vec{r}_3, t - t_3) : \vec{E}(\vec{r}_1, t_1) \\ & \cdot \vec{E}(\vec{r}_2, t_2) \vec{E}(\vec{r}_3, t_3) d\vec{r}_{1,2,3} dt_{1,2,3}, \end{aligned} \quad (76)$$

where the time and spatial integrals are necessary due to the causality condition.

Taking the Fourier transform of the above equation yields the familiar form

$$\vec{P}(\vec{k}, \omega) = \vec{P}^{(1)}(\vec{k}, \omega) + \vec{P}^{(2)}(\vec{k}, \omega) + \vec{P}^{(3)}(\vec{k}, \omega) + \dots \quad (77)$$

where the differing orders of the polarization (linear and nonlinear) are given by

$$\begin{aligned} \vec{P}^{(1)}(\vec{k}, \omega) &= \chi^{(1)}(\vec{k}, \omega) \cdot \vec{E}(\vec{k}, \omega) \\ \vec{P}^{(2)}(\vec{k}, \omega) &= \chi^{(2)}(\vec{k} = \vec{k}_j + \vec{k}_k, \omega = \omega_j + \omega_k) : \vec{E}(\vec{k}_j, \omega_j) \vec{E}(\vec{k}_k, \omega_k) \\ \vec{P}^{(3)}(\vec{k}, \omega) &= \chi^{(3)}(\vec{k} = \vec{k}_j + \vec{k}_k + \vec{k}_l, \omega = \omega_j + \omega_k + \omega_l) \\ &: \vec{E}(\vec{k}_j, \omega_j) \vec{E}(\vec{k}_k, \omega_k) \vec{E}(\vec{k}_l, \omega_l) \\ \vec{P}^{(n)}(\vec{k}, \omega) &= \chi^{(n)}(\vec{k} = \vec{k}_1 + \vec{k}_2 + \dots + \vec{k}_n, \omega = \omega_1 + \omega_2 + \dots + \omega_n) \\ &: \vec{E}(\vec{k}_1, \omega_1) \vec{E}(\vec{k}_2, \omega_2) \dots \vec{E}(\vec{k}_n, \omega_n) \end{aligned} \quad (78)$$

and

$$\begin{aligned}
 \chi^{(n)}(\vec{k} = \vec{k}_1 + \vec{k}_2 + \dots + \vec{k}_n; \\
 \omega_\sigma = \omega_1 + \omega_2 + \dots + \omega_n) &= \int_{-\infty}^{+\infty} \chi^{(n)}(\vec{r} - \vec{r}_1, t - t_1 \dots; \vec{r} - \vec{r}_n, t - t_n) \\
 &\cdot \exp -i[k_1(\vec{r} - \vec{r}_1) - \omega_1(t - t_1) \dots \\
 &\cdot k_n(\vec{r} - \vec{r}_n) - \omega_n(t - t_n)] \\
 &\cdot d\vec{r}_1 dt_1 \dots d\vec{r}_n dt_n.
 \end{aligned} \tag{79}$$

Equating the third-order polarization calculated in the latter formalism and that from the former using Eqs. 74 and 75,  $\chi_{kji}^{(3)}(-\omega_\sigma, \omega_1, \omega_2, \omega_3)$  is found to be [27,11]

$$\begin{aligned}
& \chi_{kjih}^{(3)}(-\omega_\sigma, \\
& \omega_p, \omega_q, \omega_r) = \frac{N}{\hbar^3} \mathcal{P}_I \sum_{vnmI} \rho_{il}^{(o)} \\
& \times \left\{ \frac{\mu_{iv}^k \mu_{vn}^j \mu_{nm}^i \mu_{ml}^h}{[(\Omega_{vl} - \omega_p - \omega_q - \omega_r) - i\gamma_{vl}][(\Omega_{nl} - \omega_p - \omega_q) - i\gamma_{nl}]} \right. \\
& \quad \frac{1}{[(\Omega_{ml} - \omega_p) - i\gamma_{ml}]} \\
& + \frac{\mu_{iv}^h \mu_{vn}^k \mu_{nm}^j \mu_{ml}^i}{[(\Omega_{nv} - \omega_p - \omega_q - \omega_r) - i\gamma_{nv}][(\Omega_{mv} - \omega_p - \omega_q) - i\gamma_{mv}]} \\
& \quad \frac{1}{[(\Omega_{vl} - \omega_p) - i\gamma_{vl}]} \\
& + \frac{\mu_{iv}^i \mu_{vn}^k \mu_{nm}^j \mu_{ml}^h}{[(\Omega_{nv} - \omega_p - \omega_q - \omega_r) - i\gamma_{nv}][(\Omega_{vm} - \omega_p - \omega_q) - i\gamma_{vm}]} \\
& \quad \frac{1}{[(\Omega_{ml} - \omega_p) - i\gamma_{ml}]} \\
& + \frac{\mu_{iv}^h \mu_{vn}^i \mu_{nm}^k \mu_{ml}^j}{[(\Omega_{mv} - \omega_p - \omega_q - \omega_r) - i\gamma_{nv}][(\Omega_{nl} - \omega_p - \omega_q) - i\gamma_{mv}]} \\
& \quad \frac{1}{[(\Omega_{vl} - \omega_p) - i\gamma_{vl}]} \\
& + \frac{\mu_{iv}^j \mu_{vn}^k \mu_{nm}^i \mu_{ml}^h}{[(\Omega_{vn} - \omega_p - \omega_q - \omega_r) - i\gamma_{vn}][(\Omega_{nl} - \omega_p - \omega_q) - i\gamma_{nl}]} \\
& \quad \frac{1}{[(\Omega_{ml} - \omega_p) - i\gamma_{ml}]} \\
& + \frac{\mu_{iv}^h \mu_{vn}^j \mu_{nm}^k \mu_{ml}^i}{[(\Omega_{nm} - \omega_p - \omega_q - \omega_r) - i\gamma_{nm}][(\Omega_{mv} - \omega_p - \omega_q) - i\gamma_{mv}]} \\
& \quad \frac{1}{[(\Omega_{vl} - \omega_p) - i\gamma_{vl}]} \\
& + \frac{\mu_{iv}^i \mu_{vn}^j \mu_{nm}^k \mu_{ml}^h}{[(\Omega_{nm} - \omega_p - \omega_q - \omega_r) - i\gamma_{nm}][(\Omega_{vm} - \omega_p - \omega_q) - i\gamma_{vm}]} \\
& \quad \frac{1}{[(\Omega_{ml} - \omega_p) - i\gamma_{ml}]} \\
& + \left. \frac{\mu_{iv}^h \mu_{vn}^i \mu_{nm}^j \mu_{ml}^k}{[(\Omega_{ml} - \omega_p - \omega_q - \omega_r) - i\gamma_{ml}][(\Omega_{nl} - \omega_p - \omega_q) - i\gamma_{nl}]} \right\} \cdot \frac{1}{[(\Omega_{vl} - \omega_p) - i\gamma_{vl}]} \}. \tag{80}
\end{aligned}$$

This formula shows that there are distinct resonances in the spectra of  $\chi^{(3)}$  due to the various terms in the denominator. The resonances which are relevant to this work are the single-photon, two-photon and Raman-type resonances as is illustrated in Fig. 6. In Fig. 6a, a two-photon resonance is illustrated by the two solid lines, denoting real states,  $\alpha$  and  $\delta$ . Additionally, if the dotted lines denoted  $\beta$  and  $\gamma$  correspond to real rather than virtual states, single photon (incoming and outgoing, respectively) resonances may also occur. A Raman-type resonance is illustrated in Fig. 6b. The real Raman mode (which may also be a Raman-type electronic resonance) is denoted  $\Omega$ . For this situation single-photon resonances may also occur when either of the states  $\gamma$  or  $\delta$  correspond to real states. For both situations discussed above, multiple resonances may occur, i.e., any of the higher lying states may be real or more than one may be real. These possibilities must be considered in examining the nonlinear spectra.

The argument of  $\chi_{kjih}^{(3)}(-\omega_\sigma, \omega_p, \omega_q, \omega_r)$  shows that the third-order nonlinear susceptibility is a function of four frequencies, three input frequencies and one generated frequency. This should be compared with the linear susceptibility, which is a function of the input frequency. The tensor nature of  $\chi^{(3)}$  also cannot be ignored. Because of this tensorial property, the direction of polarization of the input beams and the orientation of the material must be considered in the interpretation of the nonlinear spectra. This inherent directional property of  $\chi^{(3)}$  also leads to specific transition selection rules for a given material. [34,35]

It should also be noted that the general form of  $\chi^{(3)}$  is complex, so that, as in the linear susceptibility, the third-order susceptibility has both real and imaginary parts. These real and imaginary parts correspond to the dispersive and absorptive components of the susceptibility, respectively. [27]

In the general formulation, there are 48 terms in the expression for  $\chi^{(3)}$ . These terms have been explicitly calculated by Bloembergen *et al.*, using the perturbation technique outlined above [28] and by Prior, utilizing a diagrammatic technique [30]. In Eq. 80, these 48 terms may be found by the use of the permutation operator

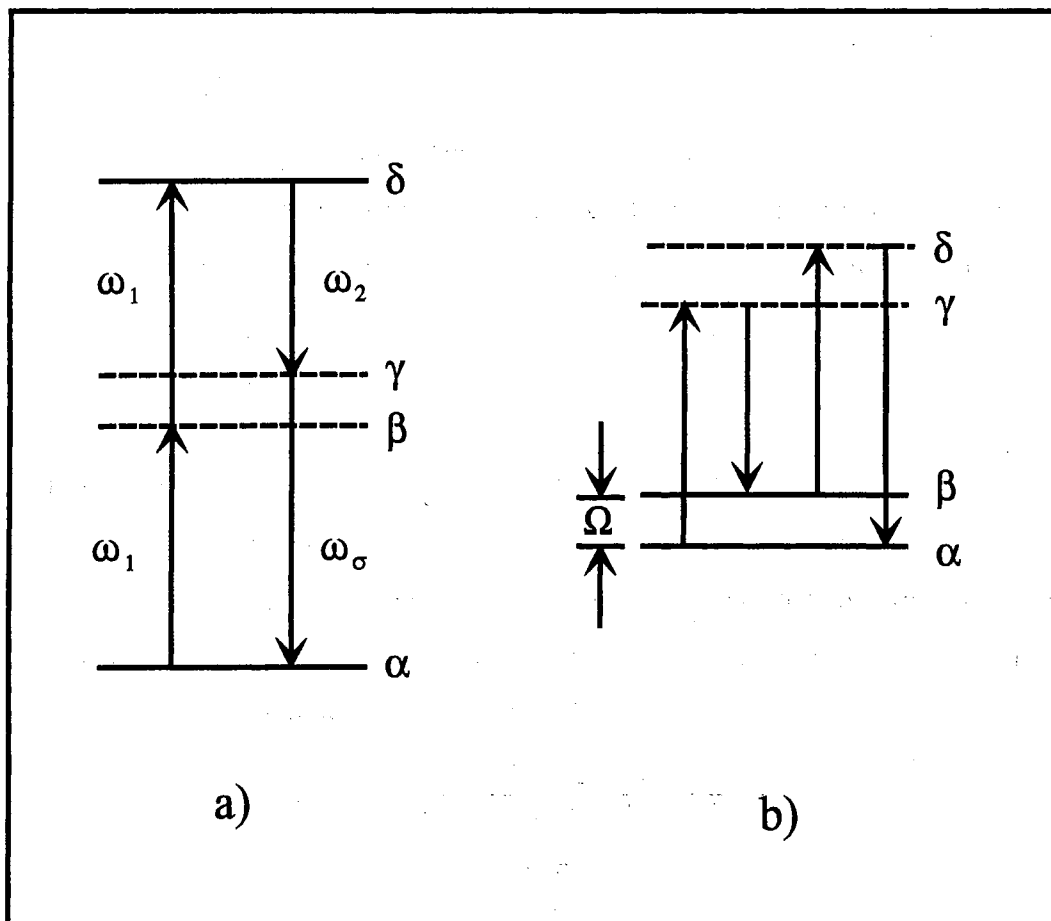


Figure 6. Energy resonances which arise from various terms in  $\chi^{(3)}$ . In a), single- and two-photon resonances are possible, both incoming and outgoing. In b), a Raman type resonance is illustrated. All of these resonances are observed in NDFWM spectroscopy.

$\mathcal{P}_I$ . This operator expands the above expression by permuting the electric fields; six permutations of eight terms for a total of 48. [27]

## Two-photon photoluminescence excitation spectroscopy

### Introduction

The nonlinear properties of QW's have been studied extensively. However, most of these studies have concentrated on the saturation of the excitonic absorption with an intense pump. [36–38] Few studies have been performed on the two-photon absorption (TPA) of QW states, primarily in GaAs/AlGaAs QW's. [39–43] Recently, one group has reported TPA spectra of ZnSe/ZnSeS QW's. [44] No known observations of TPA in ZnCdSe/ZnSe QW's have been reported.

The importance of  $\text{Zn}_{1-x}\text{Cd}_x\text{Se}/\text{ZnSe}$  QW's to blue lasing has been proven [45–47]. However, much of the fundamental information on this system is as yet not known. For example, the exciton binding energy (i.e., the binding energy of the lowest energy  $1s$  exciton, as discussed in Chapter I) in these materials has not yet been unambiguously determined. The exciton binding energy in quantum well structures (QW's) is an important parameter both for device applications and for fitting the observed spectra to theory.

The  $1s$  exciton binding energy of ZnSe of about 20 meV is comparable to  $k_B T = 25$  meV at room temperature (for GaAs  $E_b^{1s} = 4.2$  meV [48]). This leads to the expectation that substantial populations of the  $1s$  exciton may exist at room temperature, leading to room temperature devices based on the exciton effect. However, this line of reasoning ignores the strong coupling of the excitons (as well as electrons and holes) in II-VI compounds with the longitudinal optical (LO) phonons. This coupling may be described as a linewidth broadening. This broadening is expressed as [49]

$$\Gamma(T) = \Gamma_R + \gamma_{Ac}T + \frac{\Gamma_{LO}}{\exp(\hbar\omega_{LO}/k_B T) - 1}, \quad (81)$$

where  $\Gamma_R$  is the residual broadening due to scattering from impurities or interfaces,  $\gamma_{Ac}$  is the acoustic exciton-acoustic phonon coupling constant,  $\Gamma_{LO}$  is the exciton-LO phonon coupling constant. In Eq. 81,  $\omega_{LO}$  is the LO phonon frequency. The coupling constant  $\Gamma_{LO}$  determined for epilayers of ZnSe grown on GaAs is 80 meV [50], which should be compared with the corresponding value for bulk GaAs of 14 meV [51]. This rather high value of  $\Gamma_{LO}$  means that the population of excitons in ZnSe is depleted at higher temperatures by disassociation of the excitons into electrons and holes. This process may be pictured as the absorption of an LO phonon by an exciton. Since the 1s exciton binding energy is less than the LO phonon energy, the exciton will disassociate.

For device applications, it has been considered important to increase the 1s exciton binding energy in II-VI compound semiconductors beyond the longitudinal optical (LO) phonon energy of 30.7 meV. As noted in the preceding chapter, one way of increasing the binding energy of the exciton is in a QW potential. This creates a quasi-2D exciton, increasing the binding energy. Additionally, in an alloy well the LO phonon energy may also be shifted slightly from the bulk value. The LO phonon energy may be increased or decreased or the alloy may support two modes arising from the two constituent sublattices, as is the case for AlGaAs materials. For the case of ZnCdSe, the LO phonon energy is increased from the bulk ZnSe value, and the material shows single mode behavior. [52]

The two-photon selection rules for quantum wells allows the observation of the 2p excitonic states with  $\Delta n = 0$  and the corresponding continuum states when the electric field polarization of the incident light is in the plane of the well [53,39,54,40,55-57]. This information, in conjunction with determination of the energy position of the 1HH-1e 1s exciton ( $E_{1hh-1e}^{1s}$ ), which can be determined using linear absorption spectroscopy, or similar technique, yields the exciton binding energy directly. With the electric field polarization perpendicular to the plane of the well, the relevant selection rule is  $\Delta n \neq 0$  for the LH-e transitions and the associated s-state excitons [53,39,54,40,55-57].



## Theory of two-photon absorption

The basic theory governing the allowed transitions in QW's in the linear regime has been covered in the preceding chapter. Recall that, for single photon transitions, the  $\Delta n = 0$  transition rule holds for interband transitions, that is, transitions between conduction and valence band states. For intraband transitions, however, the allowed transitions are such that  $\Delta n \neq 0$  (intersubband transitions), with the light polarized perpendicular to the plane of the well. If the light is polarized in the plane of the well, defects must take up the momentum to allow transitions within a subband. [6]

The theory of two-photon transitions has been treated for many years, beginning with Göppert-Mayer in 1931 [58]. Despite this early beginning, the first experimental observation of two-photon absorption by Kaiser and Garrett [59] had to await the development of intense laser sources. Two-photon transitions in condensed matter have been studied theoretically by several groups, using different theoretical models. The primary differences in these theories has been the way that the virtual intermediate states are handled. Both Loudon [60] and Braunstein [61] considered a three band model with the intermediate band distinct from the initial and final bands. Mahan has emphasized the contribution due to intermediate states arising from either the initial or final bands [53]. Lee and Fan, however, have developed a more comprehensive theory which includes the contributions from the initial and final bands as well as remote bands [62]. Loudon, Mahan, and Lee and Fan also incorporate the Coulombic attraction (exciton effect) between the generated carriers into their models.

The absorption from a field of frequency  $\omega_1$  due to the presence of another field of frequency  $\omega_2$  is given by [63,62]

$$\beta(\omega_1) = \frac{\pi^2 e^4 \mathcal{E}_2}{c n_1 m^4 \omega_1 \omega_2^2} \sum_f \left| \sum_I \left( \frac{p_{cI}^{(2)} p_{Iv}^{(1)}}{E_I - E_v - \hbar\omega_1} + \frac{p_{cI}^{(1)} p_{Iv}^{(2)}}{E_I - E_v - \hbar\omega_2} \right) \right|^2 \delta(E_f - E_i - \hbar\omega_1 - \hbar\omega_2), \quad (82)$$

where  $n_1$  is the index of refraction at  $\omega_1$ ,  $\mathcal{E}_2$  is the electric field at frequency  $\omega_2$ , and the second summation is over all states (intermediate states  $I$ ) within the constraints of the two or three band model. This can occur in two-photon absorption since the intermediate state is virtual, i.e., energy and conservation may be violated in the two virtual transitions. As can be seen from the individual matrix elements, the  $\vec{k}$  values must be conserved in each transition. In the resulting final state of the electron-hole pair, energy and momentum must be conserved. The factors  $p_{cI}^{(2)} p_{Iv}^{(1)}$  are written in analogy to the dipole transition matrix element exhibited in Chapter I:

$$p_{cI}^{(2)} p_{Iv}^{(1)} = \langle c | \epsilon_2 \cdot \mathbf{p} | I \rangle \langle I | \epsilon_1 \cdot \mathbf{p} | v \rangle, \quad (83)$$

where  $\epsilon_1$  ( $\epsilon_2$ ) is the polarization direction for the field at frequency  $\omega_1$  ( $\omega_2$ ), and  $\mathbf{p}$  is the dipole moment operator. As above,  $|v\rangle$  and  $|c\rangle$  are the initial valence band state and the final conduction band state, respectively. In this work, the primary concern is the two-photon absorption from a single beam. In this case, the absorption becomes [62]

$$\beta(\omega) = \frac{2\pi^2 e^4}{cn_1 m^4 \omega} \sum_f \left| \sum_I \left( \frac{\epsilon \cdot p_{cI} \epsilon \cdot p_{Iv}}{E_I - E_v - \hbar\omega} \right) \right|^2 \cdot \delta(E_c - E_v - 2\hbar\omega). \quad (84)$$

The selection rules for two-photon absorption may thus be determined from the terms  $\langle c | \epsilon \cdot \mathbf{p} | I \rangle$  and  $\langle I | \epsilon \cdot \mathbf{p} | v \rangle$ , for single photon transitions. For the bulk, band-to-band case, Table II of Chapter I gives the relative oscillator strengths of the various transitions near  $\vec{k} = 0$ . The similarity of Eq. 84 and the form of the various terms in  $\chi^{(3)}$  should be noted. With the appropriate substitutions for the relevant frequencies, it can be seen that [64]

$$\beta(\omega) = \frac{8\pi\omega}{n^2 c^2} \text{Im}(\chi^{(3)}). \quad (85)$$

Examination of the matrix elements for band-to-band transitions would lead to the expectation that this transition would be forbidden due to parity. The two-photon absorption includes terms such as

$$\beta(\omega) \sim |\langle c | \epsilon \cdot \mathbf{p} | I \rangle \langle I | \epsilon \cdot \mathbf{p} | v \rangle|^2. \quad (86)$$

The intermediate states can be either in the valence band or the conduction band. Then, the TPA will be consist of terms such as

$$\beta(\omega) \sim |\langle S | \epsilon \cdot \mathbf{p} | S \rangle \langle S | \epsilon \cdot \mathbf{p} | v \rangle|^2. \quad (87)$$

Note that the factor on the left is zero because of the parity of the states is identical. A factor that has been ignored here, however, is that the states may not have a well defined parity. Near  $\vec{k} = 0$  the states are defined as given in Chapter I. Away from  $\vec{k} = 0$ , the parity is not well defined. This will cause the TPA to become nonzero for a band-to-band transition.

The selection rules for two-photon transitions to excitons in bulk is easily demonstrated by considering the dipole matrix element for single photon absorption and creation of an (intermediate state) exciton as calculated in Chapter I,

$$\langle \psi_I(r_e, r_h) | \epsilon \cdot \mathbf{p} | \psi_v(r_e) \rangle \sim \sqrt{Vol} \mathbf{p}_{cv} R_{nl}(r=0) Y_l^{m_l}(\theta, \phi) \delta_{K,0}, \quad (88)$$

which allows for the creation of only *s*-states of the excitons. As is well known [23,63], the single-photon transitions of hydrogen from *s*-states are to *p*-states. Thus, two-photon excitonic absorption in bulk materials results in the creation of a *p*-state exciton.

Two-photon transitions in QW's have also been considered, with the theories primarily based upon the results and techniques of the bulk theories cited above. Most of these theories have been based upon the two-band model of Mahan. [53] However, these theories have the additional complication of the generation of subband states due to the QW potential. Again, as in the bulk case, an intermediate virtual state is created in which energy is not necessarily (generally, is not) conserved. With the two-photon absorption given similar to that in Eq. 84, the proper selection rules may be determined directly from the single photon case. The promotion into a virtual state is just as in the single photon case, for either intra- or interband transitions (except as noted above, that the energy need not be conserved). Transitions from this virtual state are then dependent upon the other type of transition momentum matrix element, i.e., if the initial transition is

intraband, the second is interband. Note that both types contribute to  $\beta(\omega)$ . If the polarization of the light is in the plane ( $\epsilon \perp \hat{z}$ , with  $\hat{z}$  the growth axis), the  $\Delta n = 0$  transition rule holds, since as discussed in Chapter I, light of this polarization does not induce transitions between subbands, that is,  $n$  does not change. The band-to-band selection rules for two-photon absorption of a light beam with the polarization vector in the plane of the well is then just as it is for single photon absorption, i.e.,  $\Delta n = 0$ . [54–57,40,39] This situation is shown in Fig. 7a. Additionally, due to the linear dependence of the intraband absorption on  $k$  (again, see Chapter I), the two-photon absorption increases linearly with  $2\hbar\omega - E_g$  (where  $E_g$  denotes the onset of the absorption) [54,40,39] for each  $n$ .

The description given above can be shown mathematically considering terms in the TPA coefficient for a QW subband-subband transition for the electric field along the  $x$  direction, and using the inter- and intra-subband matrix elements derived in Chapter I:

$$\beta(\omega) \sim \left| (\hbar k_x \langle \chi_{nk} | \chi_{n'k'} \rangle) \left( \langle \chi_{n'k'}^e | \chi_{nk}^h \rangle \langle u_c | - i\hbar \nabla_x | u_v \rangle \right) \right|^2 \quad (89)$$

where the polarization is assumed to be in the  $x$  direction. In the above equation, the first factor is due to the intrasubband transitions and the last factor due to interband transitions. This illustrates that the subband-to-subband selection rules for TPA with  $\epsilon \perp \hat{z}$  are as for single photon absorption, since intrasubband transitions do not change  $n$ .

If the light polarization is along the growth direction ( $\epsilon \parallel \hat{z}$ ), the relevant rule for single photon intraband absorption is  $\Delta n$  odd (Chapter I). Combining this with the second transition, the two-photon selection rule for light polarized perpendicular to the plane of the QW is  $\Delta n$  odd [54–57,40,39]. This is seen by

$$\beta(\omega) \sim \left| \left( \langle \chi_{nk}(z) | - i\hbar \nabla_z | \chi_{n'k'}(z) \rangle \right) \left( \langle \chi_{n'k'}(z) | \chi_{nk}(z) \rangle \langle u_c | - i\hbar \nabla_z | u_v \rangle \right) \right|^2 \quad (90)$$

The factor on the right again describes interband transitions, with  $\Delta n = 0$ . The factor on the left (intersubband transitions) requires that the envelope functions differ in parity, so that  $\Delta n$  must be odd. Transitions which contribute to the

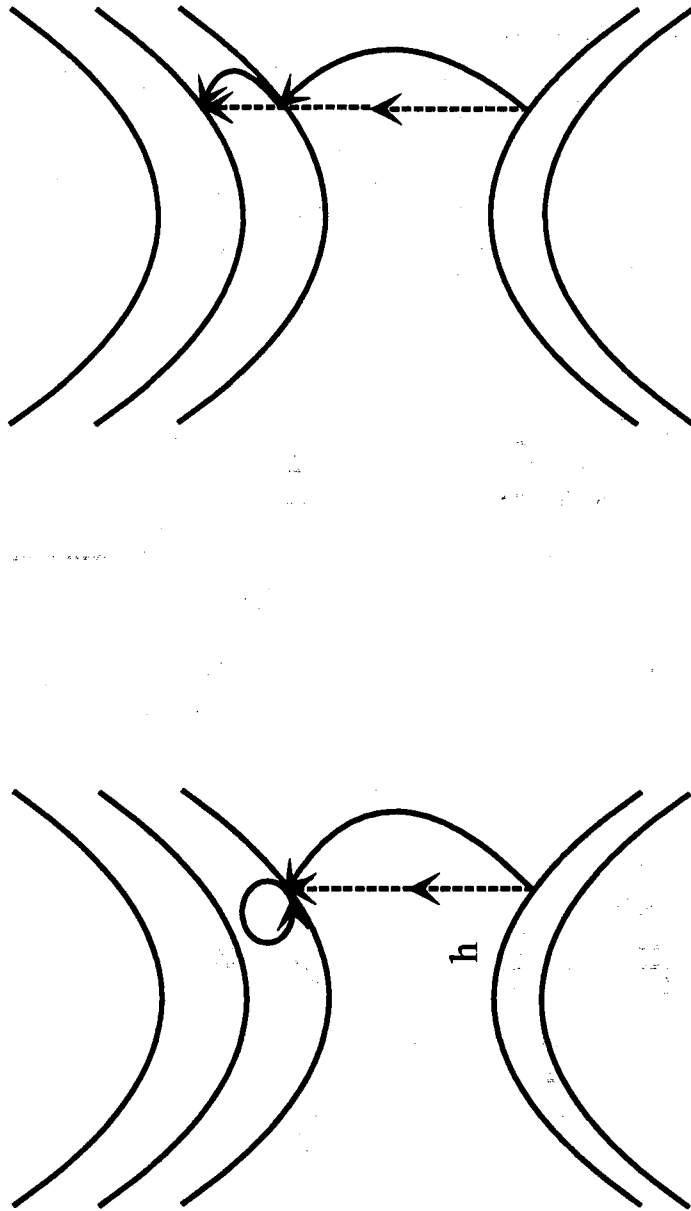


Figure 7. Processes which contribute to the two-photon absorption in a QW. In a), intrasubband absorption contributes to the absorption with the polarization in the plane of the well. The intersubband contributions with the polarization perpendicular to the well are shown in b).

TPA for this polarization are shown in Fig. 7b. Note that light polarized in this direction exhibits a shift in the absorption edge to higher energy compared to that observed in linear spectroscopy or for TPA the polarization in the plane of the well.

The selection rules for excitons in QW's may be determined by considering the intraband and interband matrix elements including the exciton effect. Using the results from Chapter I for intra- and inter-band matrix elements,

$$\begin{aligned} \beta(\omega) \sim & |(\hbar k_{x,y} \langle \chi_{n'k'}(z) | \chi_{nk}(z) \rangle \delta_{\phi'\phi} \\ & + \langle \chi_{n'k'}(z) | \chi_{nk}(z) \rangle \langle \phi'(x,y) | -ih\nabla_{x,y} | \phi_s(x,y) \rangle) \\ & \cdot (\langle \chi_{n'k'}(z) | \chi_{nk}(z) \rangle \phi_s(x,y) \langle u_c | -ih\nabla_{x,y} | u_v \rangle)|^2. \end{aligned} \quad (91)$$

The first term in the top line is small for excitonic transitions due to the limited extent of the excitons in  $k$  space, and allows for TPA of  $s$ -excitons in this polarization. The second, and dominant, term requires the exciton to change parity and allows only  $p$ -excitons to be observed.

If the polarization of the electric field is allowed to be parallel to  $z$ , the TPA includes such terms as

$$\begin{aligned} \beta(\omega) \sim & |(\langle \chi_{n'k'}(z) | -ih\nabla_z | \chi_{nk}(z) \rangle \delta_{\phi'\phi} \\ & + \langle \chi_{n'k'}(z) | \chi_{nk}(z) \rangle \langle \phi'(x,y) | -ih\nabla_z | \phi_s(x,y) \rangle) \\ & \cdot (\langle \chi_{n'k'}(z) | \chi_{nk}(z) \rangle \phi_s(x,y) \langle u_c | -ih\nabla_z | u_v \rangle)|^2. \end{aligned} \quad (92)$$

Recall that for  $E||z$ , the HH-e interband transition is forbidden (see Chapter I and Ref. [65]), so that only the LH states contribute to the TPA. If the  $u_v$  in the last line of Eq. 92 is a HH state,  $\beta$  is zero. This occurs because the LH (HH) states (do not) include the  $|Z\rangle$  function. The first term in Eq. 92 allows the  $s$ -excitons to contribute to the TPA. The second term in the first line, is zero if the excitons are  $2D$ .

## Experimental

The samples in this study were of three different types. The first were  $\text{Zn}_{1-x}\text{Cd}_x\text{Se}/\text{ZnSe}$  MQW's grown on ZnSe grown at North Carolina State by J.F.

Schetzina. These wells of these samples were all 50 Å wide and the  $x$ -values were between 10 and 15%. The larger Cd concentration ( $x$ ) decreases the band gap of the alloy in this structure. The band gap of the alloy may be found by the empirical formula [66]

$$E_g = 2.825 - 1.39x + 0.35x^2 \text{ (eV)}, \quad (93)$$

while the lattice constant of the alloy may be found by

$$a = 5.6676 + 0.3824x \text{ (Å)}. \quad (94)$$

The second set of samples were also  $\text{Zn}_{1-x}\text{Cd}_x\text{Se}/\text{ZnSe}$  MQW's, but grown by J.K. Furdyna on GaAs. The well thicknesses of these samples were 300 and 500 Å. A third type of sample was constructed of a two monolayer (2ML) single quantum well (SQW) of CdSe with ZnSe barriers grown on GaAs. [67] This CdSe/ZnSe SQW was grown at Hiroshima University by Z.Q. Zhu and T. Yao. All of the samples were grown in the (100) crystal direction.

In the  $\text{ZnCdSe}/\text{ZnSe}$  material system, the wells are under compressive strain due to the lattice constant difference between the alloy wells and the ZnSe barriers. This compressive strain causes the HH band to be pushed up with respect to the LH band (considering electron energies), decreasing the transition energy. [52] If the material were under tensile strain, the LH band could be above the HH band. This situation is shown in Fig. 8 [26] for bulk (or bulk-like epilayer) materials. However, this latter statement ignores the QW potential which increases the LH *subband* energy. For the  $\text{ZnCdSe}/\text{ZnSe}$  material system in this study, however, the primary results of this strain is to increase (decrease) the HH (LH) confinement energy and shift the LO phonon energy slightly. [52] Pelekanos *et al.* quote an increase in the LO phonon energy of about 1 meV for a  $\text{Zn}_{1-x}\text{Cd}_x\text{Se}/\text{ZnSe}$  with  $x = 0.25$  and  $L_w = 30$  Å. The QW's in this sample should exhibit less of an LO phonon shift due to the lower values of  $x$ . [52]

As was mentioned in the introduction of Chapter I, linear and nonlinear spectroscopic techniques are complimentary, giving different information. In order

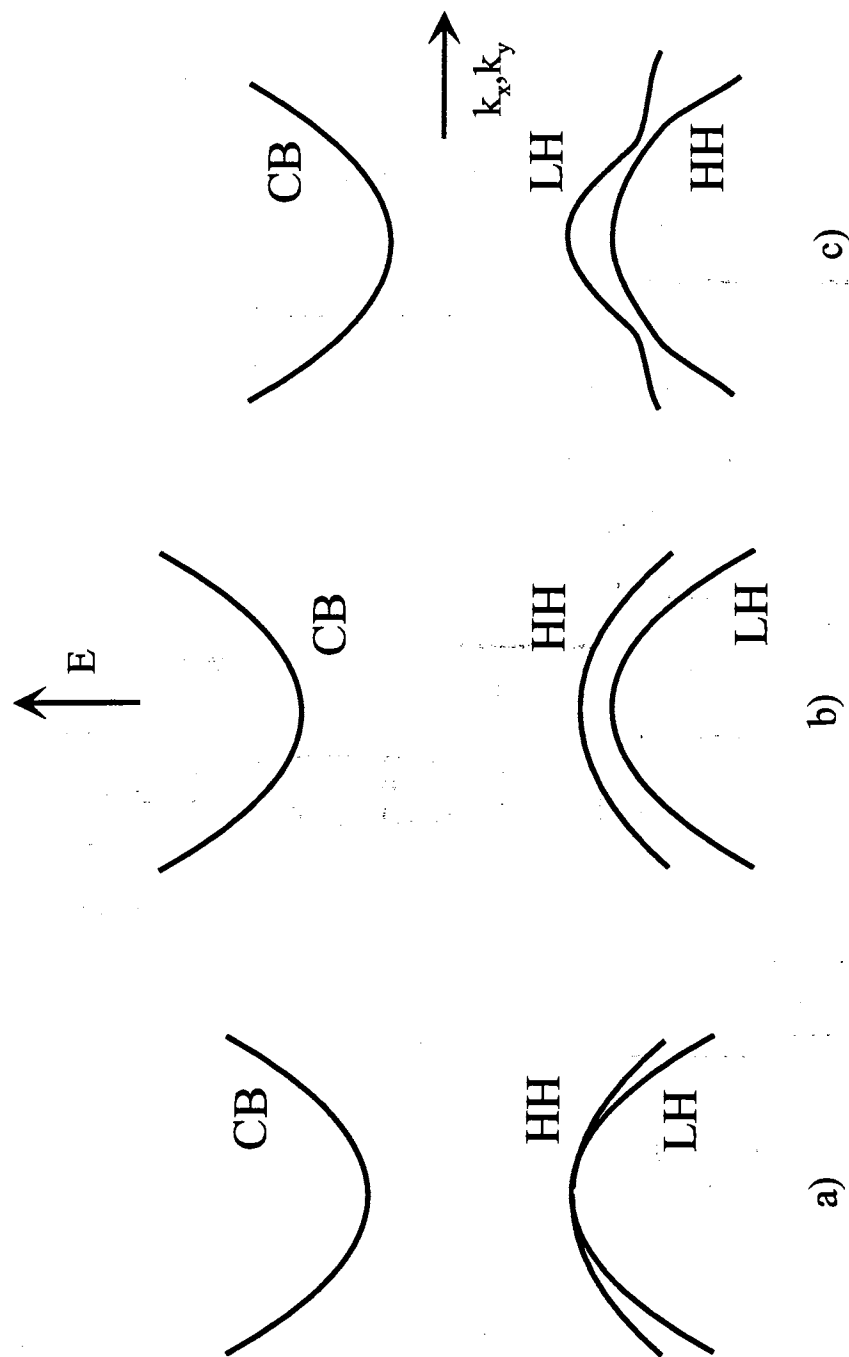


Figure 8. Effect of strain on bulk semiconductor band states is shown for a) unstrained b) compressive and c) tensile strain. Under compressive strain, the HH states are lowered, while under tensile strain the LH states are lowered. After People and Jackson.



to understand the TP-PLE spectra of these materials, the linear behavior must also be studied.

The linear absorption spectroscopy follows the selection rules determined in Chapter I, so that the 1HH-1e, 1s exciton (often referred to as the  $n = 1$  heavy hole exciton and denoted 1HHx) is usually the lowest energy state observed, then the 1LH-1e, 1s exciton, then the  $n = 2$  exciton states, and so on. The subband-to-subband transitions also contribute to the absorption, but distinct peaks are not seen. This is the reason that SP-absorption or SP-PLE usually cannot determine the binding energy of the exciton: the onset of the subband transitions are obscured by the strong excitonic transitions.

Photoluminescence excitation spectroscopy is performed by detection of a specific emission line (PL) from a sample, and then observing the variation of the emission intensity as a function of excitation energy. This is schematically illustrated for the case of single-photon photoluminescence spectroscopy (SP-PLE) in Fig. 9. As indicated in the figure, the light is absorbed according to the selection rules discussed in Chapter I. The carriers then relax to the  $n = 1$  states and recombine, emitting the light which is collected and detected. A sketch of the resulting spectra is shown in Fig. 9b, with the various excitonic transitions indicated. The Stokes' shift shown on the diagram is the shift in energy from the  $E_{1hh-1e}^{1s}$  PL peak and the PLE (or absorption) peak from the same transition. The observation of the Stokes' shift is usually taken to be an indication of inhomogeneous broadening in the sample. [68] This is often used as a qualitative measure of the quality of a QW sample. TP-PLE produces a similar type of spectra, but the different selection rules in combination with the values of the matrix elements modifies the resulting spectra.

Linear spectroscopy of  $Zn_{1-x}Cd_xSe/ZnSe$  QW's. Photoluminescence of the samples was obtained using a HeCd laser (10 mW) operating at 325 nm as an excitation source. The PL was collected and dispersed using a 0.85 m double spectrometer (SPEX 1403). The detection system was a GaAs photomultiplier

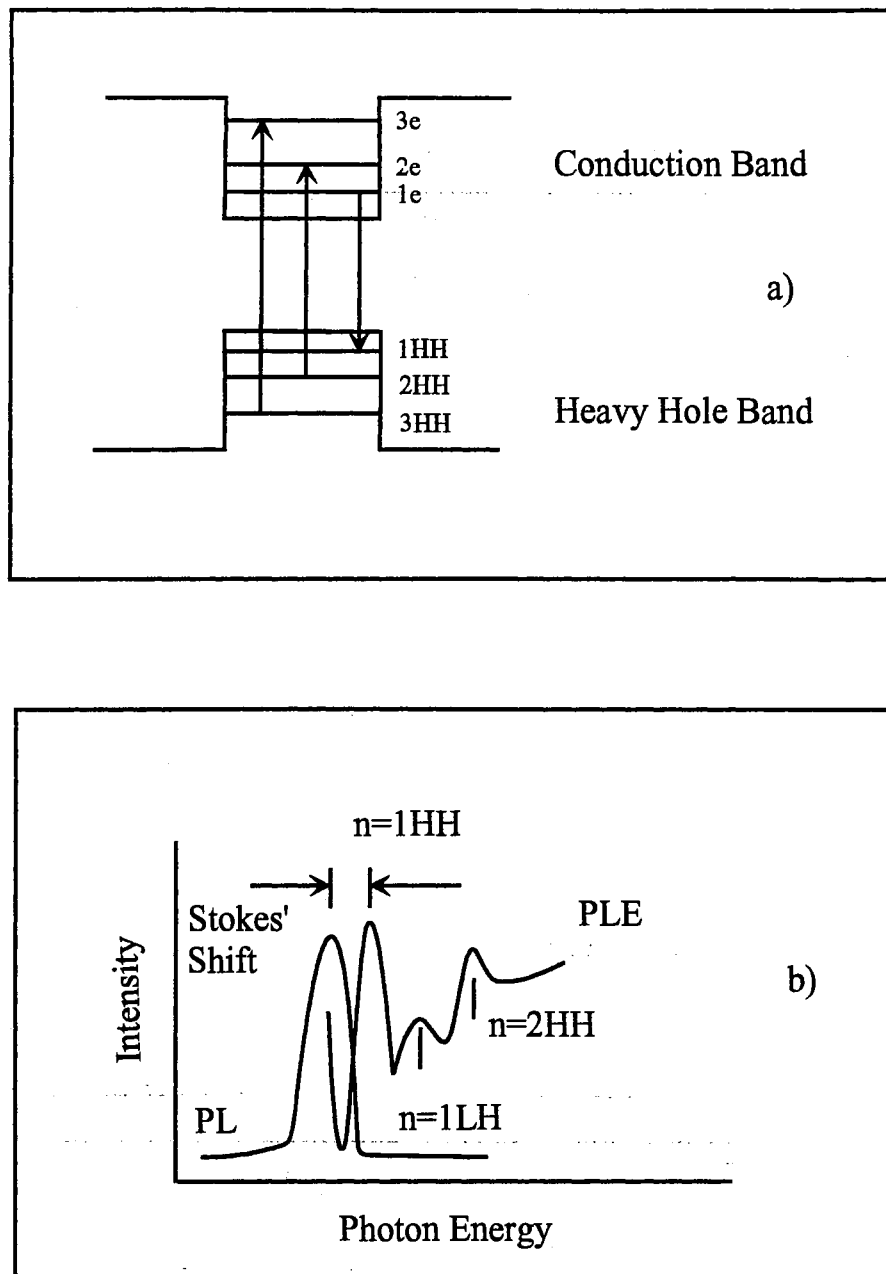


Figure 9. Photoluminescence excitation spectroscopy involves the observation of the photoluminescence of a sample as a function of the excitation energy as shown for a QW in a). The light hole band is excluded for clarity. In b), a typical SP-PLE spectra is sketched, showing the  $n=1$  and  $n=2$  excitonic resonances.

tube (PMT) used in conjunction with a photon counting and computerized data acquisition system. [69]

The ZnSe substrates facilitate the use of absorption spectroscopy since they are transparent in the QW energy state region. The linear absorption spectroscopy was performed utilizing a 0.5 m monochromator (Aries F500) for dispersion of the tungsten lamp source. The detector used was a UV-enhanced photodiode. The beam incident upon the sample was chopped to allow use of a lock-in signal averager. [69]. The ZnCdSe/ZnSe samples grown on GaAs were studied using a similar system, but using reflection geometry. The CdSe/ZnSe sample could not be studied in this manner due to poor surface quality. However, SP-PLE has been performed on this sample, [67,70] using a tungsten lamp and a 1/4 meter spectrometer as a source. The SP-PLE was detected using a 0.5 m spectrometer (Aries F500). This SP-PLE system is schematically illustrated in Fig. 10.

Photoluminescence and absorption spectra for sample D59 are shown in Fig. 11. This sample is grown on a ZnSe substrate. The double peaks in the absorption spectra at about 2.652 and 2.664 eV are due to 1HH-1e 1s excitons in different wells due to the different  $x$ -concentrations in the wells (as will be seen below in TP-PLE). Note that the PL peaks do not exhibit any observable Stokes' shift. The next highest peak is identified as due to the 1LH-1e 1s excitons. This peak appears to be a doublet, again due to different wells. No higher lying states are resolved in the absorption spectra. However, from this spectra it cannot be determined if any higher lying states exist due to the interfering absorption tail of the ZnSe substrate and barriers.

Similar spectra for a sample (D58) with a larger  $x$ -concentration is shown in Fig. 12. This sample also shows a doublet structure for the 1HH-1e 1s excitons (2.609 and 2.626 eV), and no observable Stokes' shift. The 1LH-1e 1s exciton peaks are also observed ( $\sim 2.67$  eV), and 2HH-2e 1s exciton can also be observed at about 2.72 eV. The dominant PL peak also does not show any Stokes' shift.

Absorption and PL spectra from sample D63A, as shown in Fig. 13, which has the lowest  $x$  value of the ZnSe substrate samples studied, again shows the

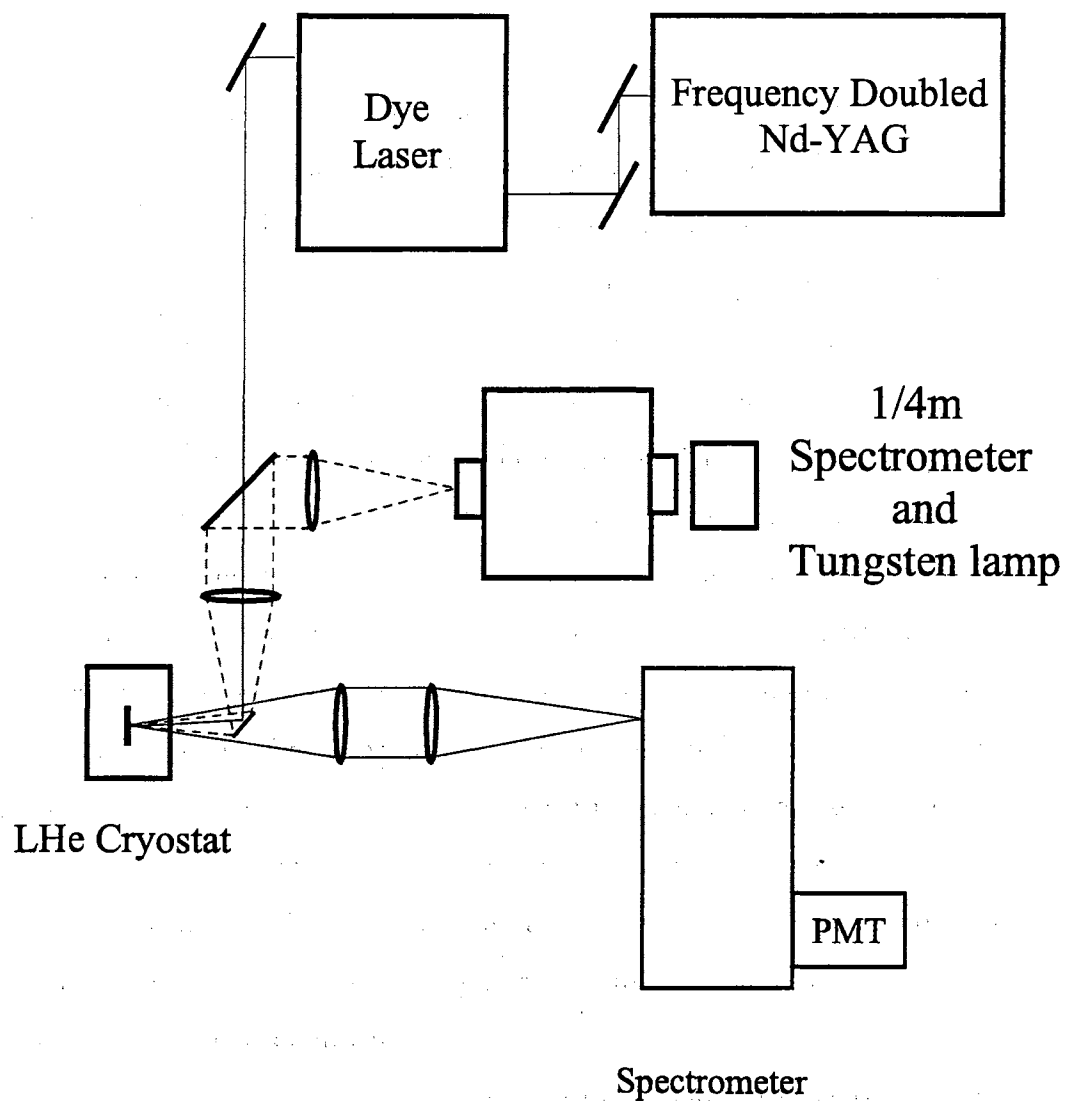


Figure 10. Two-photon and single-photon photoluminescence excitation spectroscopy system. PLE spectra may be obtained using either single-photon (tungsten lamp) or two-photon (Nd-YAG pumped dye laser) techniques.

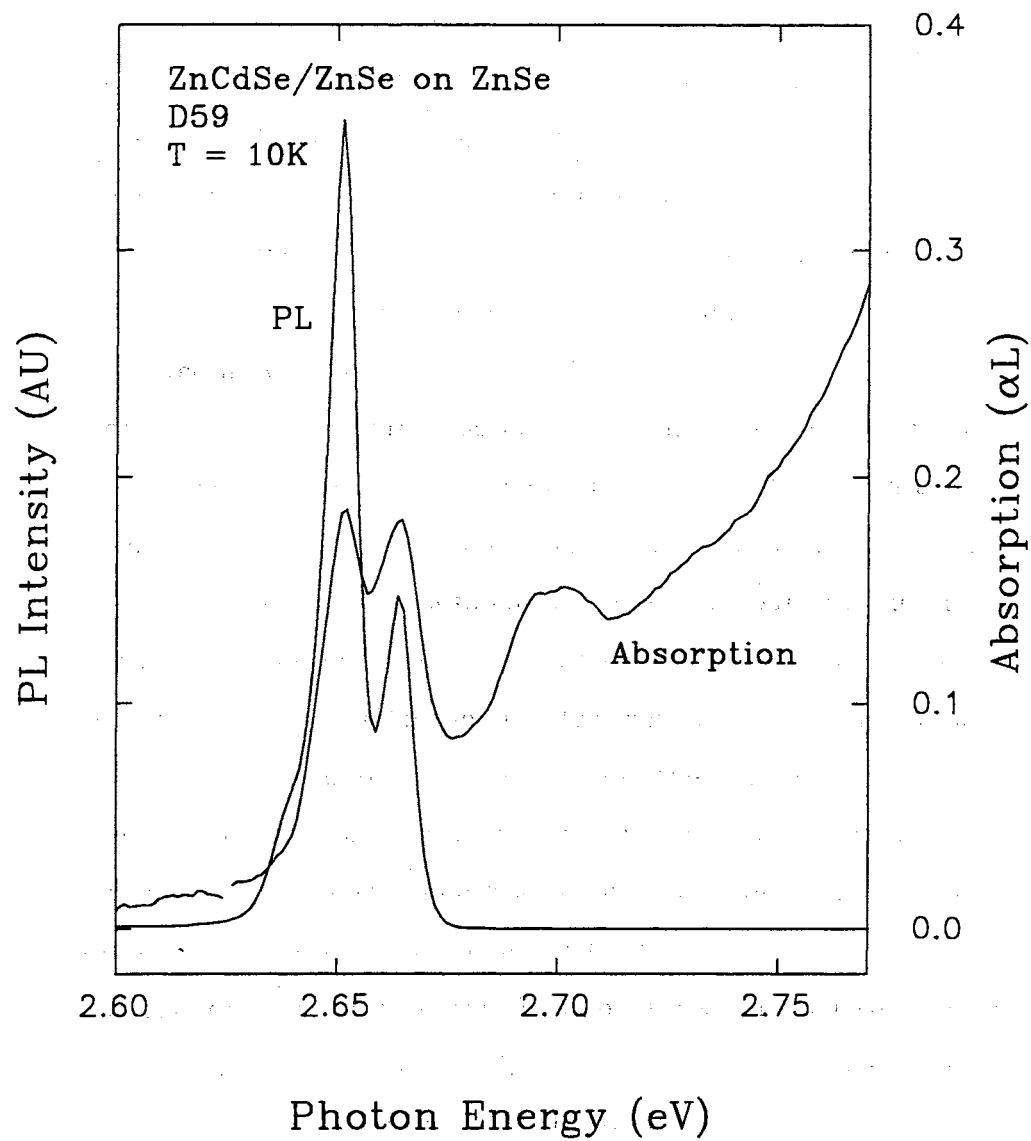


Figure 11. Single photon photoluminescence and absorption spectra for sample D59. The two lowest energy peaks are due to the  $1HH-1e$   $1s$  excitons. The peak at  $\sim 2.70$  eV is due to the  $1LH-1e$   $1s$  excitons.

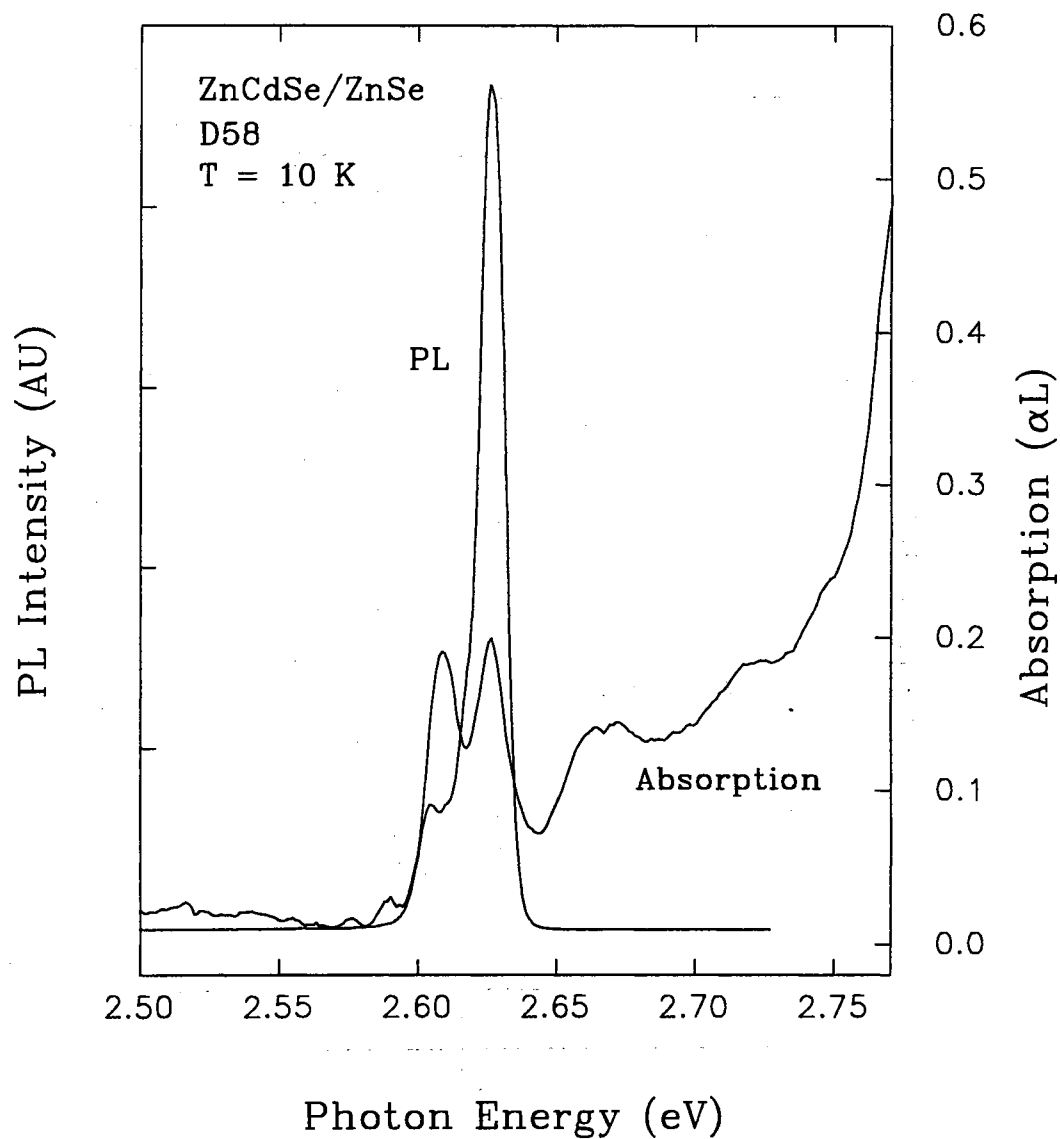


Figure 12. Single photon photoluminescence and absorption spectra for sample D58. The two lowest energy peaks are again due to  $1HH-1e 1s$  excitons. The peak at about 2.67 eV is due to the  $1LH-1e 1s$  excitons. An additional feature at about 2.72 eV is identified as due to  $2HH-2e 1s$  excitons.

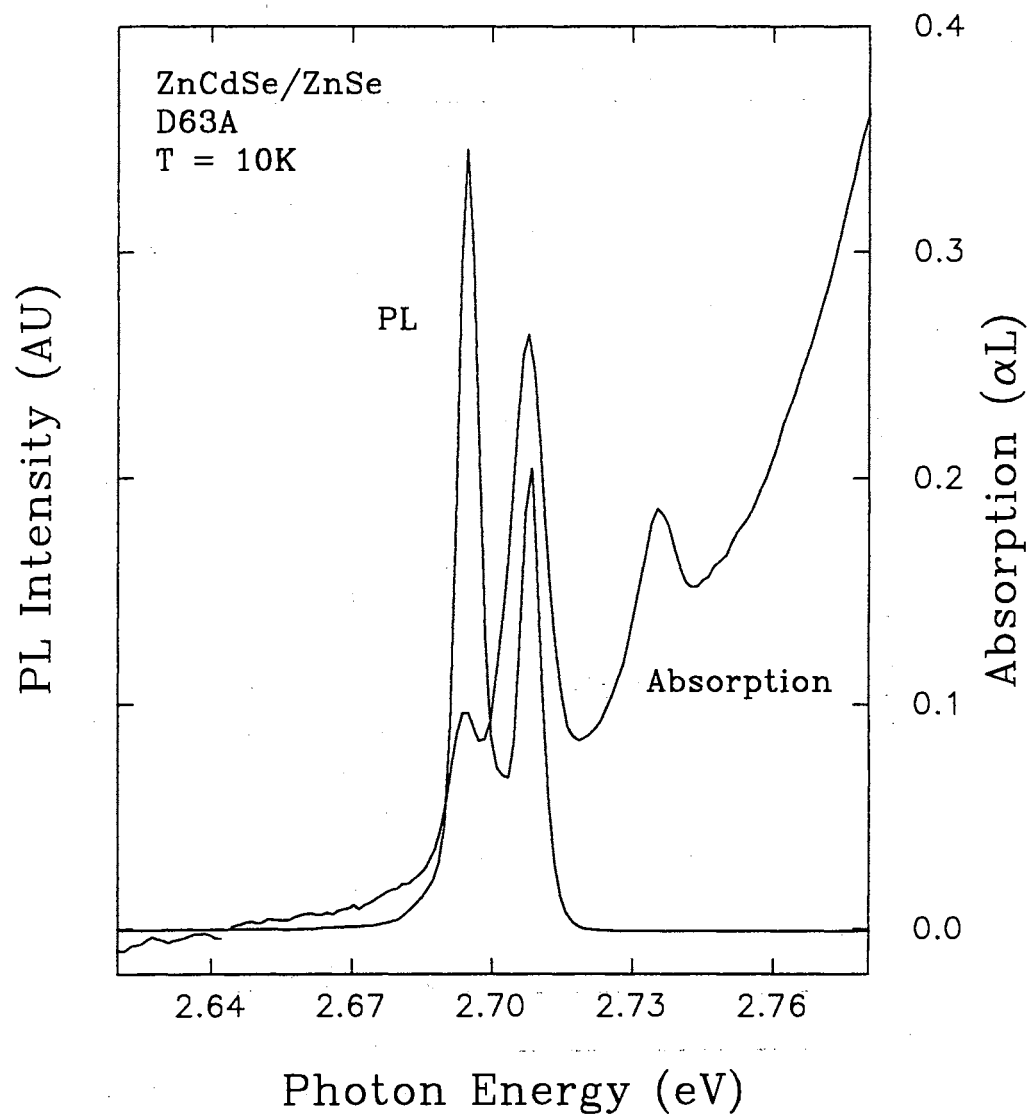


Figure 13. PL and absorption spectra for sample D63A. The 1HH-1e 1s excitons are seen at 2.694 and 2.708 eV. The peak at  $\sim 2.735$  eV is due to the 1LH-1e 1s excitons. No higher lying states can be observed due to the ZnSe absorption.

1HH-1e 1s excitons (2.694 and 2.708 eV) and a 1LH-1e 1s exciton peak (2.735 eV). This sample also does not show any higher lying excitonic levels in the absorption spectra. The full width at half maximum (FWHM) for all of the ZnSe substrate samples is 5 – 8 meV.

The assignments of the transitions in the data presented above have been checked by calculations using the envelope function approximation due to Bastard [71,6,72]. These calculations also suggest that the 1LH-1e transition is slightly Type II for these samples. However, the band-offset for the LHs is very small (a few meV), creating a superlattice state, where the holes may travel nearly freely through the wells and barriers. This would explain the strong 1LH-1e 1s transition, which is unexpected in well-confined Type II QW's. [73]

The reflectivity and photoluminescence for the 300 Å ZnCdSe/ZnSe sample grown on GaAs is shown in Fig. 14. The linewidth of the reflectivity data is wider than that of the PL, for the 1HH-1e 1s exciton with the peak shifted to slightly lower energies. The reflectivity data also appears to have a doublet structure. The cause of the broadened linewidth may be the fact that reflectivity is determined by both the real and imaginary part of the dielectric constant. Since the real part of the dielectric constant tails to lower (and higher energies), the apparent linewidth will be broadened. Another contributing factor could be spatial inhomogeneity in the sample, yielding slightly different energies at different spot on the sample. The 1LH-1e 1s exciton is also observed at about 2.696 eV.

The corresponding data for the 500 Å sample shows the 1HH-1e 1s exciton at about 2.690 eV, and the 1LH-1e 1s exciton at 2.712 eV. This data is shown in Fig. 15 The 1HH-1e 1s exciton linewidth of this sample is about 4 meV.

Single-photon PLE and PL spectra for the 2ML CdSe/ZnSe sample are shown in Fig. 16. The oscillations in the SP-PLE may arise from the Franz-Keldysh effect due to the large strain in the CdSe QW. The PL FWHM of almost 45 meV for this sample is quite large compared to the other samples.



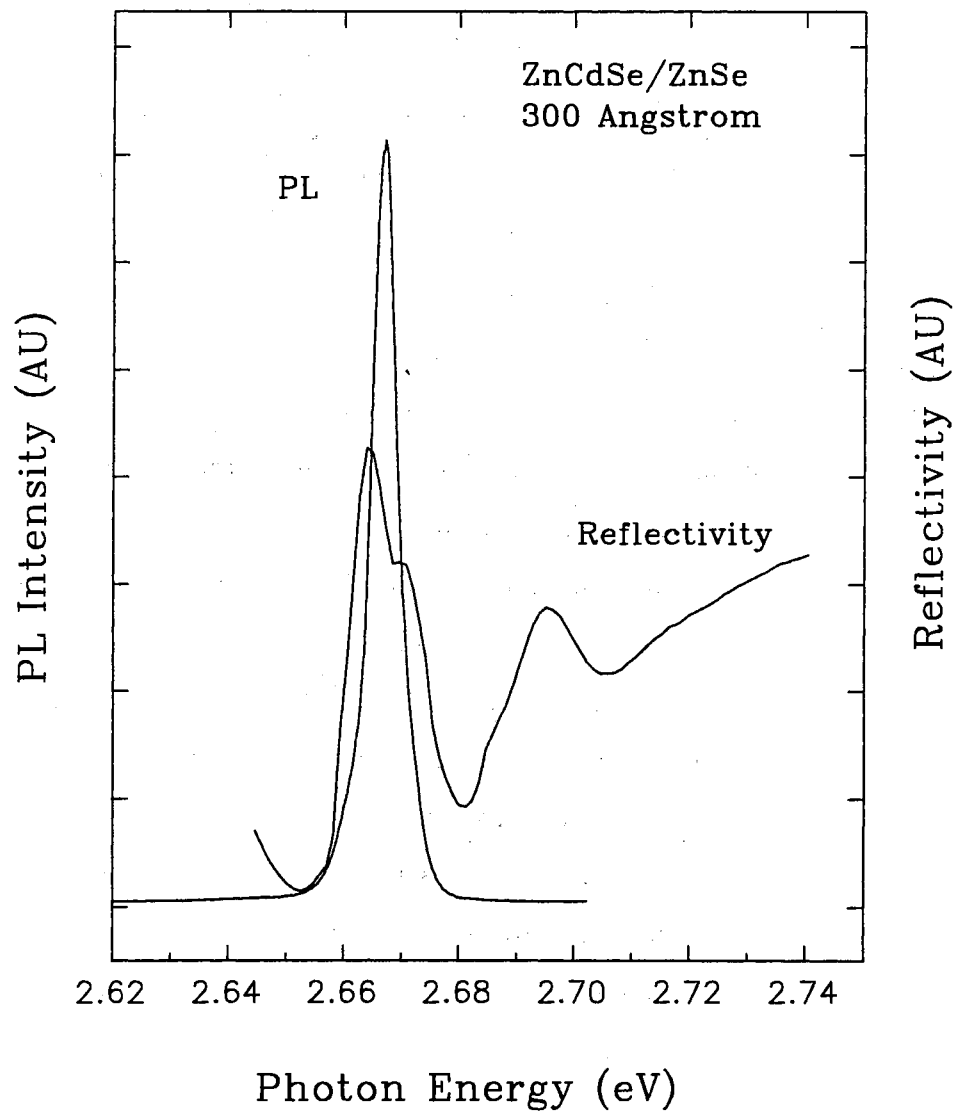


Figure 14. Single photon photoluminescence and reflectance spectra for the 300 Å ZnCdSe/ZnSe QW. The lowest energy peak at 2.67 eV is due to the 1HH-1e 1s excitons. The peak at  $\sim 2.70$  eV is due to the 1LH-1e 1s excitons.

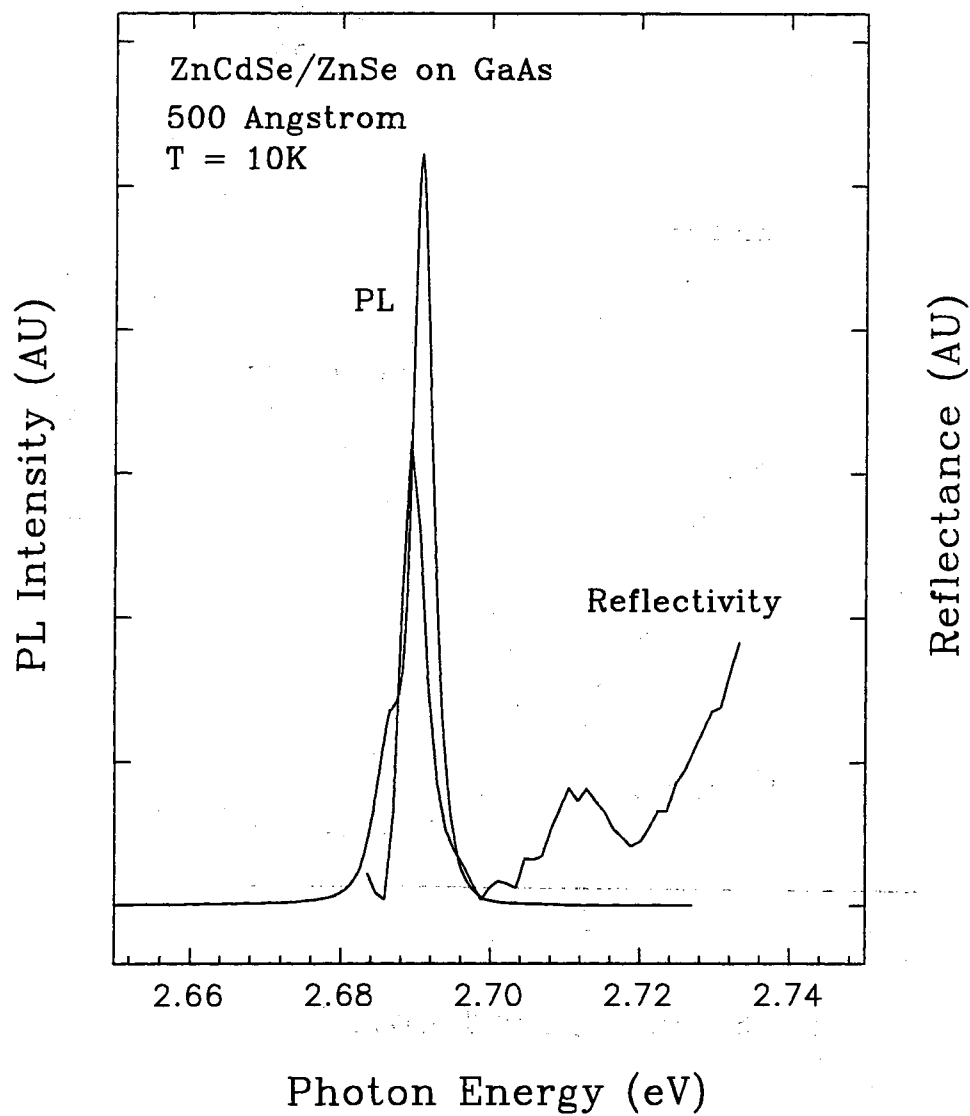


Figure 15. Reflectivity and PL data for the  $L_z = 500 \text{ \AA}$  sample. The lowest energy peak at 2.69 eV is due to the 1HH-1e 1s excitons. The peak at  $\sim 2.71$  eV is due to the 1LH-1e 1s excitons.

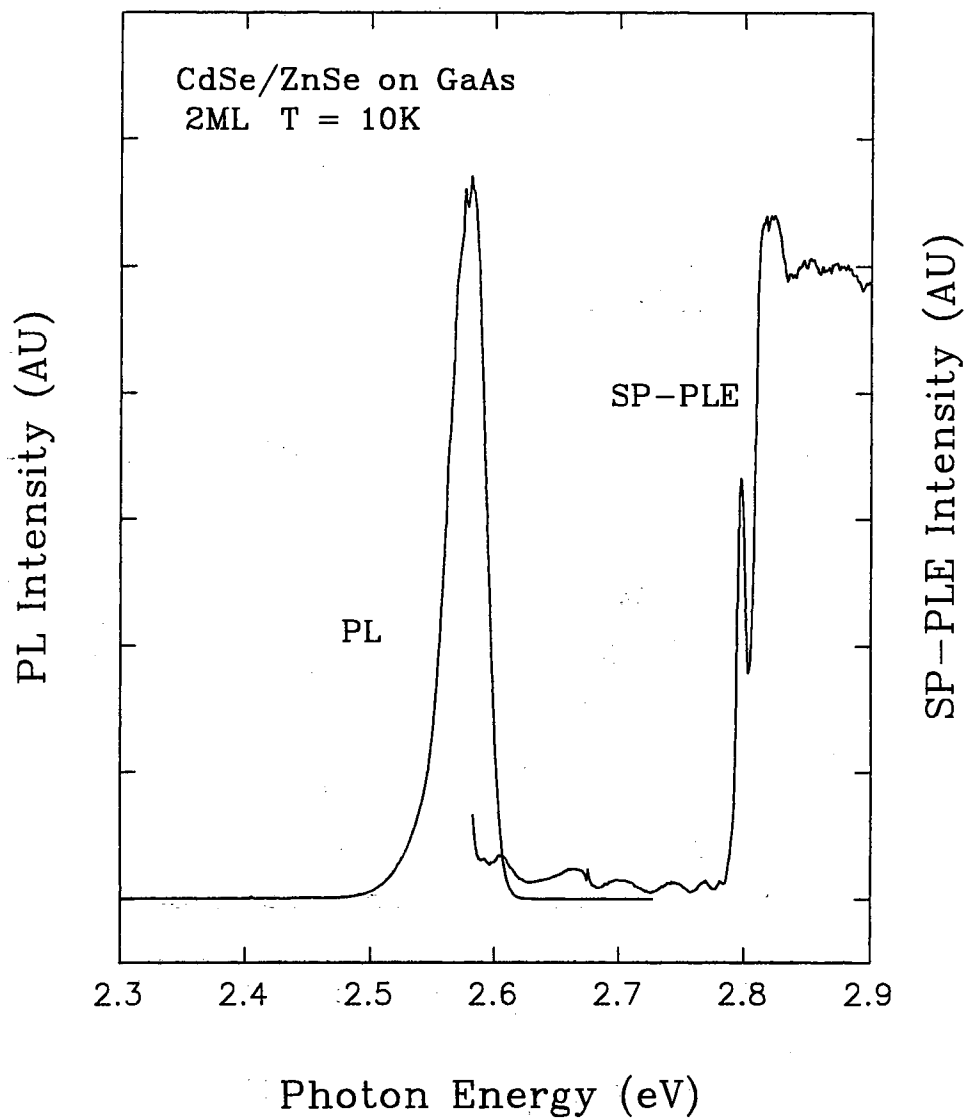


Figure 16. Single photon PLE and PL spectra for the 2ML CdSe/ZnSe sample. The peak at 2.592 eV is due to the  $1\text{HH}-1e\ 1s$  exciton. No higher lying states are observed in the SP-PLE spectrum, possibly obscured by the oscillatory structure.

Two-photon photoluminescence excitation spectroscopy of  $Zn_{1-x}Cd_xSe/ZnSe$  QW's.

The two-photon photoluminescence excitation (TP-PLE) spectra were taken using the backscattering configuration, as is shown in Fig. 10. The excitation source was a dye laser (using the Exciton dyes LDS925 and/or LDS867) pumped by the second harmonic of a 8 ns Nd-YAG laser. The infrared excitation beam was at near normal incidence to the surface of the sample. The polarization of the electric field was vertical and thus perpendicular to the z-axis (that is, the growth direction). The photoluminescence signal was collected into a spectrometer and detected using a GaAs PMT, or alternately, using an intensified CCD. A boxcar signal averager was also utilized in conjunction with the GaAs PMT. The TP-PLE data was divided by the square of the dye emission curves in order to eliminate the effect of the power variation of the dyes. All of the spectroscopic techniques were performed with the samples held at 10 K in a closed cycle liquid He cryostat. As is discussed above, with the polarization in the plane of the well ( $\epsilon \perp z$ ), the  $2p$  exciton states are observed, and the band-to-band emission increases linearly for each  $n$ . Additionally, the selection rules for this polarization allow only  $\Delta n = 0$  states to be observed in TP-PLE. For either polarization direction, the absorption edge is shifted to higher energies, with the absorption due to light polarized parallel at higher energies. An energy diagram showing the TP absorption and subsequent emission is shown in Fig. 17. As indicated in the figure, two photons are absorbed, creating either a  $p$ -state exciton or an electron-hole pair in the associated bands. These particles lose energy due to scattering or phonon emission, relaxing to the  $1HH-1e 1s$  exciton, which then recombines emitting a photon which is collected and detected.

The TP-PLE spectra for sample D59 is shown in Fig.18, superimposed over the linear absorption spectra. The TP-PLE spectra shown is taken with the detector set to the strongest PL peak. As can be seen in the figure, a strong resonance is seen above the  $1HH-1e 1s$  exciton transitions. This feature is ascribed to the  $2p$  state of the  $1HH-1e$  exciton. At higher energies, a steep rising slope is observed which is identified as being due the  $1HH1-1e$  continuum. The fit to the linear

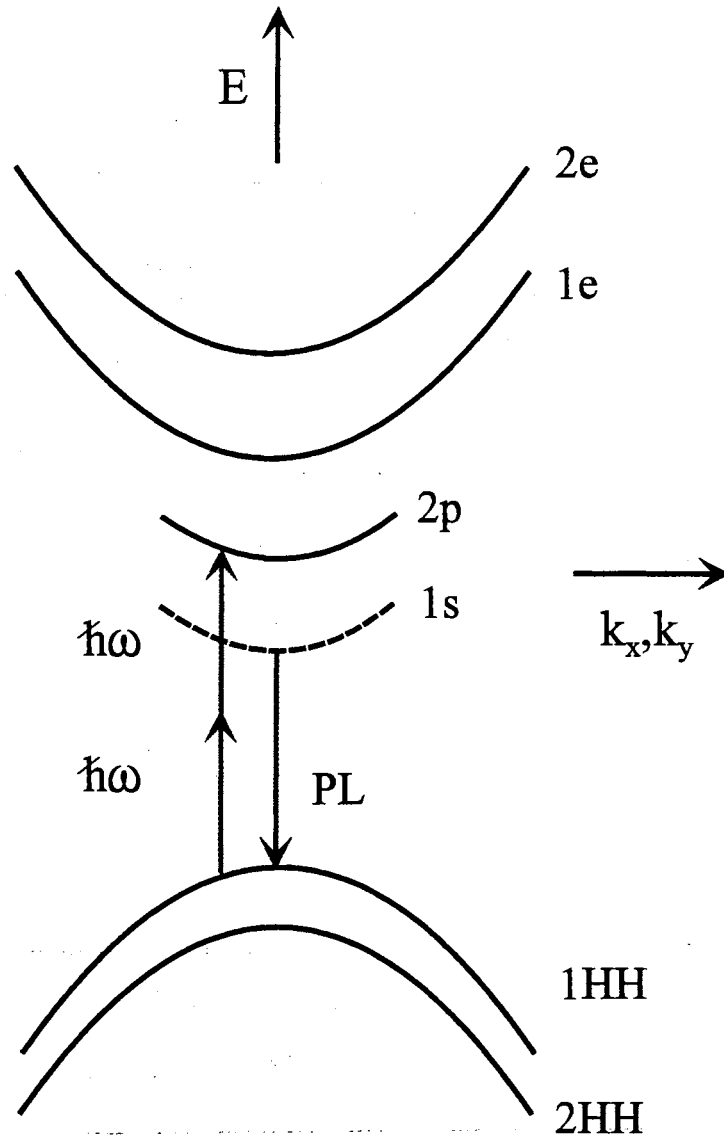


Figure 17. TP-PLE spectra is obtained with the detector set to  $E_{1HH-1e}^{1s}$ . The excitation photon energy is scanned and resonances are observed at the allowed transitions. Specifically, for  $\vec{E} \perp \hat{z}$ , the  $p$  states are allowed as are the  $\Delta n = 0$  continuum states.

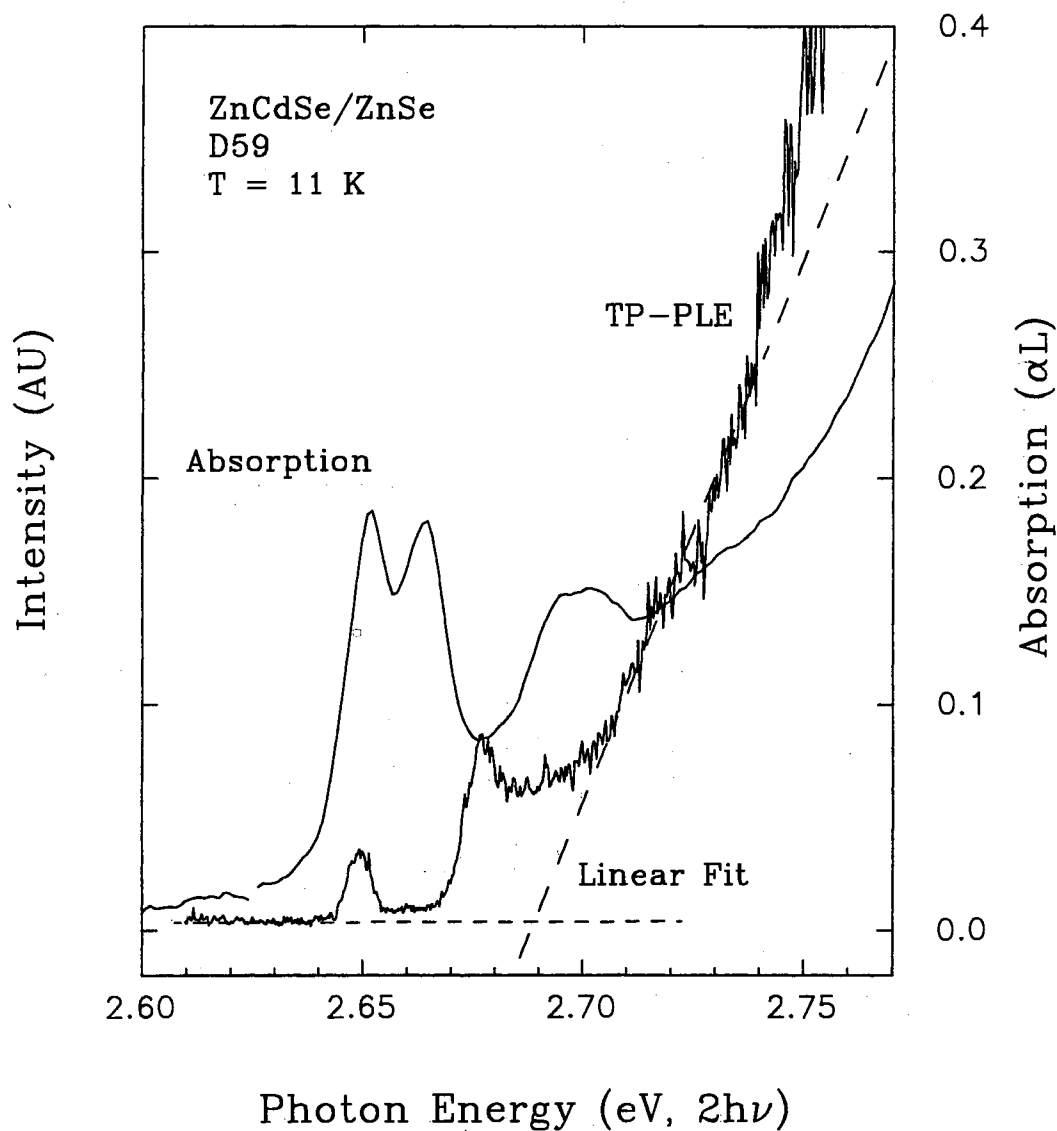


Figure 18. Two-photon photoluminescence excitation and linear absorption spectra for sample D59. The dashed line is a linear fit to the rising slope of the 1HH-1e continuum transition. The intersection of this fit with the baseline gives, in conjunction with the 1HH-1e 1s exciton observed in linear absorption,  $E_b^{1s}$ .

dependence of  $2\hbar\omega - E_g$  of this rising slope can be extrapolated back to give the energy position of the onset of this resonance [39,54]. This linear rising slope has been observed in GaAs/AlGaAs QW's. [39] Using the value for the onset of the continuum state found in this manner, minus  $E_{1HH-1e}^{1s}$ , gives the 1s exciton binding energy of  $37 \pm 2$  meV.

Two TP-PLE spectra for sample D58 are shown in Figs. 19 and 20, with the detector set to the lower ( Fig. 19) and higher ( Fig. 20) energy 1HH-1e 1s exciton positions. The 2p resonance can be clearly seen in both TP-PLE spectra. Since the 2p exciton is shifted between the two spectra, it appears that the 1HH-1e 1s exciton peaks are not energetically connected. This supports the assumption that the two peaks observed in the absorption spectra are due to separate wells. Another possibility, that cannot be ruled out, is that the two states arise within a well, but are localized. The onset of the 1HH-1e continuum can not be clearly determined using the technique for D59. The binding energy of the unperturbed 2p state of the exciton in bulk ZnSe is 5 – 6 meV [74], thus a lower limit can be set on the 1s binding energy by addition of 5 meV to the position of the 2p state. This gives a binding energy of  $> 38$  meV. An upper limit can easily be set by the position of the unambiguous contribution from the 1HH-1e continuum. Thus the binding energy of the 1HH-1e 1s exciton in this QW is  $38 \text{ meV} < E_b < 44 \text{ meV}$  for the spectra presented in Fig. 19. When the detector is set to the higher energy peak, the spectra yields the binding energy to be  $41 \text{ meV} < E_b < 49 \text{ meV}$ .

A similar spectra is shown in Fig. 21. In this lower Cd percentage sample the 2p state of the 1HH-1e exciton is clearly visible. In this case, the onset of the continuum states is visibly separated from the 2p state. Using the onset of the 1HH-1e continuum for estimating the binding energy of the 1s exciton, the range determined is  $38 \text{ meV} < E_b < 42 \text{ meV}$ . The peak between the 2p exciton and the 1HH-1e continuum states may be due to the enhanced scattering of the tail of the 2p state by LO phonons into the 1s exciton state, or possibly, absorption due to the 3p exciton.

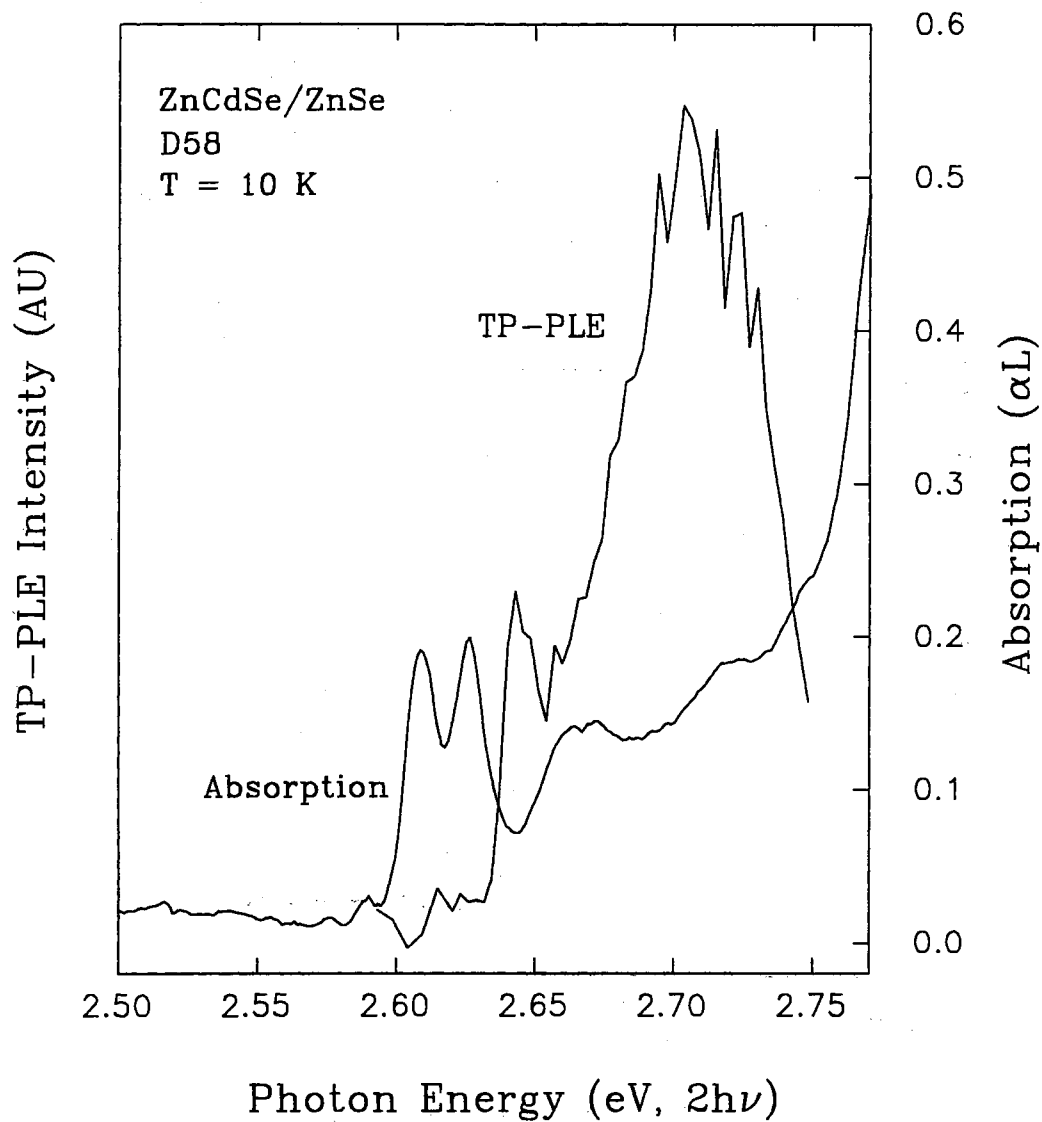


Figure 19. TP-PLE spectrum of sample D58 with the PL position set to the lowest HH exciton. Also shown is the absorption spectra for this sample. The sharp peak is ascribed to the  $1HH-1e\ 2p$  state.



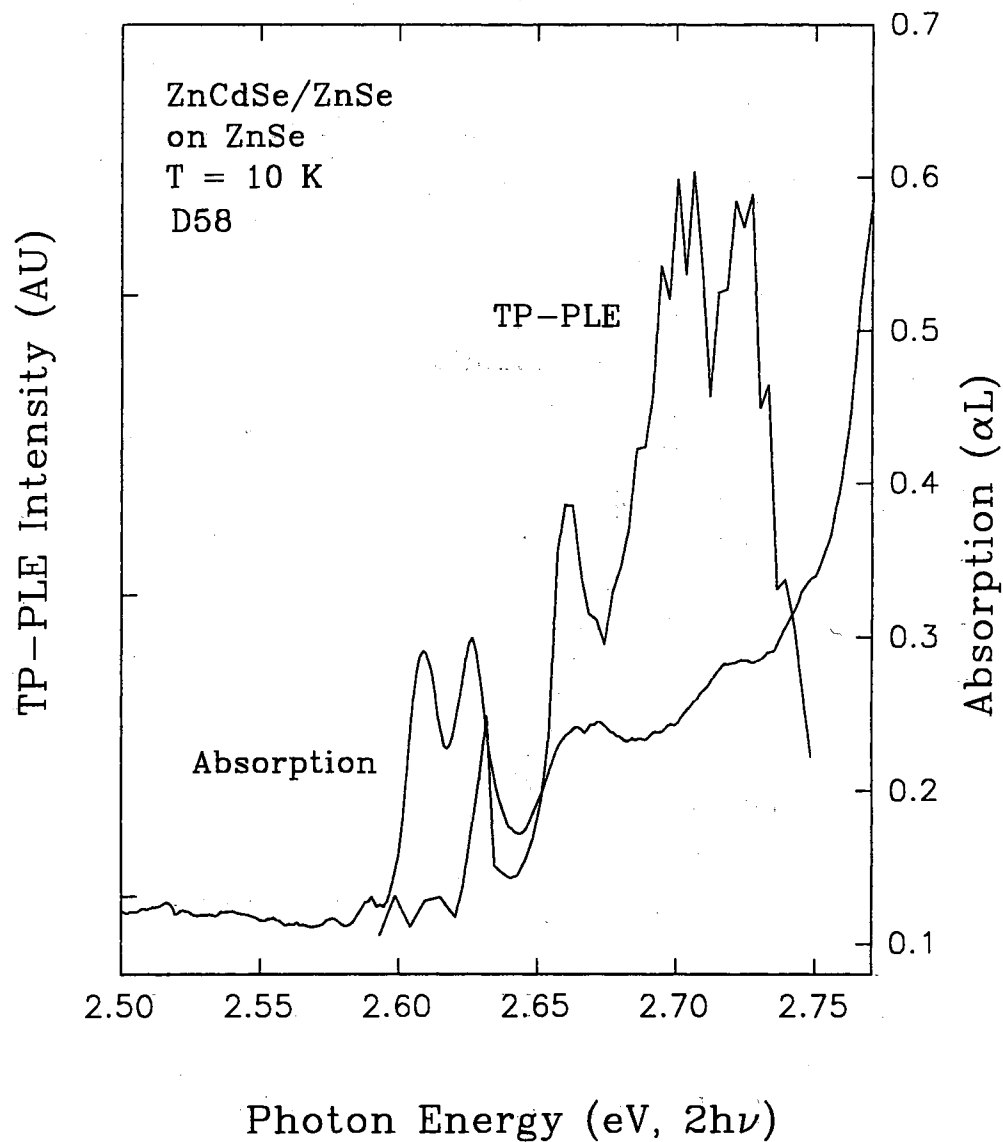


Figure 20. TP-PLE spectrum of sample D58 with the PL set to the highest energy HH exciton. Note that the position of the  $2p$  exciton is shifted from the previous spectra. This implies that the two  $1HH-1e$   $1s$  excitons are not energetically connected.

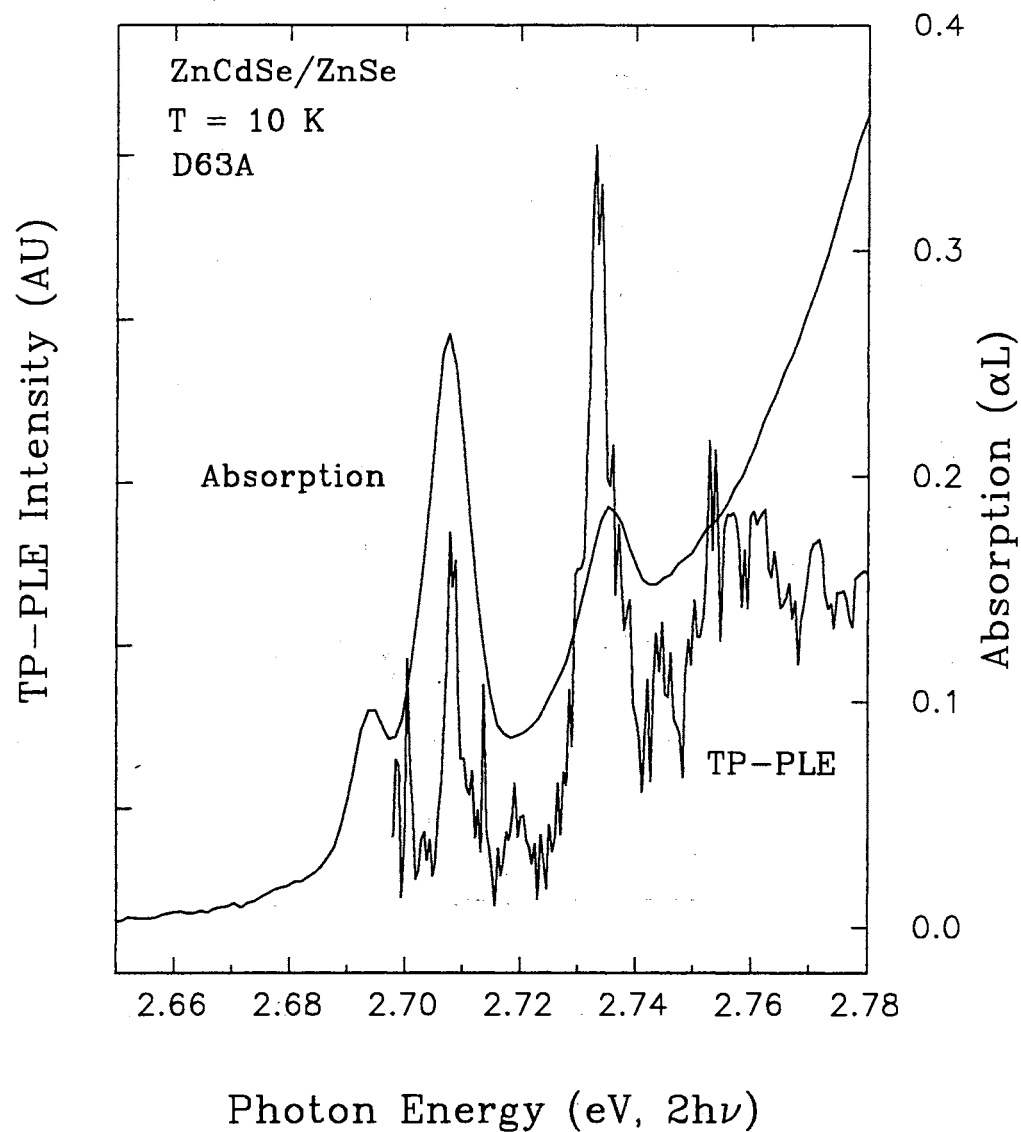


Figure 21. Two-photon photoluminescence excitation spectrum for sample D63A. The  $2p$  exciton is clearly visible at 2.734 eV. The onset of the  $1HH-1e$  continuum is taken to be at about 2.748 eV.

The TP-PLE spectra of the 300 Å MQW shows as small bump at energies just above the 1HH-1e exciton as is seen in Fig. 22. This bump is attributed to the 2p exciton. At higher energies, a linearly rising slope can be seen. Extrapolating back, and using the reflection data, which is also presented in Fig. 22, the binding energy can be determined to be approximately 22 meV. For the 500 Å sample (Fig. 23), the 2p state is not clearly visible, while the excitonic binding energy calculated from the linear fit is about 20 meV. Note that this value is about the same as the accepted value for the exciton binding energy of bulk ZnSe. This result is not surprising, since for this wide well, the excitons should be essentially bulk-like.

The third type of sample, that is, a SQW sample with a 2ML wide well of CdSe/ZnSe grown on GaAs. Two photon PLE and PL spectra for this sample are shown in Fig. 24. The linear fit to the rising slope for this sample, in conjunction with the SP-PLE spectra shown in the previous section yield an exciton binding energy of  $38 \pm 2$  meV. Note that the TP-PLE spectra of this sample also exhibits TP absorption into the 1s exciton region.

### Discussion of results

The absorption coefficient observed for the ZnSe substrate  $\text{Zn}_{1-x}\text{Cd}_x\text{Se}$  quantum wells of approximately  $0.2 \alpha L$  converts to an effective  $\alpha = 1.4 \times 10^5$  for samples D58 and D59 if the double equal intensity peaks are taken to be indicative of two separate well widths within the sample. This result is close to that reported by Ding *et al.* of  $\alpha \simeq 1.8 \times 10^5$  for a  $\text{Zn}_{0.76}\text{Cd}_{0.24}\text{Se}$  sample with  $L_z = 35$  Å. [75]. The same group reported  $\alpha \simeq 9 \times 10^4$  for a  $L_z = 200$  Å sample [75]. The data presented here are consistent with these previous reports since the oscillator strength of the excitons should increase with confinement. [76] All of the ZnSe substrate samples exhibit a near zero Stokes' shift and narrow linewidths for both PL and absorption spectra. The FWHM of the 1HH-1e 1s exciton in these samples is between 5 and 8 meV.

The results of the binding energy measurements and peak positions of important transitions are summarized in Table III. The binding energies found in

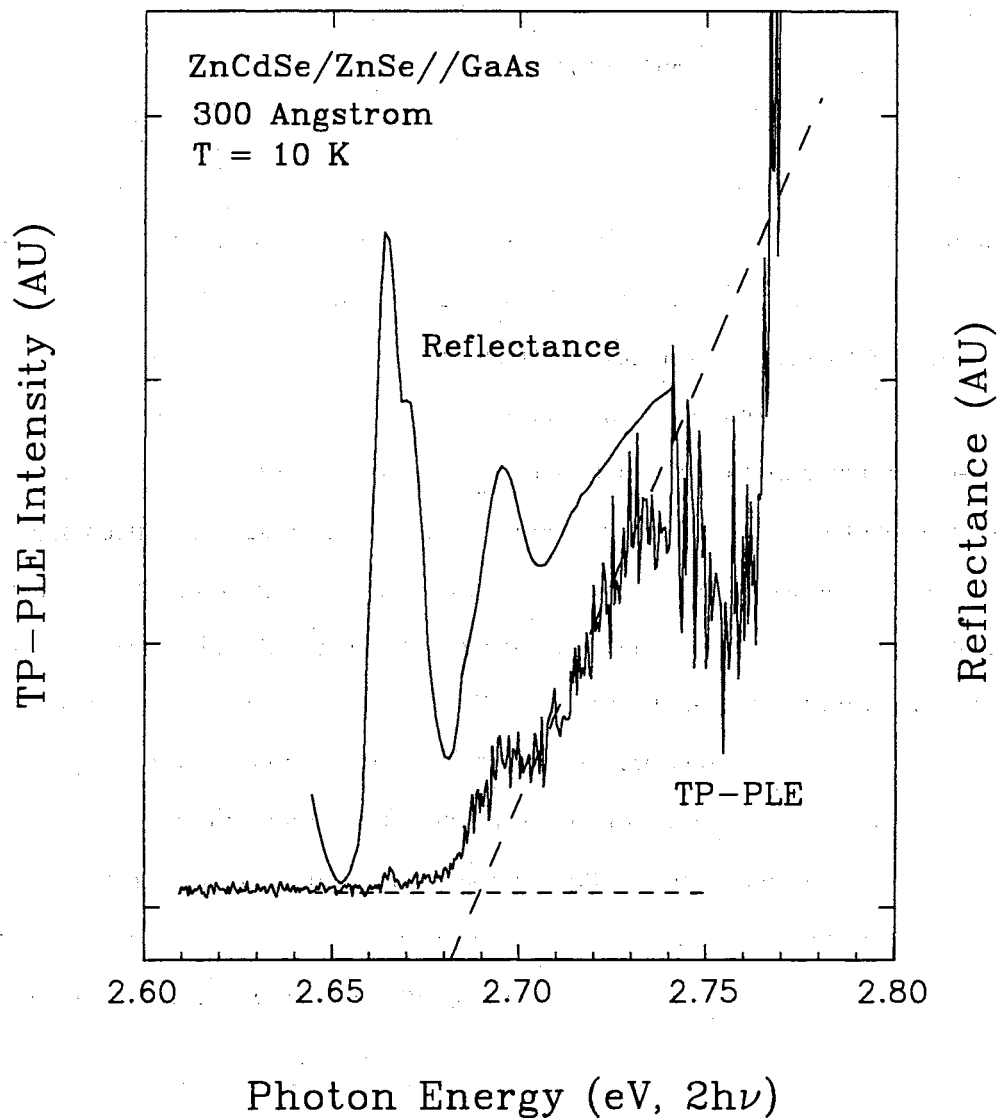


Figure 22. Two-photon photoluminescence excitation spectrum for the 300 Å QW. The small shoulder in the TP-PLE spectra is attributed to the  $2p$  exciton. The linear fit to the rising slope is shown as the dashed line.

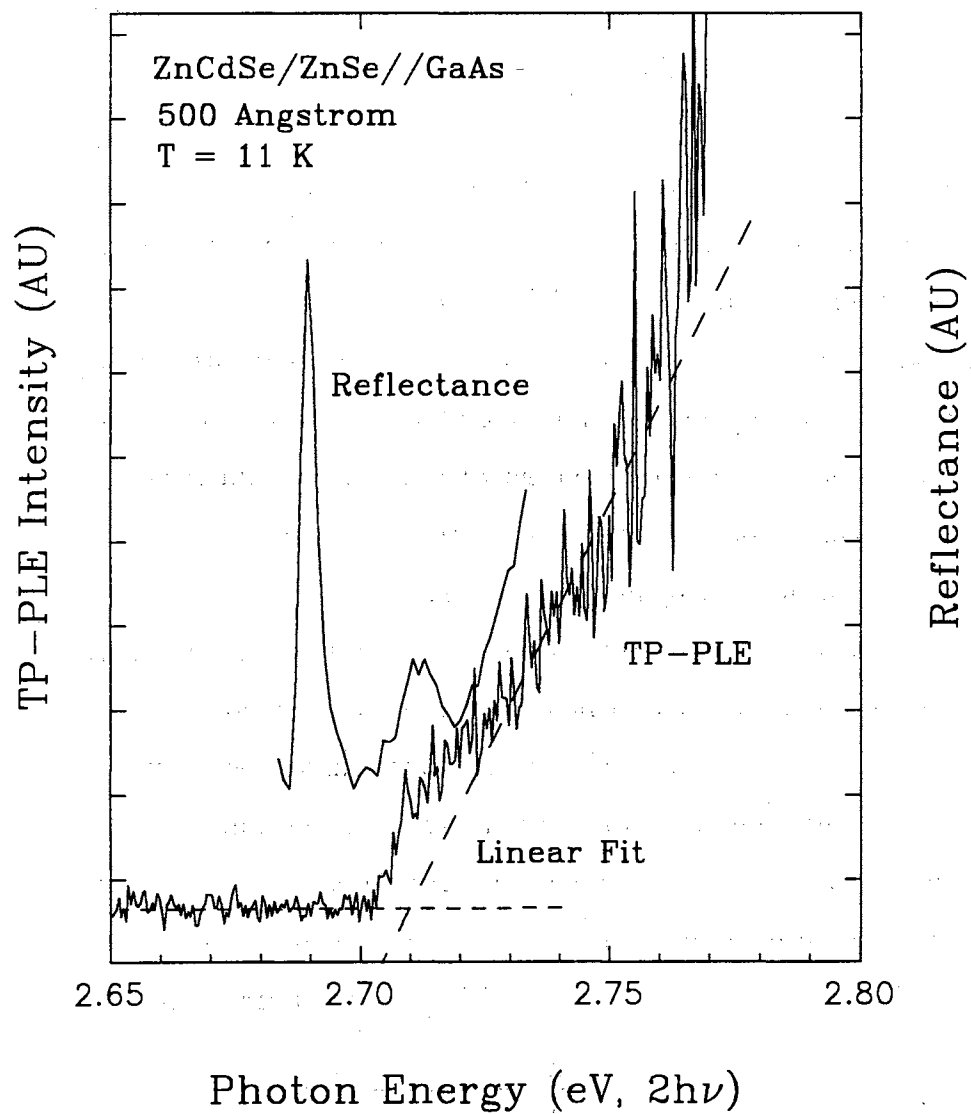


Figure 23. Two-photon PLE and reflectance spectra for the 500 Å sample. The dashed line is the linear fit to the TP-PL data. The weak shoulder is attributed to the  $2p$  exciton.

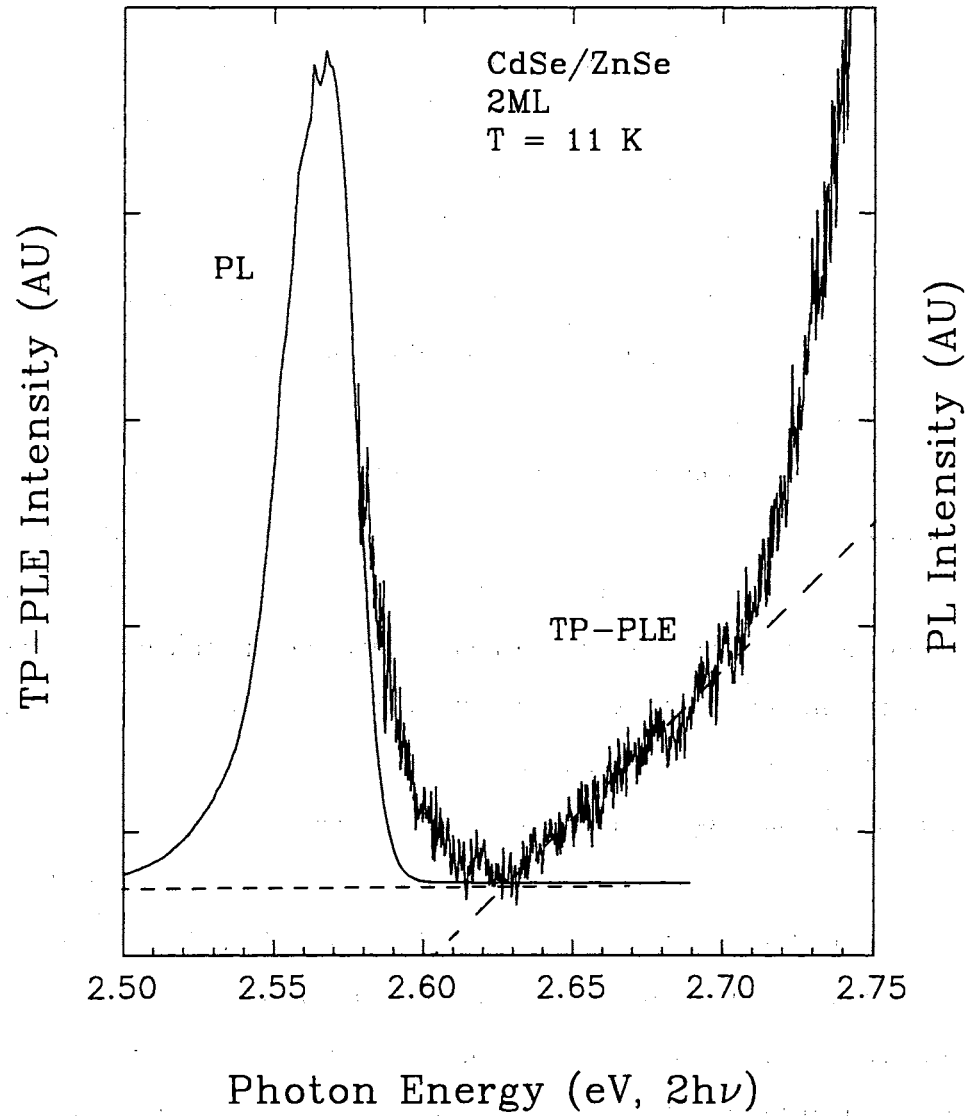


Figure 24. Photoluminescence and TP-PLE spectra for 2ML sample. The dashed line is a linear fit to the rising slope of the TP-PLE data. Note that TPA is observed in the  $1HH-1e\ 1s$  region and no  $2p$  excitonic feature is seen.

TABLE III.

The results of the binding energy measurements and peak positions of important transitions are summarized.

Sample	$E_{1s}^{1HH-1e}$ (eV)	$E_b(1s)(meV)$	$E_b(2p)(meV)$	$E_{1s}^{1LH-1e}$ (eV)
D58	2.609	41-49	8-16	2.664
	2.626	38-44	4-10	2.672
D59	2.652	35-39	10-14	2.695
	2.664	-	-	2.702
D63A	2.694	-	-	-
	2.708	38-42	13-17	2.736
300 Å	2.667	20-22	-	2.696
500 Å	2.690	18-22	-	2.712
2ML	2.592	36-40	-	-

the  $L_z = 50 \text{ \AA}$  samples are in the same range as that found by Pelekanos *et al.* of 35-41 meV for a  $L_z = 90 \text{ \AA}$  well with  $x = 0.25$ . [52] The authors were able to determine  $E_b^{1s}$  in this particular sample due to the observation and identification of the  $2s$  state of the 1HH-1e exciton in absorption spectroscopy. The value of the splitting allowed determination of the exciton binding energy using the 2D and 3D limits for the binding energy. However, in general, the  $2s$  state is not observable using this method.

Two-photon PLE of GaAs/AlGaAs QW's usually do not exhibit distinct peaks for the  $2p$  exciton resonances [39], although Catalano *et al.* have reported observation of the  $2p$  state of the 1LH-1e, 2HH-2e and 2LH-2e transitions [40]. The enhancement of the  $2p$  state of the 1HH-1e transition in ZnCdSe/ZnSe quantum wells as compared to GaAs/AlGaAs quantum wells may be due primarily to the smaller exciton radius and accompanying increased binding energy [54]. As mentioned earlier, the  $2p$  exciton has been observed in two-photon spectroscopy of bulk ZnSe, so it should not be surprising that it is easily observable in QW's based on this material. The  $2p$  excitons have been recently reported for ZnSeS/ZnSe QW's grown on GaAs for the 1HH-1e, 2HH-2e and 1LH-1e continuum states. [44] This the first known report of  $2p$  excitons in ZnCdSe QW's.

A plot of the binding energies found in the above as a function of well width is shown in Fig. 25. In this figure, the solid line is the reduced exciton binding energy as a function of the reduced well width for a infinitely deep quantum well. The exciton binding energy is given by [77]

$$\frac{E_b}{E_0} = \left\{ 1 - \frac{1}{2} \exp \left[ \frac{1}{2} \left( \frac{L_w}{a_0} \right) \right] \right\}^{-2}$$

The reduced exciton binding energy is  $E_b/E_0$ , and the reduced well width is  $L_w/a_0$ , where the  $E_0$  is the free exciton binding energy in the bulk case, and  $a_0$  is the exciton (bulk) Bohr radius. The other symbols are as defined earlier. This equation arises from an assumption that the fractional dimensionality of an exciton varies exponentially with the reduced well width. This fractional dimensionality is due to the fact that, for any real quantum well, the exciton is not two dimensional



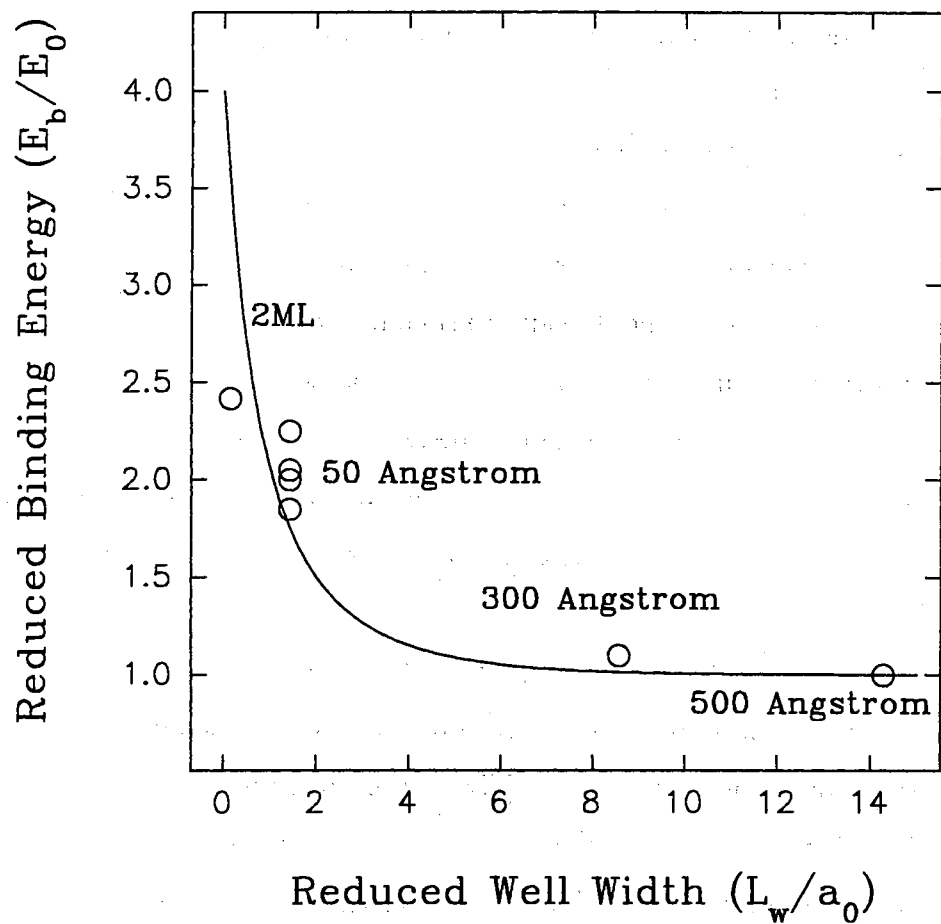


Figure 25. Variation of the exciton binding energy with well width. The exciton binding energy varies exponentially with  $1/L_w$ . The theory is shown by the solid line, and the experimental data points by the open circles.

(2D). This dimensionality may be parameterized by the expression [77]

$$\alpha = 3 - \exp \left[ -\frac{1}{2} \left( \frac{L_w}{a_0} \right) \right],$$

where  $\alpha$  is the fractional dimension. Note that this equation yields the expected behavior in the limits; for an infinitely wide well,  $\alpha = 3$ , and for an infinitely small well  $\alpha = 2$ . The factor of  $1/2$  is due to the fact that  $a_0$  is the excitonic Bohr radius and not the diameter.

In Fig. 25, the free exciton parameters for bulk ZnSe were used, since these parameters are not fully characterized for different alloys of ZnCdSe. For the CdSe SQW, bulk CdSe parameters have been used. The parameters used are for ZnSe:  $E_b = 20$  meV [78], exciton Bohr radius  $a_0 = 35$  Å and for CdSe:  $E_b = 15.7$  meV [78],  $a_0 = 41$  Å and lattice constant  $a = 6.05$  Å (cubic phase) [3]. The CdSe exciton Bohr radius was calculated using  $\epsilon = 9.29$ ,  $\mu^* = 0.095 m_e$  [78]. The circles in the figure are the experimental data found in this study. The spread seen in the different 50 Å wells may be due to the differing  $x$ -concentrations, as can be observed from the different positions of the PL and lowest energy absorption peaks. The different  $x$  values would result in different bulk exciton binding energies, as well as different dimensionalities due to the different degree of confinement.

The data follows the general trend quite well, except that the 50 and 300 Å wells are slightly high and the 2ML sample low relative to the theory. The reason for the high values of  $E_b/E_0$  is unclear. If the decrease in  $E_0$  due to the introduction of Cd into the lattice is included,  $E_b/E_0$  would increase, not decrease. Considering a linear form for the variation of  $E_b$  (although there is no basis for this assumption), the bulk binding energy for the alloy material would be between 19.3 and 19.6 meV. This effect is smaller than the experimental error assumed of  $\pm 2$  meV.

If the effect of a noninfinite well is considered, the excitons should become more three dimensional, which would decrease the binding energy of the excitons in the model. The exciton in the 2ML sample probably has a smaller binding energy than in the infinite well case because it is more three dimensional. As the

energy states of the exciton approaches the top of the well, the wavefunction of the exciton can spread over a larger volume, decreasing the binding energy. [77]

### Conclusions

The absorption coefficient observed for the ZnSe substrate  $\text{Zn}_{1-x}\text{Cd}_x\text{Se}$  quantum wells of approximately  $0.2 \alpha L$  converts to an effective  $\alpha = 1.4 \times 10^5 \text{ cm}^{-1}$  for sample D58. All of the ZnSe substrate samples exhibit a near zero Stokes' shift and narrow linewidths for both PL and absorption spectra. The FWHM of the 1HH-1e 1s exciton in these samples is between 5 and 8 meV.

The  $2p$  state of the 1HH-1e exciton in  $\text{Zn}_{1-x}\text{Cd}_x\text{Se}$  quantum wells has been observed. Additionally, the two-photon allowed 1HH-1e continuum state allows direct determination (for some samples) of the 1HH-1e 1s exciton binding energy, using TP-PLE in conjunction with the linear absorption or reflectivity data. For a well widths of 50 Å, the binding energies range from a minimum of 35 meV up to possibly 49 meV for a sample with a higher  $x$ -value. The binding energies for wider wells are about 21 meV (300 Å well) and 20 meV (500 Å well). These values are of great importance for devices since the LO-phonon energy of ZnSe is about 31 meV. Scattering of the lowest 1s exciton into the 1HH-1e continuum decreases the lifetime of the exciton, especially at elevated temperatures.  $\text{Zn}_{1-x}\text{Cd}_x\text{Se}/\text{ZnSe}$  QW's of 50 Å or less in width and with  $x = 10 - 15\%$  should have binding energies large enough to be stable at room temperature. However, there is a limit to increasing the binding energy with decreasing well width as is observed for the 2ML sample in this study. As the well width is decreased, the exciton binding energy will reach a maximum value due to its limited spatial extent. As the well width is decreased beyond this value, the binding energy will decrease due to the spreading of the wavefunction into the barrier. This occurs because the wells are not infinitely deep, and the narrow wells have states with energies very near the barrier levels. This allows spreading of the wavefunctions into the barriers, and thus a decrease of the binding energy as the exciton becomes more three dimensional.

## Non-degenerate four-wave mixing spectroscopy

The mixing of two laser beams of differing wavelengths in order to generate a third beam in the direction  $2\vec{k}_1 - \vec{k}_2$  of frequency  $2\omega_1 - \omega_2$  (or in the direction  $2\vec{k}_2 - \vec{k}_1$  and of frequency  $2\omega_2 - \omega_1$ ) as a spectroscopic technique has been referred to in the literature by many different names. The most common name for this type of spectroscopy is CARS or CSRS for Coherent Anti-Stokes Raman Spectroscopy or Coherent Stokes Raman Spectroscopy [79,80]. However, these names are unnecessarily restrictive as they imply that the resonance of interest is of the Raman type (as was historically the case). Another name sometimes given is three-wave mixing. [81] This name is used because there are two input beams and one output beam of interest. Recently, the term nondegenerate four-wave mixing (NDFWM) has become more accepted since it illustrates the commonality of the basic theory of this type of spectroscopy and other types of four-wave mixing (FWM), [29,33,82] and describes the interaction process in particular, but less restrictive, terms.

The generation of a coherent beam of frequency  $2\omega_1 - \omega_2$  in the direction  $2\vec{k}_1 - \vec{k}_2$  (or of frequency  $2\omega_2 - \omega_1$  in the direction  $2\vec{k}_2 - \vec{k}_1$ ) is governed by the third-order nonlinear susceptibility,  $\chi_{k_j i h}^{(3)}(\omega_\sigma; \omega_1, \omega_1, \omega_2)$  (or  $\chi_{k_j i h}^{(3)}(\omega_\sigma; \omega_2, \omega_2, \omega_1)$ ) [83-85,79,29].

Non-degenerate four-wave mixing spectroscopy has been performed on CdTe and ZnSe bulk samples and ZnCdSe/ZnSe quantum well structures.

A schematic diagram of the NDFWM spectroscopy system utilized in these studies is shown in Fig. 26. A Spectra Physics frequency doubled Nd-YAG (Nd-doped yttrium aluminum garnet, with a pulse width of approximately 8 ns, and a frequency of 10 Hz) laser is used as the pump source for a scanable Lambda Physik dye laser, as well as a source for the 1.06  $\mu\text{m}$  light used for one of the mixing beams. The dye laser is capable of being tuned from the yellow-green region of the spectrum to nearly 1  $\mu\text{m}$  using various dyes. The dyes most commonly used in these studies were LDS 925, LDS 867. The number designation on these dyes closely correspond to the peak wavelength of the tuning curve.

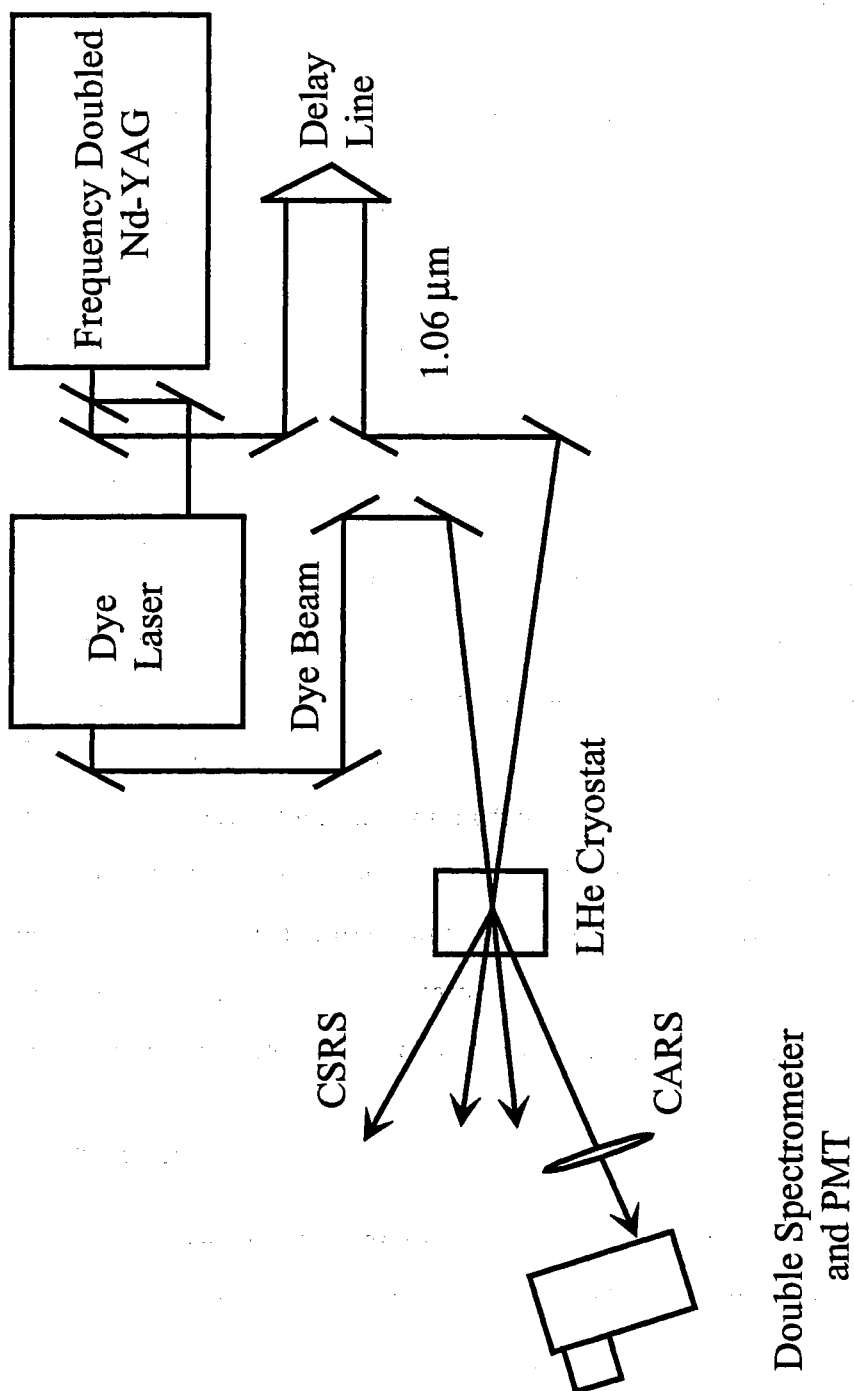


Figure 26. System diagram for NDFWM spectroscopy. The  $1.06\mu\text{m}$  beam from the fundamental of the Nd-YAG is mixed within the sample with the IR dye laser beam. This generates two beams in the directions  $2\vec{k}_1 - \vec{k}_2$  and  $2\vec{k}_2 - \vec{k}_1$ . The  $2\vec{k}_1 - \vec{k}_2$  beam is collected and sent into a spectrometer.

The delay line is used to ensure that the pulses from the two lasers overlap in time. This is necessary since the dye laser introduces a significant delay in the pulse. The overlap in time was achieved by monitoring the scattered light from a card at the sample position using a fast photodiode (from ThorLabs Inc., with a rise time of  $\sim 2$  ns). The delay was varied until the two pulses overlapped on an oscilloscope.

The samples were mounted in a temperature controllable, closed-cycle liquid helium cryostat which allowed temperatures down to about 10 K to be achieved.

As discussed in the previous section, the four-wave mixing interaction allows two signal beams to be generated, one in the direction  $2\vec{k}_1 - \vec{k}_2$  and another in the direction  $2\vec{k}_2 - \vec{k}_1$ . For the case shown, with an infrared (IR) dye mixed with the  $1.06 \mu\text{m}$  beam from the Nd-YAG, and with the  $\vec{k}_1$  wave identified with the dye laser beam, the  $2\vec{k}_1 - \vec{k}_2$  wave is referred to as the anti-Stokes' beam. The  $2\vec{k}_2 - \vec{k}_1$  wave then corresponds to the Stokes' beam. In the case of a Raman-type resonance, these beams are referred to as the CARS (coherent anti-Stokes' Raman Scattering) and CSRS (coherent Stokes' Raman Scattering) beams, respectively [79]. As noted in the previous section, some authors use these names in the general sense for all NDFWM spectra.

The signal is collected and focused into a double spectrometer (ISA DH-10) with a photomultiplier tube (Hamamatsu 928R). The signal is then sent to a boxcar averager. A computer program was written to coordinate the scanning of the dye laser, the scanning of the spectrometer and the data acquisition of the boxcar averager. Typically, the boxcar is allowed to average 30 shots per point on a NDFWM spectrum. A reflection of the dye beam is monitored using a photodiode.

### Single-photon resonances

In Fig. 27, the NDFWM spectrum is shown at room temperature (a) and at 175 K (b). The sample in this case is a  $360 \mu\text{m}$  film grown on sapphire. The electric fields are all parallel to the (100) direction in the CdTe, so that  $\chi^{(2)}$  effects may be ignored. Note that the spectra is considerably shifted as the temperature

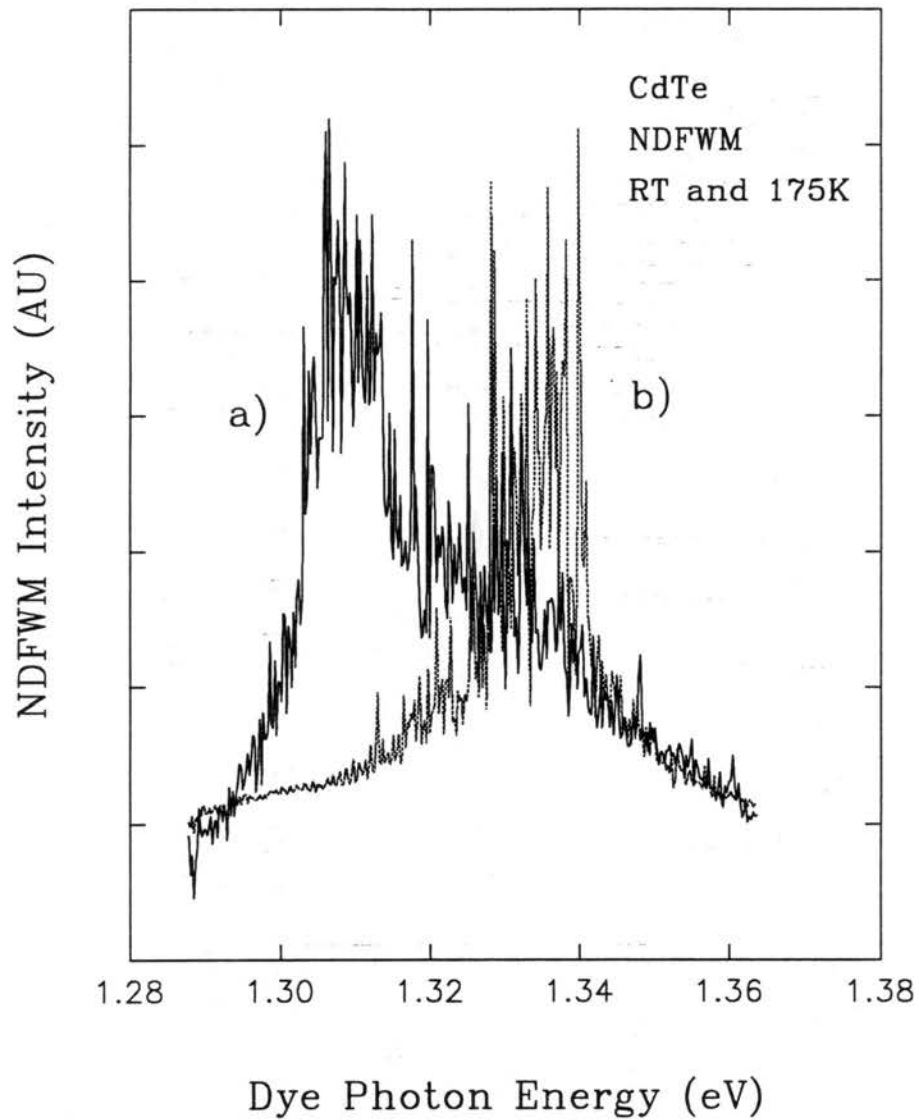


Figure 27. Nondegenerate FWM for CdTe is shown. The curve marked a) is taken at room temperature and the curve marked b) at 175 K. This resonance is due to an outgoing single-photon resonance with the CdTe band gap. Note the energy shift with temperature change.

is lowered. The energy diagrams for this process are shown in Fig. 27. As can be seen from this figure, there are many possible contributing processes to  $\chi^{(3)}$ . Another possible contributing factor is free carrier absorption. In this case, the emitted beam may be partially reabsorbed and thus contribute to the carrier density. These carriers, in turn can absorb photons from the interacting beams. This effect is especially important in longer pulses [86]. The governing equations for a single beam in this case may be written [86]

$$\frac{dI}{dz} = -\alpha I - \beta_2 I^2 - \sigma_c N I, \text{ and}$$

$$\frac{dN}{dt} = \frac{\beta_2 I^2}{2\hbar\omega} - N\gamma_{rec},$$

where  $I$  is the irradiance,  $\alpha$  is the linear absorption, and  $\beta_2$  is the two-photon absorption. Additionally,  $N$  is the carrier density,  $\sigma_c$  is the carrier absorption cross section, and  $\gamma_{rec}$  is the recombination rate of the free carriers. The last term in the last equation has been added from that given in Ref. [86] because of the additional complication here of pulses which are comparable to the lifetime of the carriers. The two equations must be solved simultaneously for a single beam propagating in the material if the photogenerated carriers may not be ignored. However, in single-photon resonant NDFWM, the situation is yet more complicated because of the depletion of the pump beams, as well as absorption of the generated beam.

### Two-photon resonances

The situation for two-photon resonances only is much simpler if the absorption due to two-photon generated carriers are ignored. Following Ref. [86], this factor will be ignored due to the large critical irradiance ( $I_c$ ). The critical irradiance is the value of irradiance such that the carrier absorption is equal to that arising from multiple photon processes. Van Stryland *et al.* estimate  $I_c > 10 \text{ GW/cm}^2$  [86] for ZnSe at  $1 \mu\text{m}$ . In this study, all of the power densities used were considerably below this value. For ZnSe at room temperature NDFWM can be used to find the value of  $\chi^{(3)}$  using the well-known Raman mode in calcite as a reference [85]. The  $\chi^{(3)}$  spectrum for bulk ZnSe is shown in Fig. 29. The oscillations are due to



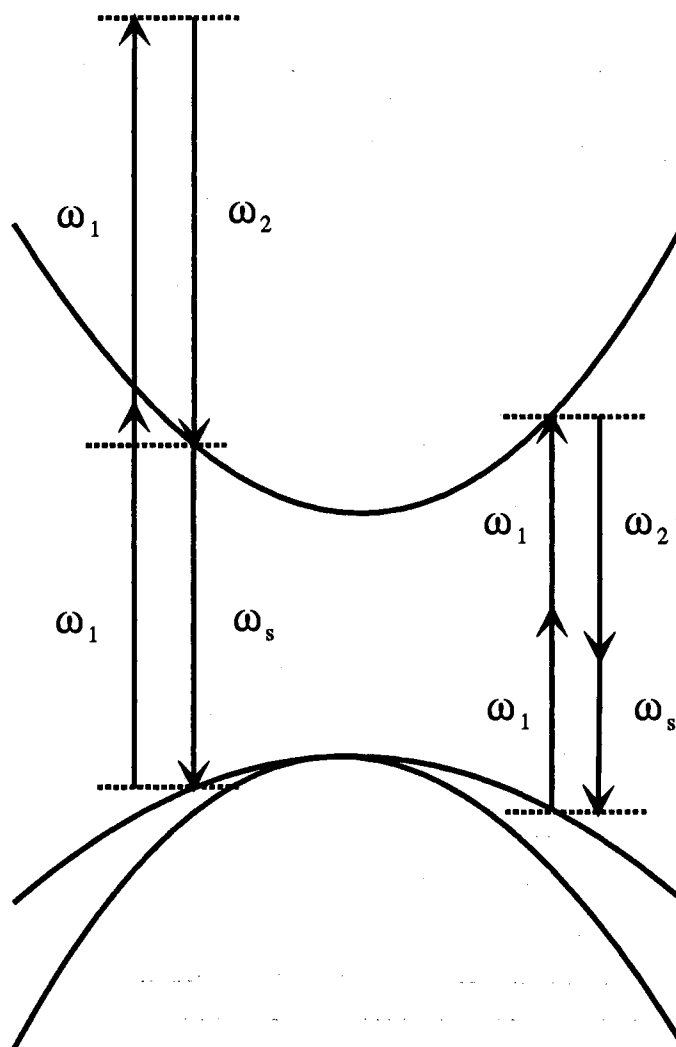


Figure 28. The energy diagram for NDFWM in CdTe in the near-infrared regime. This spectra illustrates the possibility of an outgoing resonance, and incoming single- and two-photon resonances.

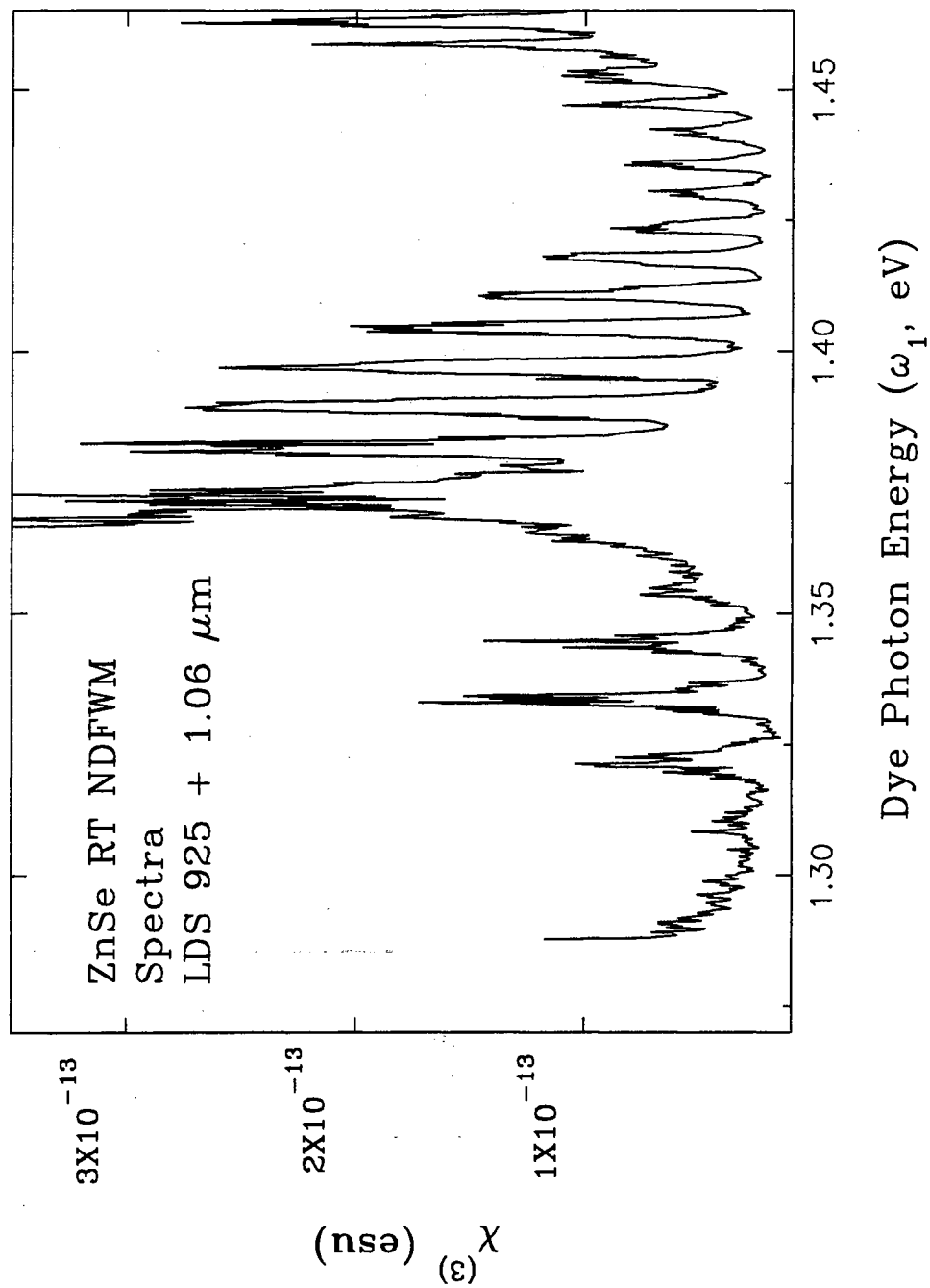


Figure 29. The  $\chi^{(3)}$  spectrum of ZnSe in the near-infrared. The oscillations are due to the phase-matching condition. The actual values of  $\chi^{(3)}$  are the values at the peaks.

the phase matching condition, and the peaks are the values of  $\chi^{(3)}(\omega_s, \omega_1, \omega_1, \omega_2)$ , where  $\omega_s$  is the signal photon frequency,  $\omega_1$  is the frequency of the dye laser beam, and  $\omega_2$  is the frequency corresponding to the 1.06  $\mu\text{m}$  Nd-YAG beam.

The use of NDFWM as a spectroscopic tool is illustrated in the  $T = 10$  K spectrum of a ZnCdSe/ZnSe QW (sample D58) as shown in Fig. 30. The sample is grown on a ZnSe substrate, so that both the linear absorption and the NDFWM can be done in a transmission type geometry. This is not the case for the ZnCdSe/ZnSe QW's grown on GaAs substrates, which were studied using TP-PLE as discussed earlier. The spectra shows a broad peak which is similar to that seen in the TP-PLE spectra, except that no clear evidence of a  $2p$  exciton peak is observed.

### Conclusions

The NDFWM technique allows the determination of  $\chi^{(3)}$  over a wide range of photon energies. Single photon resonant NDFWM spectra has been observed in a CdTe. In this case, the outgoing emission is resonant with the band gap of CdTe. The two-photon resonant contributions have been observed in ZnSe at room temperature. The incoming ( $\omega_1$ ) photons are TP resonant with the bands in bulk ZnSe.

Two-photon resonant NDFWM has also been observed in a ZnCdSe/ZnSe QW at 10 K. The  $1\text{HH}-1e$  continuum can be observed in the NDFWM spectra of a ZnCdSe/ZnSe sample, but the associated  $2p$  exciton is not resolved. A factor that may contribute to the difficulty in observing the  $2p$  resonance in the ZnCdSe/ZnSe samples using the NDFWM technique is the existence of two different HH exciton resonances. This will tend to wash out any higher lying excitonic resonances.

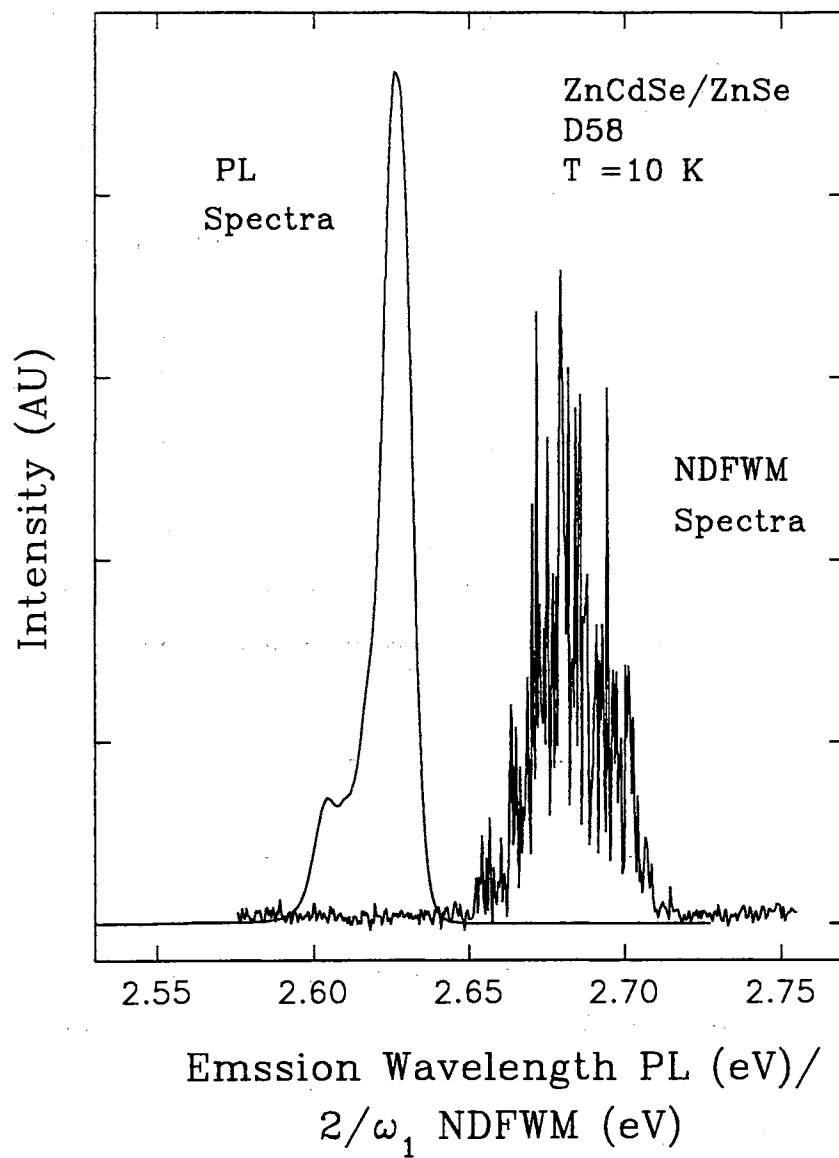


Figure 30. Two-photon resonant spectrum of a ZnCdSe/ZnSe QW (sample D58). Shown superimposed over the NDFWM spectrum is the PL spectrum of the sample.

## CHAPTER III

### Stimulated emission and gain measurements in CdTe grown by molecular beam epitaxy

#### Introduction

Cadmium Telluride is an important II-VI compound which has found applications in such devices as electro- and acousto-optic modulators, and solar cells. [87] It is also commonly used as a substrate or buffer material for  $\text{Hg}_{1-x}\text{Cd}_x\text{Te}$ , a material used for infrared (IR) detectors [87] and IR lasers. [88,89] Despite its common usage, much of the optical properties of CdTe are not well understood. This is especially true of the details of stimulated emission (SE). Much of the early work in this field was done using electron beam excitation, [90,91] but these studies were hampered by the lack of high quality samples. Recently, high quality samples have been grown, especially using molecular beam epitaxy methods. [92,93] Bulk CdTe and MBE grown films have been studied, and strong SE in all the MBE films studied has been observed. The unetched bulk sample did not exhibit SE, while the etched bulk sample exhibited SE, but also showed strong saturation effects. [94]

#### Brief theory

The pumping scheme used in this study is schematically represented in Fig. 31a, where the conduction and valence bands of CdTe are represented as parabolic bands. Perhaps the simplest defensible model for this pumping scheme is a four-level model as shown in Fig. 31b. Note, however, that this model does not take into account the states that lie between the pumped and emitting states. This means that the pumped states for a semiconductor will empty faster than the emitting

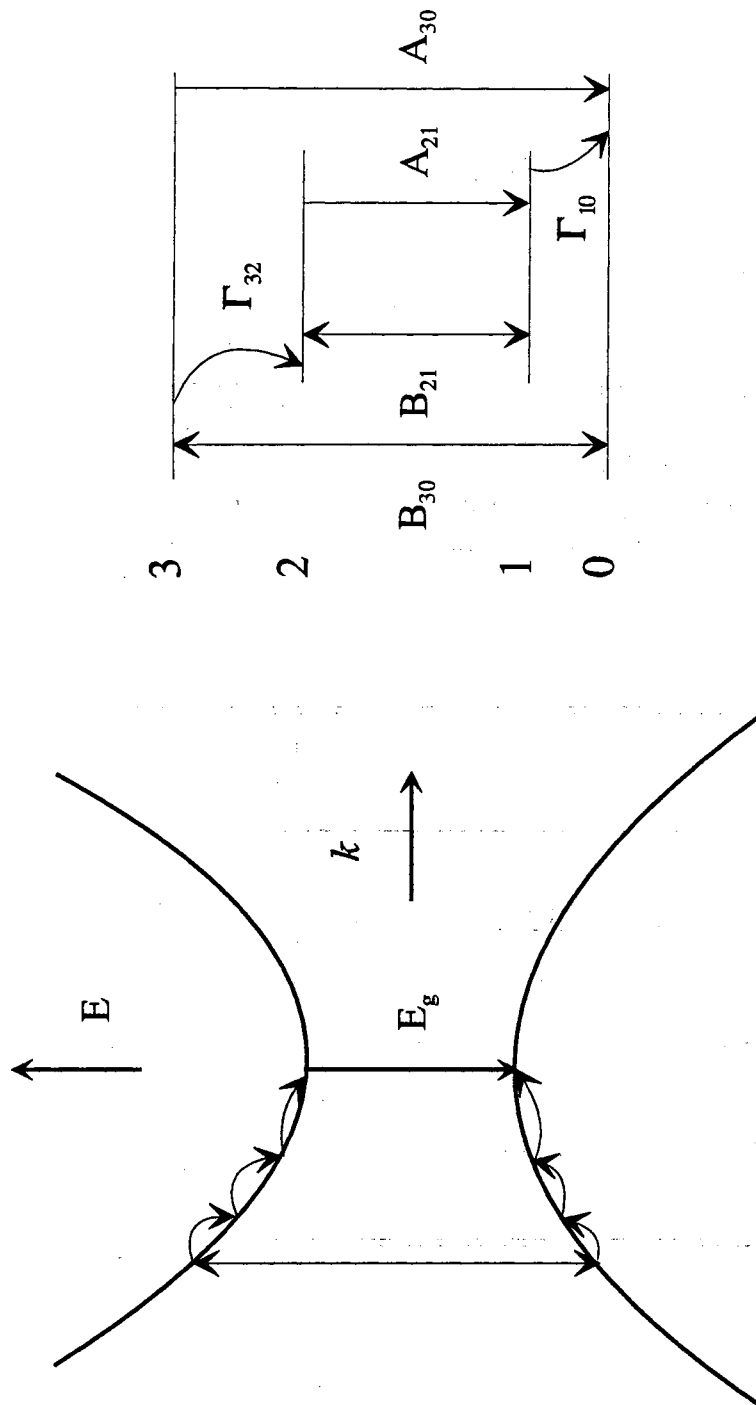


Figure 31. Excitation and stimulated emission for a two-band semiconductor is illustrated in a). The system may be modeled as a four-level system as shown in b). Despite the obvious inaccuracies, the model describes the behavior quite well.

states fill. The four-level model will therefore be a limiting case in describing the stimulated emission behavior of a semiconductor. In this model, a two-band model will be assumed and the Coulombic attraction between the electrons and holes ignored. Despite these assumptions and obvious inaccuracies in the model, it will be seen that the model predicts the observed stimulated emission behavior of CdTe quite well for relatively low power excitation and in the saturation regime.

The model presented here is an amalgam of the procedures found in Milonni and Eberly's book, *Lasers* [95] and in Loudon's book, *The Quantum Theory of Light* [96]. The states are as labeled in Fig. 31b. The populations of the states are denoted as  $N_i$ , where  $i$  is the state index. The time rate of change of the populations under a incident field are governed by the so-called rate equations. Referring to Fig. 31b, the appropriate rate equations can be written by inspection,

$$\begin{aligned}
 \frac{dN_0}{dt} &= N_3 A_{30} + \Gamma_{10} N_1 + B_{30} \overline{W}_p (N_3 - N_0) \\
 \frac{dN_1}{dt} &= N_2 A_{21} - \Gamma_{10} N_1 + B_{21} \overline{W} (N_2 - N_1) \\
 \frac{dN_2}{dt} &= -N_2 A_{21} + \Gamma_{32} N_3 - B_{21} \overline{W} (N_2 - N_1) \\
 \frac{dN_3}{dt} &= -N_3 A_{30} - \Gamma_{32} N_3 - B_{30} \overline{W}_p (N_3 - N_0),
 \end{aligned} \tag{95}$$

where the  $\Gamma_{ij}$  are the (not necessarily radiative) relaxation rates from state  $i$  to state  $j$ . The  $A_{ij}$  and the  $B_{ij}$  are the well-known Einstein  $A$  and  $B$  coefficients, respectively, denoting the spontaneous emission and the stimulated emission and absorption, from and to the indexed states. The mean energy density is written as  $\overline{W}_p$  (at  $\omega_{30}$ ) and  $\overline{W}$  (at  $\omega_{21}$ ), with the subscript denoting the pump. The populations are related by  $N_T = N_0 + N_1 + N_2 + N_3$ .

The change in the energy density of the fields due to the material should also be considered. Propagation equations may be written for a volume  $V$  of area  $A$  and length  $dz$  if conservation of energy is considered [96]:

$$\begin{aligned}
 \frac{d\overline{I}(\omega_{30})}{dz} &= \frac{d\overline{W}_p(\omega_{30})}{dt} = -(N_0 - N_3) \frac{B_{30} \overline{W}_p}{n^2 V} \hbar \omega_{30} F(\omega_{30}) \\
 \frac{d\overline{I}(\omega_{21})}{dz} &= \frac{d\overline{W}(\omega_{21})}{dt} = -(N_1 - N_2) \frac{B_{21} \overline{W}}{n^2 V} \hbar \omega_{21} F(\omega_{21}).
 \end{aligned} \tag{96}$$

In the above equation, the rate of change with distance of the time averaged intensity is assumed to be equal to the time rate of change of the mean energy density in the fields. The mean energy density,  $\bar{W}$ , and the time averaged intensity,  $\bar{I}$  are related by  $\bar{W} = n\bar{I}/c$ .

The rate equations and the propagation equations given above can be simplified if it is assumed that state 3 empties rapidly, i.e., that  $N_3 = 0$ . This is a good approximation in semiconductors since LO phonon emission can occur on the order of a few hundred of femtoseconds, and acoustic phonon emission on the order of several hundred fs., rapidly reducing  $N_3$  [51]. The rate equations become [95]

$$\begin{aligned}\frac{dN_0}{dt} &= -B_{30}\bar{W}_p N_0 + \Gamma_{10}N_1 \\ \frac{dN_1}{dt} &= B_{21}\bar{W}(N_2 - N_1) - \Gamma_{10}N_1 + N_2A_{21} \\ \frac{dN_2}{dt} &= -B_{21}\bar{W}(N_2 - N_1) + B_{30}\bar{W}_p N_0 - N_2A_{21}.\end{aligned}\quad (97)$$

Note that in the third equation above the population pumped into state 3 is assumed to immediately appear in state 2. The propagation equations are given by

$$\begin{aligned}\frac{d\bar{I}(\omega_{30})}{dz} &= -N_0 \frac{B_{30}\bar{W}_p}{n^2V} F(\omega_{30}) \\ \frac{d\bar{I}(\omega_{21})}{dz} &= -(N_1 - N_2) \frac{B_{21}\bar{W}}{n^2V} F(\omega_{21}),\end{aligned}\quad (98)$$

so that there can be no stimulated emission from state 3 to state 0.

If steady state conditions are assumed, and if it is assumed that  $\Gamma_{10} \ll A_{21}$  (which is similar to the assumption that  $N_3 = 0$ ), it is found, by combining the rate and propagation equations, that

$$\frac{1}{\bar{I}} \left[ 1 + \frac{B_{21}n\bar{I}}{cA_{21}} \right] \frac{\partial \bar{I}}{\partial z} = - \frac{B_{30}\bar{W}_p N_0}{\Gamma_{10}} \frac{B_{21}\hbar\omega F(\omega)}{Vcn}.\quad (99)$$

Making the appropriate substitutions, this can be written in the form

$$\frac{1}{\bar{I}} \left[ 1 + \frac{\bar{I}}{I_c} \right] \frac{\partial \bar{I}}{\partial z} = g.\quad (100)$$

If  $\bar{I} \ll I_c$ , then this equation becomes

$$\frac{1}{\bar{I}} \frac{\partial \bar{I}}{\partial z} = g,\quad (101)$$



which has solutions of the form

$$\bar{I} = \bar{I}_0 \exp(gz). \quad (102)$$

Eq. 102 should be recognized as the well-known small signal gain equation [95]. In the "small signal" regime, therefore, the emitted intensity varies exponentially with the excitation length.

If, on the other hand,  $\bar{I} \gg I_c$ , then it is seen that the solution is

$$\bar{I} = \bar{I}_0 + \bar{I}_c z, \quad (103)$$

which describes the saturated gain behavior of a stimulated transition [96]. This equation shows that the emission intensity is directly proportional to the length of excitation after the onset of saturation.

### Experimental

The CdTe epilayers were grown at Hughes Research laboratories by O.K. Wu. The thicknesses of the CdTe films varied between 2.0 and 2.4  $\mu\text{m}$ . The surface quality of the MBE samples was such that it was not necessary to subject the samples to any post-growth processing such as annealing in a Cd atmosphere or etching of the surface layers. The bulk samples were obtained from Eagle Picher Laboratories. The samples were cleaned with trichloroethylene and mounted on a cold finger in a LHe closed cycle cryostat. All data were taken with the samples at 10 K, using a pulsed dye laser at 1.771 eV. Pertinent growth and stimulated emission data for the samples studied is tabulated in Table IV.

The excitation system consisted of a Nd-YAG pumped dye laser, with 8 ns pulses with a repetition rate of 10 Hz. The dye used was LDS698. The excitation energy, 1.771 eV (700 nm), was chosen to be well above the band gap (1.604 eV at 10 K). The detection system consisted of a triple spectrometer, an optical multichannel analyzer (OMA), and a charge-coupled device (CCD) system. The samples were studied using both backscattering and side-pumping configurations. The excitation of the samples performed using the side-pumping configuration

TABLE IV. List of the samples, growth information and stimulated emission peaks observed. Samples IV and V are bulk samples. The "<" signs indicate that these peaks are observed to undergo significant red-shifting. The parentheses indicate that this peak is only seen under very high excitation power densities and certain lengths of excitation.

Sample	Substrate	Surface	SE peaks (eV)
I	CdTe	MBE	1.591, 1.580, (<1.576)
II	CdZnTe x=0.04	MBE	<1.576
III	CdZnTe x=0.04	MBE	1.591, 1.580, <1.576
IV	...	unetched	...
V	...	etched	1.577-1.591

consisted of a cylindrical lens for focusing the excitation beam in a line on the surface of the sample, as shown in Fig. 32. The line of focus was parallel to the optic axis of the signal collection optics. The excitation beam was normal to the optic axis of the signal collection optics, so that the emission from the sample was collected from the edge of the sample. The spectral dependence upon the power density was studied by varying the power density over nearly 4 orders of magnitude, using neutral density (ND) filters in steps of ND 0.1. The gain measurements were performed by varying the length of the excitation beam using a knife edge mounted on a micrometer, in the side-pumping configuration. [97,98]

### Stimulated emission studies

Figure 33 shows backscattering data taken at a pump energy of 1.771 eV at different pump powers. The data set is from sample I (see Table IV). At low powers, the major emission peak appears at 1.591 eV. This peak labeled A is close in energy to a bound exciton commonly seen in CdTe with good surface characteristics. [99] Peak A is seen to be over taken at higher powers by a lower energy peak at 1.580 eV, which is labeled B in Fig. 33. The intensity of peak B increases at a much greater than a linear rate. This peak shows broadening but does not show significant red-shifting as the power density is increased. The side-pumping data from the same sample (Fig. 34a) with the same excitation energy shows peak B dominating the spectrum even at low pumping powers. The reasons for this difference between the two spectra are attributed to both reabsorption of the peak A at 1.591 eV and preferential gain of the peak B at 1.580 eV. At the onset of SE, peak B has a full-width half maximum (FWHM) of less than 5 meV. This value increases to  $\sim 10$  meV at high powers. Fig. 34b shows a high excitation ( $\sim 1$  MW/cm<sup>2</sup>) spectrum of this sample. At this excitation power, the emission at 1.580 eV clearly dominates the spectral features. At excitation power densities in excess of 2 MW/cm<sup>2</sup>, a lower energy peak at 1.576 eV arises under certain experimental conditions as will be discussed below. This peak showed evidence of red-shifting as the excitation power density was increased.

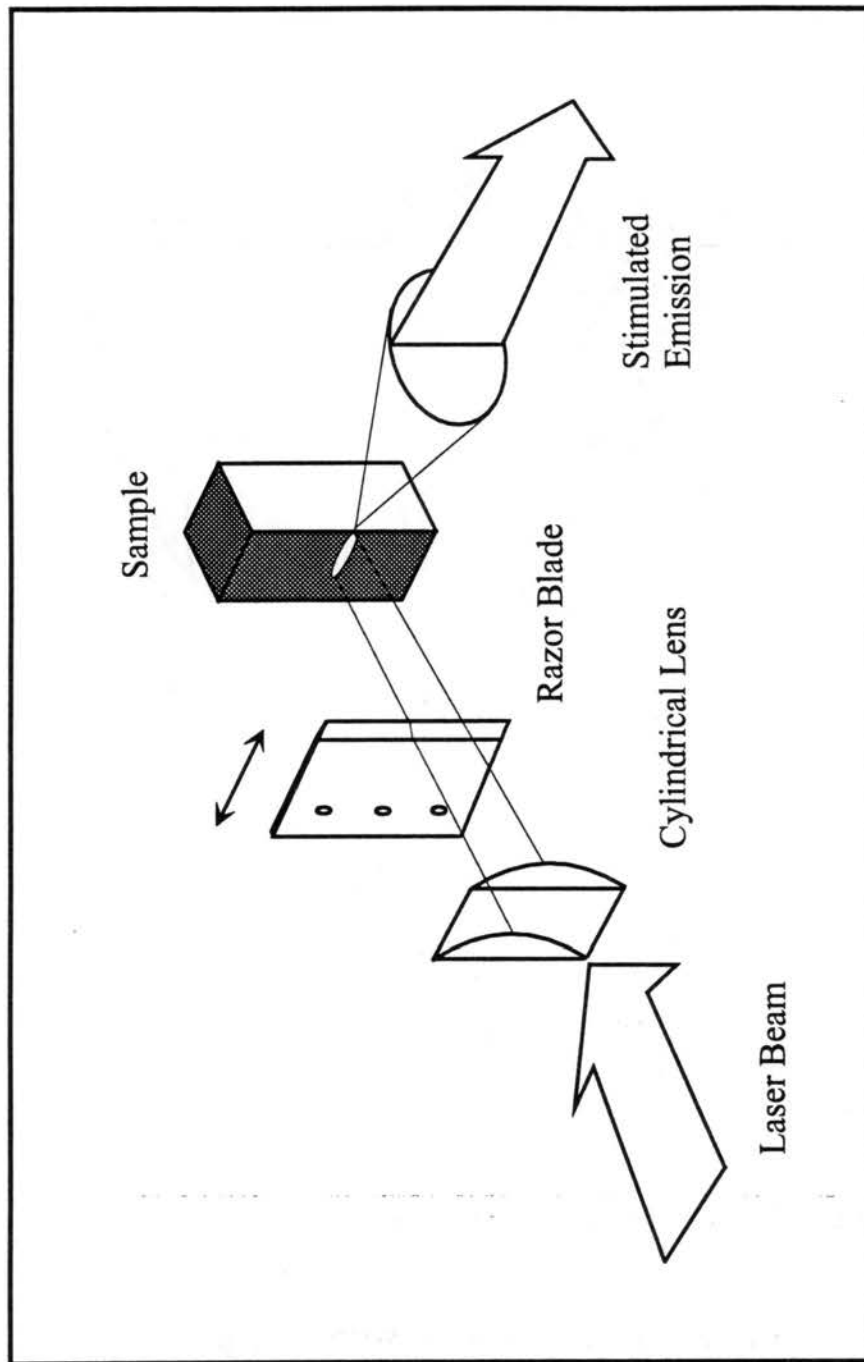


Figure 32. Side pumping configuration which allows determination of the gain values. The length of excitation can be varied to determine the gain at a specific emission energy.

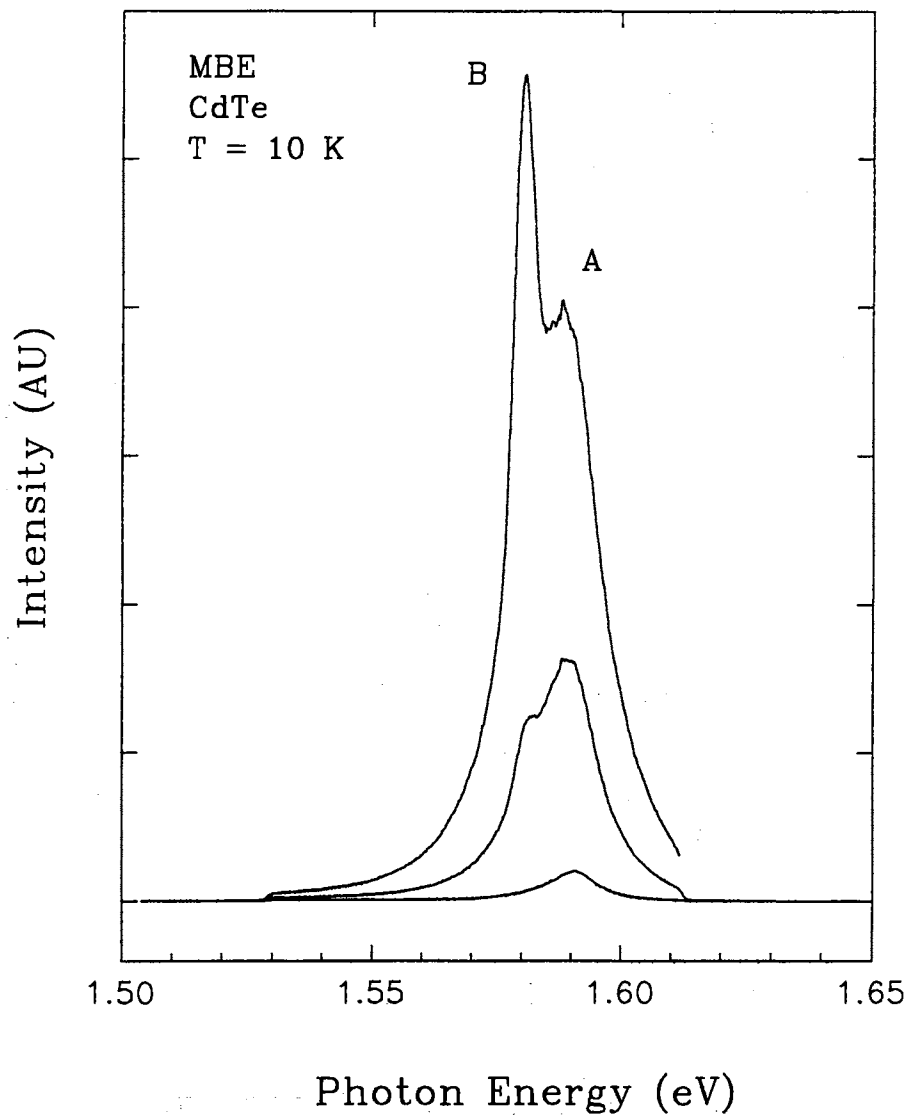


Figure 33. Backscattering data for sample I. The spectra shown here correspond to excitation power densities of 8, 32, and 82 kW/cm<sup>2</sup>. Strong emission seen at 1.591 eV is superseded at higher powers by a stimulated peak at 1.580 eV. Note the considerable broadening which is observed even at these moderate power densities.

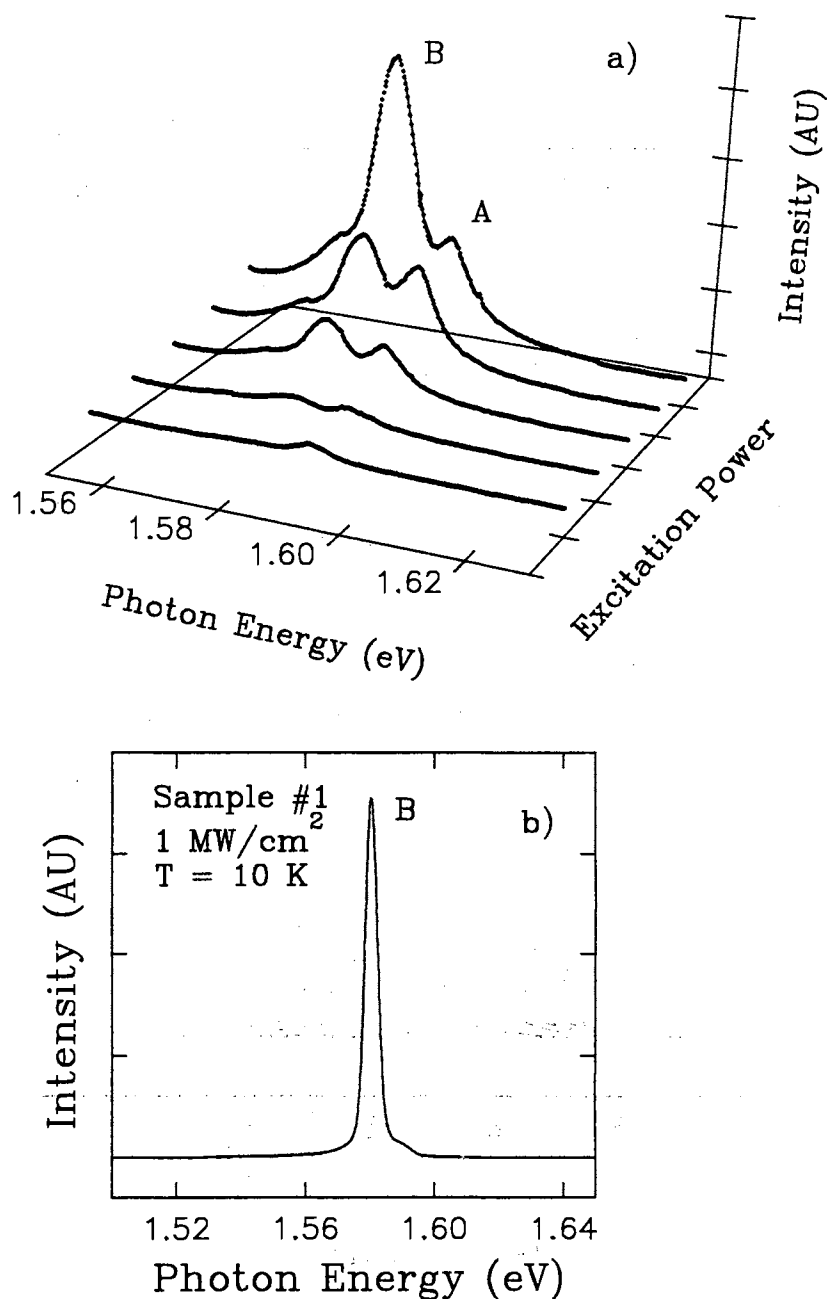


Figure 34. Side-pumping data from the same sample as the previous figure shows the onset of stimulated emission at 1.580 eV, as the power density is increased from 88 to 400 kW/cm<sup>2</sup>. Competition among the peaks is seen as the power density is increased. The spectra have been displaced for clarity. The stimulated peak at 1.580 eV at ~1MW/cm<sup>2</sup> is shown in b). This peak exhibits very little redshifting (~1-3 meVs) from the low power emission even at this excitation power.

Stimulated emission was also observed from sample II which was grown on a  $\text{Zn}_x\text{Cd}_{1-x}\text{Te}$  substrate with  $x = 0.04$ . No distinct stimulated emission peaks were observed at the energy positions of peaks A or B of sample I. Clear SE was observed, however, near the position 1.576 eV. The intensity change of this peak with the incident laser power is shown in Fig. 35 as an example of strong SE seen in MBE CdTe samples reported in this work. As seen in this figure, the emission from this sample shows an exponential dependence on the input power at relatively low ( $< 20 \text{ kW/cm}^2$ ) powers. Similar exponential dependence was also found with the SE peaks of the other samples in Table IV. It should be noted that these peaks are of a composite structure, and that the energies given are, for convenience of reference, for the peak values only.

The exponential dependence of the SE intensities is expected from elementary considerations due to the inclusion in the small signal gain equation of the population number of the excited and ground states. This can easily be seen from the well-known small signal gain equation, Eq. 102 given in the introductory section [95].

$$I(z) = I_0 e^{gz}, \quad (104)$$

where  $z$  is the length of excitation and  $g$ , the small signal gain is given by

$$g(\nu) = \sigma(\nu)(N_2 - (u_2/u_1)N_1), \quad (105)$$

where  $\nu$  is the emitted photon energy, while  $N_1$  and  $N_2$  denote the number of carriers in the lower and upper states, respectively. The factors  $u_1$  and  $u_2$  are the degeneracies of the lower and upper states, and  $\sigma(\nu)$  is the SE cross section at the frequency  $\nu$ . [95] It is clear that, for low excitation powers, the population should vary linearly with the excitation power density, and thus the emission intensity has an exponential dependence upon the excitation power density.

Stimulated emission of another MBE CdTe with ZnCdTe substrate, sample III was also investigated. Although the structure of this sample is similar to that of sample II, the substrate materials, ZnCdTe, were not cut from the same boule. The spectra measured from this sample are different from those of samples I or

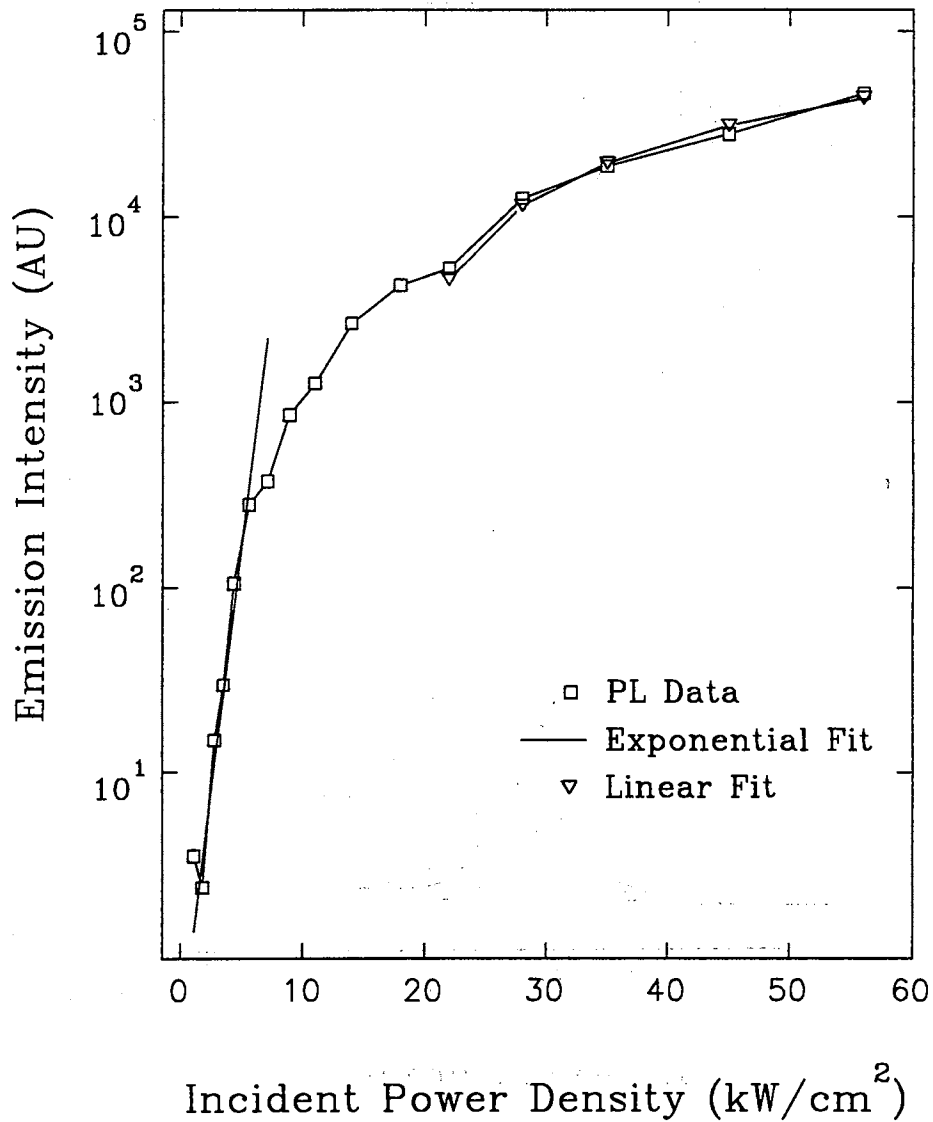


Figure 35. Semi-log plot of the integrated intensity of the 1.576 eV (at onset) peak as a function of incident power density, from sample II. At low powers an exponential increase in the emission intensity is seen, with a slope of 1.22. After the onset of saturation, the emission still displays supralinear behavior.



II. As seen in Fig. 36, peaks A and B appear in nearly the same energy positions of those in sample I. At low powers ( $<100 \text{ kW/cm}^2$ ), peak A is stimulated. It is the peak at 1.573 eV (peak C in Fig. 36), however, which shows the strongest emission at high powers. This peak C behaves very much like the SE peak detected in sample II. Note that the peak at 1.574 eV arises after the onset of saturation for the stimulated peak at 1.591 eV and then dominates the spectra at higher excitation power densities. In samples II and III, it appears nearly at the same energy position, and exhibits red-shifting and broadening with the increase of the pump power.

Fig. 37 shows the emission intensity -vs- incident power density for sample III. The top and bottom curves in the figure correspond to peaks C and A, respectively. Peak C is seen to arise and stimulate after the onset of saturation of peak A. In fact, peak C appears quite abruptly at  $\sim 180 \text{ kW/cm}^2$  in a region in which little emission is seen prior to its emergence. Also, in the cw photoluminescence (PL) spectra measured in this sample, no emission peak is found at this energy position, whereas strong PL peaks appear above this peak in the bound-exciton region. [100] From this observation as well as the significant red-shifting of peak C, the origin of peak C seems to be quite different from that of peaks A and B.

In order to see the effects of the substrates on the stimulated emission observed from the three MBE samples discussed above, emission from CdTe and CdZnTe bulk samples was also studied. For bulk CdTe, both unetched and etched samples (see Table IV) were investigated. For ZnCdTe, MBE samples were mounted on the copper sample block with the substrate side up.

The unetched bulk sample, sample IV, was not observed to undergo SE. The emission was found to be restricted below the bound exciton band, in the region  $<1.57 \text{ eV}$  at all power densities studied. The etched bulk sample, sample V, however, showed SE at multiple peaks in the region 1.577-1.591 eV, as shown in Fig. 38. This sample also exhibited significant saturation effects, and was not observed to stimulate at or below 1.573 eV, i.e., no structure appears that shows behavior similar to peak C. In the low energy region (1.53  $\sim$  1.57 eV) of this sample,

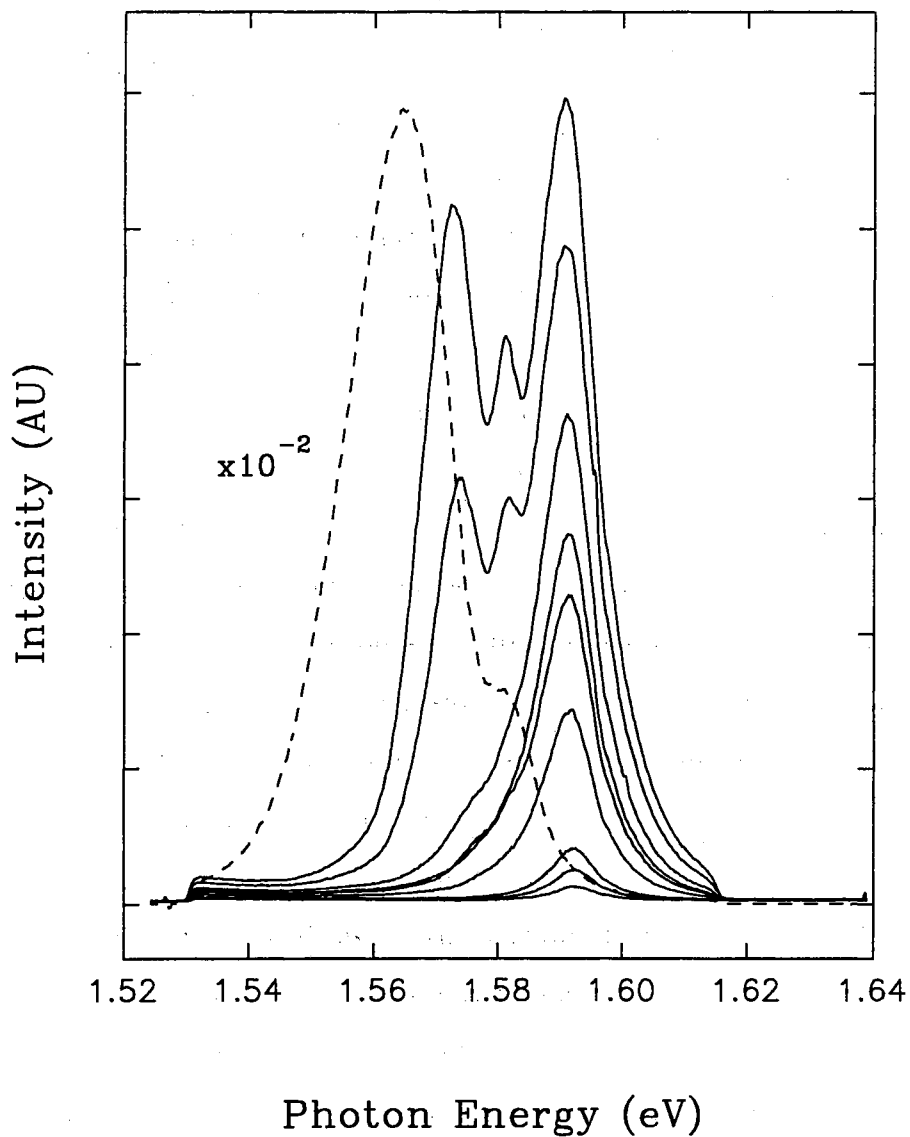


Figure 36. Spectral dependence upon the incident power density for sample III. The power densities for the spectra are 9, 14, 22, 35, 56, 110, 140, 180, 220, 280  $\text{kW}/\text{cm}^2$ , in increasing order. Note the onset of stimulated emission from a lower energy (1.573 eV) peak between 180 and 220  $\text{kW}/\text{cm}^2$ . This low energy peak undergoes significant (more than 10 meVs) red-shifting as the power is increased.

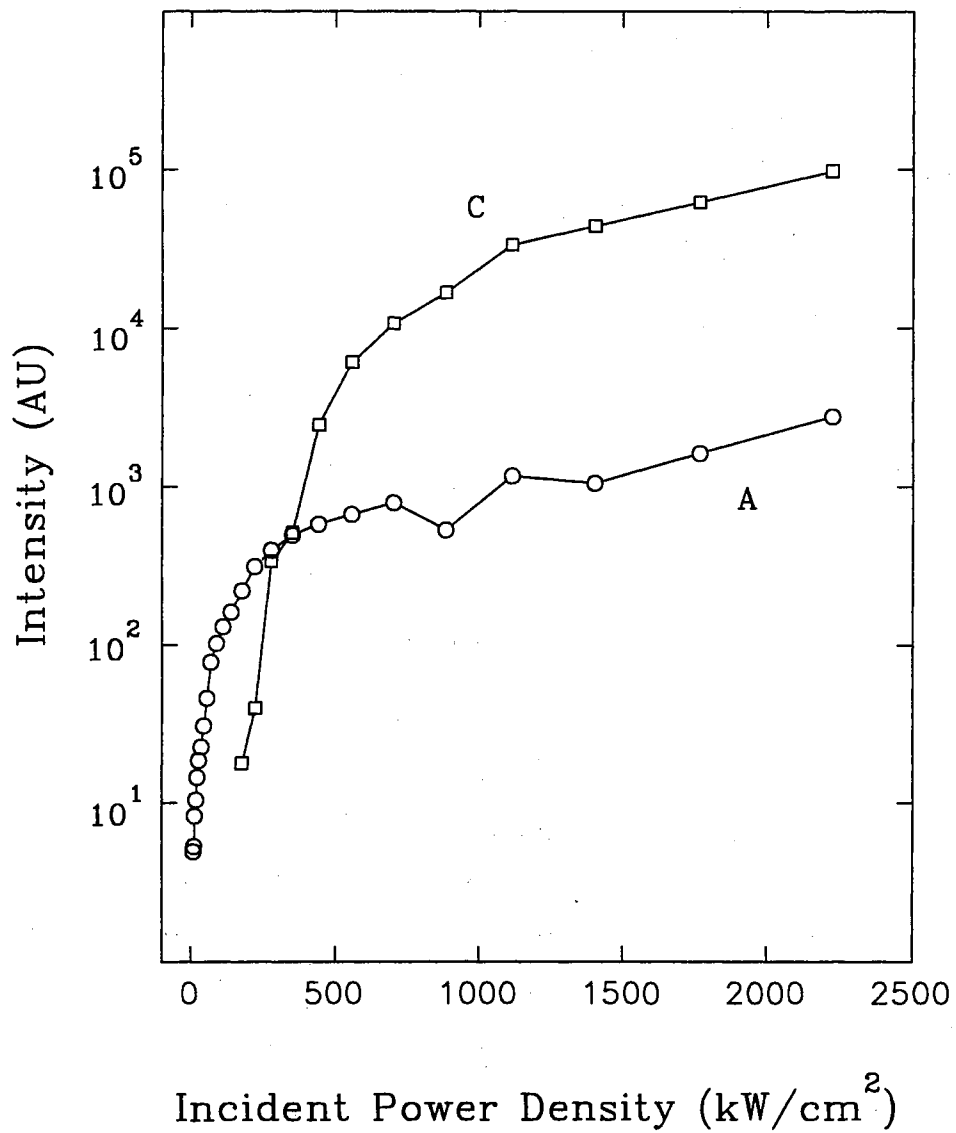


Figure 37. Semi-log plot of the emission intensity as a function of incident power density for the same sample as in the previous figure. Note that the peak at 1.574 eV arises after the onset of saturation for the stimulated peak at 1.591 eV and then dominates the spectra at higher excitation power densities.

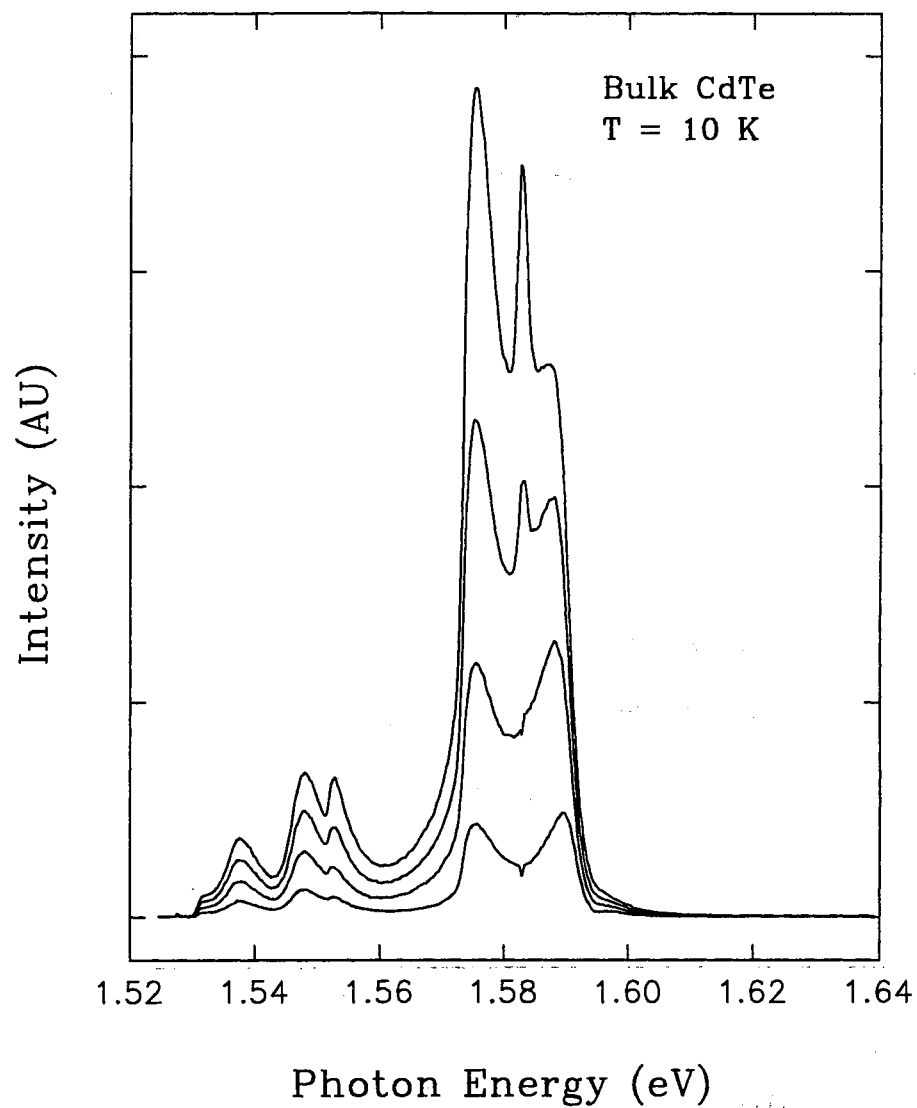


Figure 38. Power dependence of the etched bulk CdTe sample. Stimulated emission occurs at 1.580 and 1.577 eV. The power density varies from 1.2 to 5.9kW/cm<sup>2</sup>. Note the overall increase in the impurity emission as compared to the MBE grown samples.

several strong impurity- related emission peaks were found whereas little emission was noted in the same energy range with all three MBE samples. The lack of SE in the unetched sample as well as the differences in the spectra between the etched and unetched CdTe bulk samples are ascribed to complex surface related processes. These surface effects are well known in CdTe and have been studied by many different groups. [101] The ZnCdTe substrate showed emission at 1.621 eV, well above the band-gap of CdTe (1.604 eV at 10 K), and also exhibited no stimulated emission. No appreciable emission from this sample was seen in the bound exciton region of CdTe or below. This result implies that the SE seen in the CdTe/ZnCdTe samples is due to the CdTe thin film and not due to the substrate via carrier diffusion. This result is to be expected since the band gap of the ZnCdTe substrate is greater than that of the CdTe epilayer. This will cause the carriers to be confined within the epilayer.

Although the etched CdTe sample exhibited stimulated emission, the rate of SE signal growth with the power change in sample V was much less than those of MBE samples. In the exponential gain region which corresponds to the straight line shown in the low power region of Fig. 36, the emission signal was found to have  $\exp(AI)$  dependence where A is a constant. For MBE samples, the constant A, varied from 0.08 to 1.22 for the different energy peak positions. In the etched sample, the A value was only 0.13. After the onset of saturation in sample V, the emission exhibited less than linear behavior with the power increase. None of the MBE samples showed such low emission growth rate beyond the exponential region. The MBE samples showed supralinear behavior at all the power densities investigated. These differences are probably due to surface sample quality of MBE samples as well as the differences in the details of impurity concentrations.

### Optical gain measurements

Optical gain measurements were performed by variation of the length of excitation at a fixed power density, as is illustrated in Fig. 32. The resulting spectra were curvefitted assuming Gaussian lineshapes to separate out the different

contributions to the SE. This procedure is necessary due to the redshifting and broadening of the low energy peaks and because of the occurrence of the multiple overlapping stimulated peaks mentioned above. This procedure yielded peak energies different from those stated above and in Table IV. This is due to the fact that the SE peaks are actually a collection of states in a region of energies. As an example, the spectral variation of sample I with length of excitation is shown in Fig. 39. The excitation power density was relatively low ( $\sim 23 \text{ kW/cm}^2$ ). The spectra show the commonly observed redshifting with an increase of the excitation beam length [97]. The values of the length,  $l$ , ranged from 140 to 500  $\mu\text{m}$  in this figure. Beyond 500  $\mu\text{m}$ , saturation effects dominate and the emission increases little. The largest gain in this figure was found to be  $\sim 750 \text{ cm}^{-1}$  in the region of peak A at  $\sim 1.587 \text{ eV}$ . At higher powers and large  $l$  values, however, peak B dominates the SE spectra. This value of the gain at  $\sim 1.587 \text{ eV}$  corresponds closely to the maximum reported in Ref. [102], of  $780 \text{ cm}^{-1}$  for bulk CdTe. The authors of this reference ascribe the SE observed in their studies to the growth of an electron-hole plasma.

The optical gain can be obtained from the slope of the line in the linear portion of the semi-log plot for emission intensity versus length of excitation, as shown in Fig. 40. The curves shown here are representative of the optical gain observed in this sample (sample I), and display the differences between the different peaks. The higher energy side of the emission spectra shows the highest gain and the lower energy side the lowest at this excitation power density. As mentioned previously, the emission in the small signal gain regime is given by Eq. 102,  $I(l) \sim \exp(gl)$ , where  $g$  is the signal gain and  $l$  is the length of excitation. [98,95] The gain for the different peaks was calculated using a linear least-squares-fit.

The emission intensity -vs- length of excitation plot for sample III is shown in Fig. 41. The peak C at 1.575 eV is the only peak that shows gain ( $55 \text{ cm}^{-1}$ ) at this excitation power density of  $2 \text{ MW/cm}^2$  due to saturation effects of the other peaks. This observation suggests that for samples with multiple emission regions, "small signal" levels which mentioned above are relative. Here the small signal regime is taken to be simply that region of power density, for a given emission peak, which is

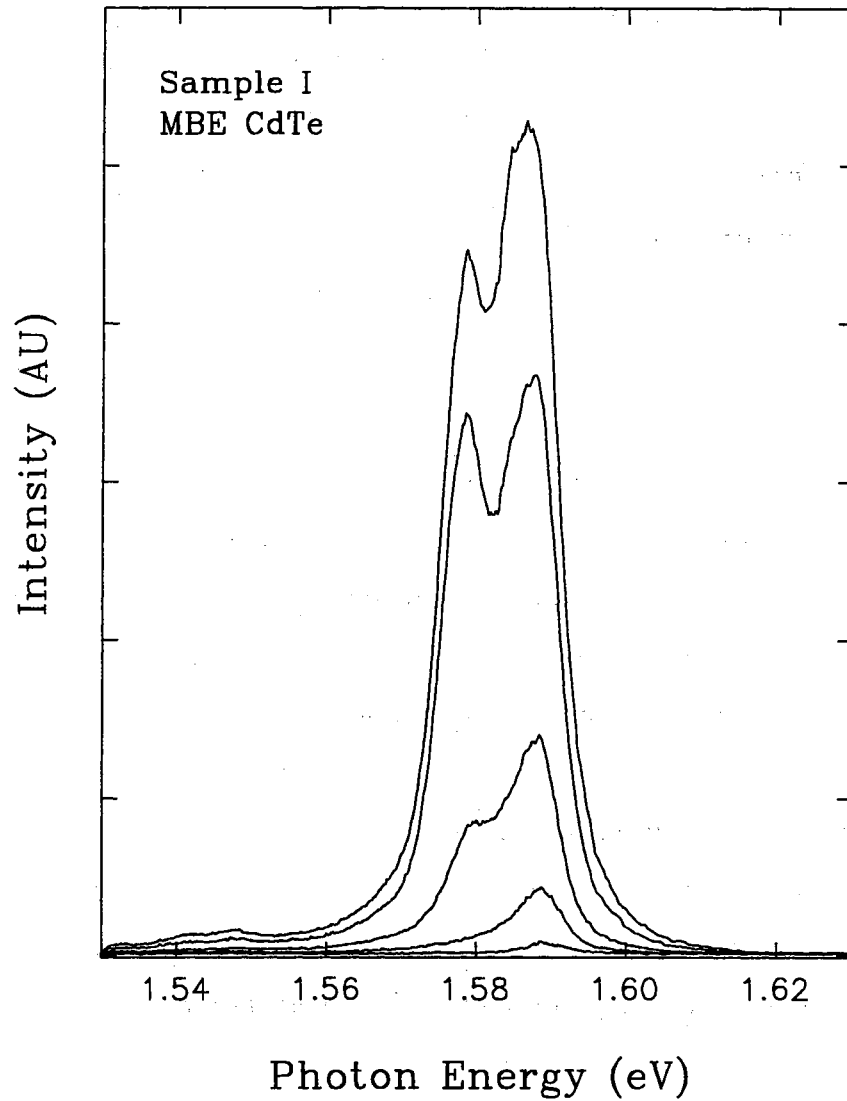


Figure 39. Spectral dependence of the homoepitaxially grown sample (sample I) on excitation length. The sample shows the common redshifting of the spectrum with an increase in the length. The length was varied in this figure from  $140 \mu\text{m}$  to  $500 \mu\text{m}$ . After this point, saturation effects dominate and the emission increases little.

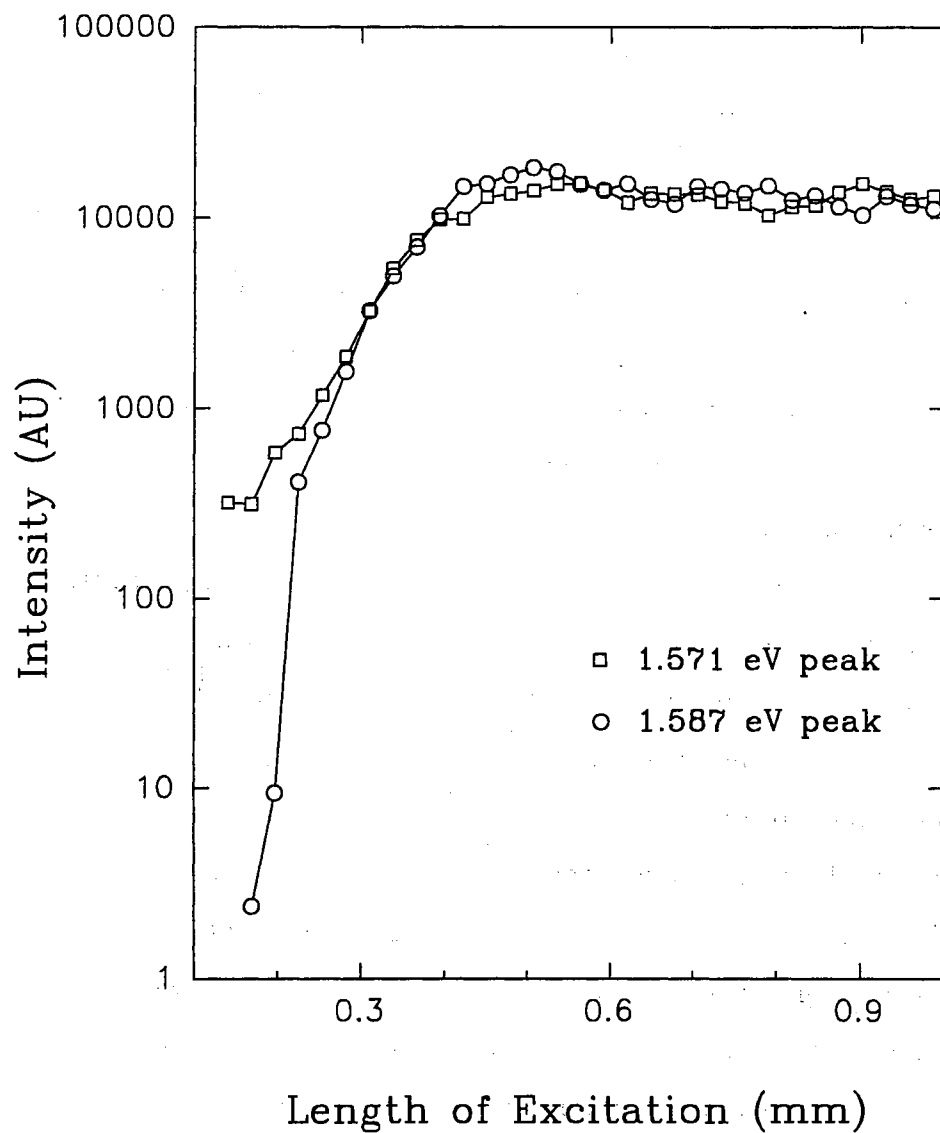


Figure 40. Semi-log plot of emission intensity as a function of excitation length for sample I. The curvefitted peaks show different gain behavior at this excitation power ( $23 \text{ kW/cm}^2$ ).



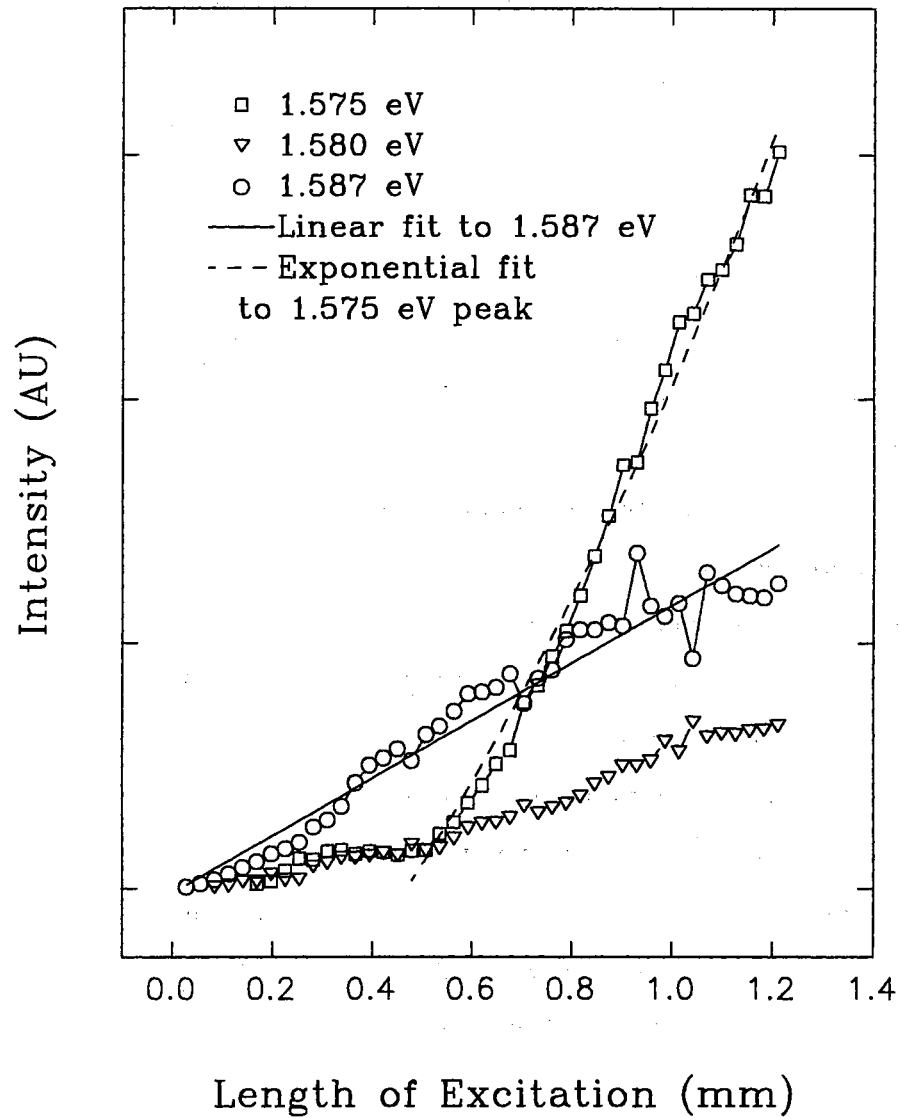


Figure 41. Linear plot of excitation length -vs- emission intensity for sample III, showing the saturation behavior at  $\sim 2$  MW/cm<sup>2</sup>, so that only the lowest energy peak C at 1.575 eV is not saturated at this power density. The other peaks follow linear behavior.

not dominated by saturation effects. For a given material and emission peak, the calculated gain is a function of the power density. This is especially true of samples in which competing SE processes occur, such as is seen in CdTe. The inverse of this is also true. That is, the spectral dependence on the power density is a function of the length of excitation. [103] This complicating factor was alluded to earlier in the presentation of the spectra for sample I. At certain lengths of excitation for this sample it is possible to observe the onset of a peak in the region of peak C at excitation powers in excess of  $2 \text{ MW/cm}^2$ . At other lengths of excitation this peak is not seen. This behavior was not observed in the other samples, although it is possible that such a behavior exists and was not noted.

### Conclusions

The observed differences in the spectra, power dependence, and calculated gain between the MBE samples studied is probably due to differences in defect concentration. The identity of these defects remain to be understood. Among the possibilities are lattice defects caused by the lattice mismatch between the thin film and the substrate, or diffusion of impurities from the substrate into the thin film during the MBE growth.

The observation of broadening without red-shifting of the peaks A ( $\sim 1.580 \text{ eV}$ ) and B ( $\sim 1.591 \text{ eV}$ ) respectively, implies that the radiative transition is more efficient at these energies than the nonradiative relaxation processes which would yield emission at lower energies. The reason for this is unclear, but is probably related to the number of intrinsic defects in the samples. The stimulated emission seems to result from at least two different processes, one involving a bound exciton or an impurity state, and another possibly involving the formation of an electron-hole plasma (EHP) [103,102,104], or a carrier scattering process. The identification of the higher energy emission, i.e., at  $1.591 \text{ eV}$  and  $1.580 \text{ eV}$  as recombination of an exciton bound to an impurity or impurity complex is mostly circumstantial, in that the emission is seen to occur in or just below the exciton band. Strengthening this identification is the small (1-3 meVs) red-shifting and narrow line width of the

SE at these energies. Bound exciton related SE has been reported previously in CdS. [105] The higher energy SE is probably not due to a EHP process because of the low power density threshold for stimulation at these energies, and the above mentioned narrow line width as well as the lack of significant peak shift. The lower energy emission at 1.576 eV and below compares favorably, with regards to its onset and evolution, to emission seen in other II-IV compounds where SE has been ascribed to the formation of an EHP. [103,104] Such an identification, however, has often been controversial. The CdTe epilayers grown on ZnCdTe substrates show this behavior due to the carrier confinement due to the greater band gap of the substrate. This will cause greater carrier densities due to the suppression of diffusion, encouraging the growth of the EHP.

In summary, strong stimulated emission (SE) has been observed in all MBE grown CdTe films studied. The MBE fabrication process enhances the SE, possibly due to the good surface quality, or perhaps a lessening of the concentration or type of impurity as compared to the bulk. The saturation effects observed do not seem to be as dominant as those seen in bulk CdTe, with the MBE samples showing supralinear behavior for all power densities studied above threshold. The etched bulk CdTe sample exhibited less than linear behavior after the onset of saturation. Stimulated emission from the MBE film has been observed in two distinct regions, in the bound exciton band, 1.591 eV-1.580 eV, and at a lower energy, below 1.576 eV. There are at least two regions at which the MBE films stimulate in the vicinity of the exciton band. The lower energy SE at  $< 1.576$  eV does not appear to correspond to any emission peaks seen at low power densities. The bulk CdTe sample was observed to stimulate at only one emission region in the bound exciton band. Gain measurements resulted in moderate ( $55 - 750 \text{ cm}^{-1}$ ) values which differed for the different peak energies. The emission spectra exhibited red-shifting with increased excitation length and power density.

## CHAPTER IV

### Photoluminescence of bulk and thin films of ZnSe

#### Introduction

In recent years the II-VI compound semiconductors have attracted much attention for their technological importance appropriate for optoelectronic devices such as semiconductor diode lasers and light-emitting diodes (LEDs). [106,107] ZnSe is one of the most extensively studied II-VI materials due to its zinc-blende structure with a band gap of  $\sim 2.7$  eV at room temperature which gives the promise of fabricating diode lasers and LEDs operating in the blue color range. [108–115] To achieve the ultimate goal of a current injection diode laser it is necessary to grow both n-type and p-type conducting ZnSe materials for the preparation of p-n junctions. There have been reports of the achievement of blue light-emitting devices from ZnSe based single quantum-well structures on GaAs substrates under pulsed current injection at relatively low temperatures. [45–47] However, the built-in biaxial strain resulting from the lattice mismatch and the different thermal expansion coefficients of ZnSe and GaAs, as well as the chemical-valence mismatch which induces the formation of vacancy-rich  $\text{Ga}_2\text{Se}_3$  layer at the GaAs/ZnSe interface [116] can severely influence the device performance and shorten device operating lifetime. Indeed, it has been observed that the threading dislocations in the ZnSe/ $\text{Zn}_{1-x}\text{Cd}_x\text{Se}$  QW lasing structures are due to dislocations at the GaAs interface. [117] The successful commercial fabrication of reliable blue laser diodes and LEDs operating at room temperature with long operating lifetimes still relies on the preparation of heavy p- or n-type doped ZnSe and ZnSe-based materials or, possibly, the growth of homoepitaxial layers of ZnSe-based materials on ZnSe

substrates. The growth of homoepitaxial layers, however, does not avoid the fundamental problem of doping of the epilayer material or of the substrate. However, n-type bulk ZnSe materials can be grown [107], so that if p-type homoepitaxial layers can be grown, bulk p-type material need not be fabricated.

The defect states formed due to the introduction of impurities, either intentional or unintentional, dominate the electrical characteristics in an extrinsic semiconductor. As is discussed below, the impurities, in general, form states within the "forbidden" energy gap. These states become ionized at elevated temperatures, giving up a hole (acceptor states) or an electron (donor states) which is promoted to the valence or conduction band, respectively. These carriers are then available for conduction. It is therefore requisite to characterize these states (including the ionization energy) to calculate the resultant conductivity of the material.

Seeded physical vapor phase transport (SPVT) has been performed to grow high quality large size ZnSe at Eagle Picher Laboratories. [116] Using this technique, strain-free, relatively high-purity bulk ZnSe crystals may be grown. A study on the optical properties of ZnSe bulk crystals grown by the SPVT technique is reported here. Additionally, doping studies of ZnSe epilayers grown on GaAs substrates using MBE and atomic layer epitaxy (ALE) [118] are also performed. [118–121] Samples used in this investigation included bulk undoped as-grown and post growth treated (Zn extraction and Se enrichment treatments), intentionally doped (Ga, Cl, N) crystals, as well as ZnSe epilayers, undoped and doped with Li. Photoluminescence (PL) measurements were performed to qualitatively evaluate the purity of nominally undoped ZnSe samples and characterize the intentionally doped samples by monitoring the notable near-band-gap bound-excitons (BE),  $I_1$ ,  $I_1^d$ ,  $I_2$ ,  $I_3$  and donor-acceptor pair (DAP) emission bands at lower energies. [122]

### Theoretical

The near-band gap photoluminescence spectra of a semiconductor consists of the emission from different transitions as shown in Fig. 42. Band-to-band emission may occur, especially at elevated temperatures where the other states

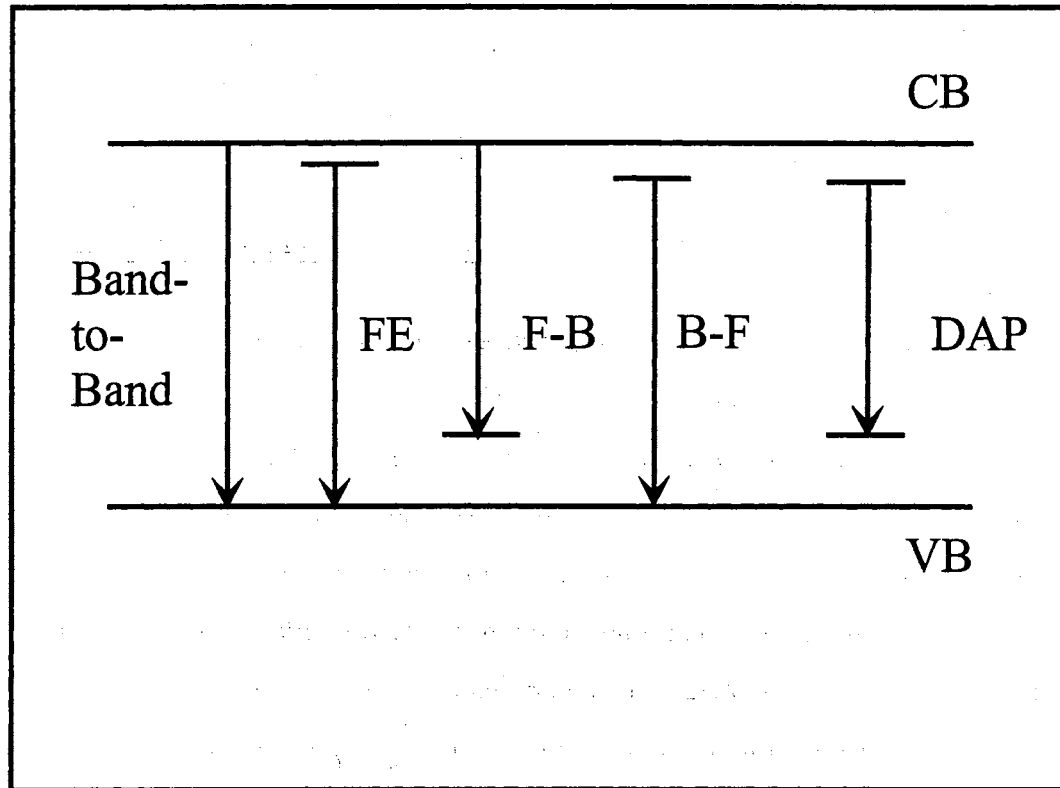


Figure 42. Near-band gap luminescent transitions in a semiconductor include band-to-band transitions, free and bound exciton emission. Emission may also be seen arising from free to bound transitions, bound to free or donor-acceptor pair recombination.

are not stable. Free excitons (FE) are sometimes observed, especially in high quality samples at low temperatures. Bound excitons (BE) may be formed if the free excitons become trapped on an impurity site (neutral or ionized). Emission related to the impurity sites themselves may be observed, i.e., free-to-bound (F-B) to acceptor states or bound-to-free (B-F) from donor states. Additionally, donor-acceptor pair emission (DAP) may be observed. The band-to-band emission is governed by the same matrix elements discussed in Chapter I for absorption, as is the FE state.

The impurity states can be described using the envelope function approximation in a manner analogous to the development given in Chapter 1 for excitons. The development here will be given for donor states. The wave function of an electron bound to a donor may be written as a sum over the Bloch states with wavevector  $\vec{k}$ :

$$\psi(\vec{r}_e) = \sum_{\vec{k}} a_{\vec{k}} \psi_{c\vec{k}}(\vec{r}_e). \quad (106)$$

In the above equation,  $\psi_{c\vec{k}}(\vec{r}_e)$  is the wave function for an electron in the conduction band of wavevector  $\vec{k}$ . The Schrödinger equation is written

$$\left[ -\frac{\hbar}{2m_e^*} \nabla_e^2 + V_G(\vec{r}_e - \vec{r}_d) \right] \psi(\vec{r}_e) = E\psi(\vec{r}_e). \quad (107)$$

The envelope function is determined as in Chapter I:

$$\phi(\vec{r}_e) \equiv \frac{1}{Vol} \sum_{\vec{k}} a_{\vec{k}} \exp[i\vec{k} \cdot \vec{r}_e], \quad (108)$$

and the  $a_{\vec{k}}$  determined by the Fourier transform

$$a_{\vec{k}} = \frac{1}{Vol} \int_{Vol} d\vec{r}_e \phi(\vec{r}_e) \exp[i\vec{k} \cdot \vec{r}_e]. \quad (109)$$

The Schrödinger equation for the envelope function is written as [123]

$$\left[ -\frac{\hbar}{2m_e^*} \nabla_e^2 + V_G(\vec{r}_e - \vec{r}_d) \right] \phi(\vec{r}_e) = (E - E_g) \phi(\vec{r}_e),$$

where the Coulombic potential is given by

$$V_G(\vec{r}_e - \vec{r}_d) = -\frac{e^2}{\epsilon |\vec{r}_e - \vec{r}_d|}.$$

The solutions to the above equation are again given by those for hydrogen, with appropriate substitutions made for the effective mass and dielectric constants. [123,14,124] The energy is given by [14,123,124]

$$E_n = -\frac{R_H^*}{n^2} = -\frac{13.6}{n^2} \left[ \frac{1}{\epsilon} \right]^2 \left[ \frac{m_c^*}{m} \right],$$

$$R_H^* = \frac{(e^2/4\pi\epsilon)^2}{2(\hbar^2/m_c^*)}$$

where  $R_H^*$  is the effective Rydberg energy and  $n$  is the principle quantum number. The effective Bohr radius is given by [14,123,124]

$$a_H^* = \frac{m\epsilon}{m_c^*\epsilon_0} a_{0H} = 0.529\epsilon \left[ \frac{m}{m_c^*} \right],$$

$$a_{0H} = \frac{\hbar^2/m}{e^2/4\pi\epsilon_0}.$$

The hydrogenic model gives donor ionization energies,  $E_{i,H}^d$ , of about 26.4 meV for ZnSe using  $m_c^* = 0.147$  [125] and  $\epsilon = 8.7$  [126]. The effective Bohr radius using these parameters is 31.3 Å. Various values have been calculated in the literature [107,110,14], mostly dependent upon the value of  $\epsilon$  used. Hydrogenic calculations for CdTe yield donor ionization energies of about 11.6 meV. [14] Acceptor energies and wavefunctions may be determined in an analogous way, although with the additional complication of degenerate bands at  $\vec{k} = 0$ . [63] Assuming that the heavy hole dominates due to its greater mass,  $E_{i,H}^A = 88$  meV and  $a_H^A = 9.4$  Å. Previous calculations give about 108 meV for the acceptor state ionization energy. [107]

The hydrogenic model gives reasonable ranges of values for the donor and acceptor levels, but it fails to describe the variation of the ionization energies for differing impurity species. The ionization energies differ because the Coulombic potential is a good approximation only at large distances away from the impurity site. The details of the potential at small distances become especially important for the ground state since it is held in a tighter orbit around the impurity site. This energy is also the most important to determine since it is the energy which needs to be considered in the temperature dependence of the conductivity of a



semiconductor. However, as will be seen below, this shortcoming of the hydrogenic model can become a tool in determining the impurity species in semiconductors.

The ground state (ionization) energies for both donors and acceptors may be determined experimentally in a number of ways. The most direct is the temperature dependence of the conductivity, since the conductivity will be directly proportional to the number of carriers in the bands. The number of carriers, in turn, is dependent upon the temperature following Boltzmann statistics (and ignoring compensation effects): [127]

$$N \simeq \sqrt{n_0 N_d} \exp \left[ \frac{-E_d}{2k_B T} \right],$$

where

$$n_0 = 2 \left( \frac{m_e^* k_B T}{2\pi \hbar^2} \right)^{3/2},$$

and  $N_d$  is the donor concentration. [127]

The ground state energy level of an impurity may be determined through low temperature and/or temperature dependent photoluminescence studies. As shown in Fig. 42, the ground state of an acceptor may be determined directly by observation of the recombination of a free electron and the neutral (unionized) acceptor state, which is denoted ( $e-A^0$ ). Similarly, the donor state may be observed in luminescence by the recombination of a free hole and the unionized donor state ( $h-D^0$ ). This type of measurement may require temperature dependent studies in order to unambiguously identify the luminescent lines. [128]

Another possibility of determining the donor and acceptor ground state energies is by observation of the excitons which become bound to these states. Excitons bound to neutral donors and acceptors are denoted by ( $D^0, X$ ) and ( $A^0, X$ ), respectively. The emission energy of the excitons is modified to differing degrees dependent upon the ground state energy of the defect site. Haynes *et al.* empirically determined a general formula for the ionization energy of donors and acceptors in silicon. [129] Halsted and Aven have extended this relationship to include CdTe, ZnSe, ZnTe and CdS [130]. Haynes' rule for donor states in these II-VI compounds

is [130]

$$\frac{(E_{FE} - E_{BE})}{E_i^d} = 0.20,$$

and for acceptors

$$\frac{(E_{FE} - E_{BE})}{E_i^A} = 0.10,$$

where  $E_{FE}$  ( $E_{BE}$ ) is the recombination energy of the free exciton (bound exciton), and  $E_i^d$  ( $E_i^A$ ) is the ionization energy of the donor (acceptor) state. The term  $E_{FE} - E_{BE}$  is often denoted  $E_D$ , and is referred to as the dissociation energy. [129,130]

## Experimental

### Crystal growth and sample preparation

The seeded physical vapor phase transport growth technique can generally provide large size uniformly strain-free ZnSe single crystals. Basically, vapor phase growth technique takes advantage of the fact that II-VI compounds have significant elemental vapor pressures well below their melting point. As a result crystal growth can take place when a source of the compound is heated until the vapor pressures are significant and a temperature gradient is established such that transport of elemental vapors takes place to a cooler region in a growth ampoule where they are deposited. The recently developed seeded technique allows single crystals to be formed from the onset of crystal growth by placing a seed crystal in the cooler region. The volatile impurities are out-gassed prior to onset of crystal growth and the crystal growth is stopped before all of the source material is exhausted so that less volatile impurities will tend to remain in source rather than transport to the growing crystals. [116]

In attempts to dope shallow impurities such as Cl, Ga, and N in ZnSe, crystal growth runs were conducted by Eagle Pitcher Laboratories using doped ZnSe charges with different elements. ZnSe powder synthesized from high-purity Zn (99.9999%) and Se (99.9995%) was mixed with an appropriate amount of zinc chloride and melted in a pressure furnace to produce poly-ZnSe containing 200

ppm Cl. This was then mixed 10:1 with ZnSe to obtain the 20 ppm Cl doped ZnSe charge for SPVT growth. The Ga-doped ZnSe charges containing 1, 10, 50, and 100 ppm Ga for SPVT growth were prepared in a manner similar to that used in Cl-doped ZnSe growth. The Cl-doped SPVT growth resulted in single crystals. However, using the same method to grow Ga-doped ZnSe yielded polycrystalline material. Also, the color of the as-grown Ga-doped ZnSe has a reddish cast instead of the normal pale yellow cast of undoped ZnSe. A similar method was used to dope melt grown ZnSe. The N-doped SPVT ZnSe crystals were grown in an N<sub>2</sub> atmosphere with standard ZnSe charges.

Two post-growth treatments, Zn-extraction and Se-enrichment, were carried out (also at Eagle Picher Laboratories) on nominally undoped as-grown SPVT ZnSe crystals. The Zn-extraction treatment was performed by submersion of ZnSe crystals into molten Zn at 850°C for 96 hours. The Se-enrichment treatment was done by annealing the ZnSe wafers in selenium vapor produced in a closed quartz tube placed in a three zone furnace. The Se metal is heated in one zone to 700°C while the temperature of the ZnSe wafers is held at 930°C in another zone. The treatment time is 68 hours. All samples used for photoluminescence measurements were mechanically polished and then chemically etched with 0.5% bromine/methanol for 5 minutes to reduce the surface roughness.

The lithium doped ZnSe films were grown on GaAs by Takafumi Yao (at Hiroshima University), Ziqiang Zhu and Mitsuo Kawashimi (at Sumitomo Metal Mining Company). The growth techniques employed were MBE growth and atomic layer epitaxy (ALE).

### Photoluminescence measurements

Extensive photoluminescence (PL) measurements have been performed on ZnSe since Dean and Merz's measurement of the pair spectra and edge emission of ZnSe in 1969. [108] It has been found that the low-temperature luminescence spectra observed from nominally undoped ZnSe crystals were usually quite complicated, characterized by the emission lines from bound excitons denoted by I<sub>1</sub>,

$I_2$ ,  $I_3$ , and  $I_1^d$  in the near band-gap region. [109–113,131–134] The  $I_2$  lines have been well identified as originating from the recombination of excitons bound to neutral shallow donors with a luminescence peak at approximately 2.797 eV. The  $I_1$  lines have been considered as emission from excitons bound to acceptors, with the notable  $I_1^d$  line located at about 2.78 eV attributed to the recombination of excitons bound to deep acceptors such as Zn vacancies or substitutional impurities (e.g., copper on a zinc site, denoted  $Cu_{Zn}$ ), and the  $I_3$  line was proposed to be associated with the recombination of excitons bound to the ionized donors due to the peak position slightly lower than  $I_2$  in energy. [109,110] More recently, however, this identification has been called into question. Pressure and stress dependent PL have shown that this  $I_3$  line is due to donors which lie deeper than those which yield lines in the region of  $I_2$ . [115,135] In this section the PL measurement results data taken from various SPVT grown ZnSe samples is presented. In general, the low-temperature PL spectra of nominally undoped SPVT samples consist of a few strong bound-exciton emission lines such as  $I_2$ ,  $I_3$ , and  $I_1^d$  with its phonon replicas lying in the near band-gap region. The donor-acceptor pair recombination spectral signatures could be hardly observed from those samples. However, the PL spectra from the intentionally doped SPVT samples are characterized by relatively weak near band-gap bound-exciton emissions along with a broad emission band at lower energies.

The samples were mounted on the cold finger of a closed-cycle liquid helium cryostat with vacuum grease and cooled to 10 K. Photoluminescence was excited by the 325 nm line of a 10 mW HeCd laser. The PL spectra in this study were measured using a Spex 1000M monochromator with a GaAs photomultiplier tube (PMT) or a Spex 1877 Triplemate spectrometer with an intensified optical multi-channel analyzer (OMA) followed by a computerized data acquisition system.

Photoluminescence of bulk ZnSe. Figure 43 shows a typical PL spectrum from as-grown SPVT ZnSe crystals. The spectrum is dominated by the strong,

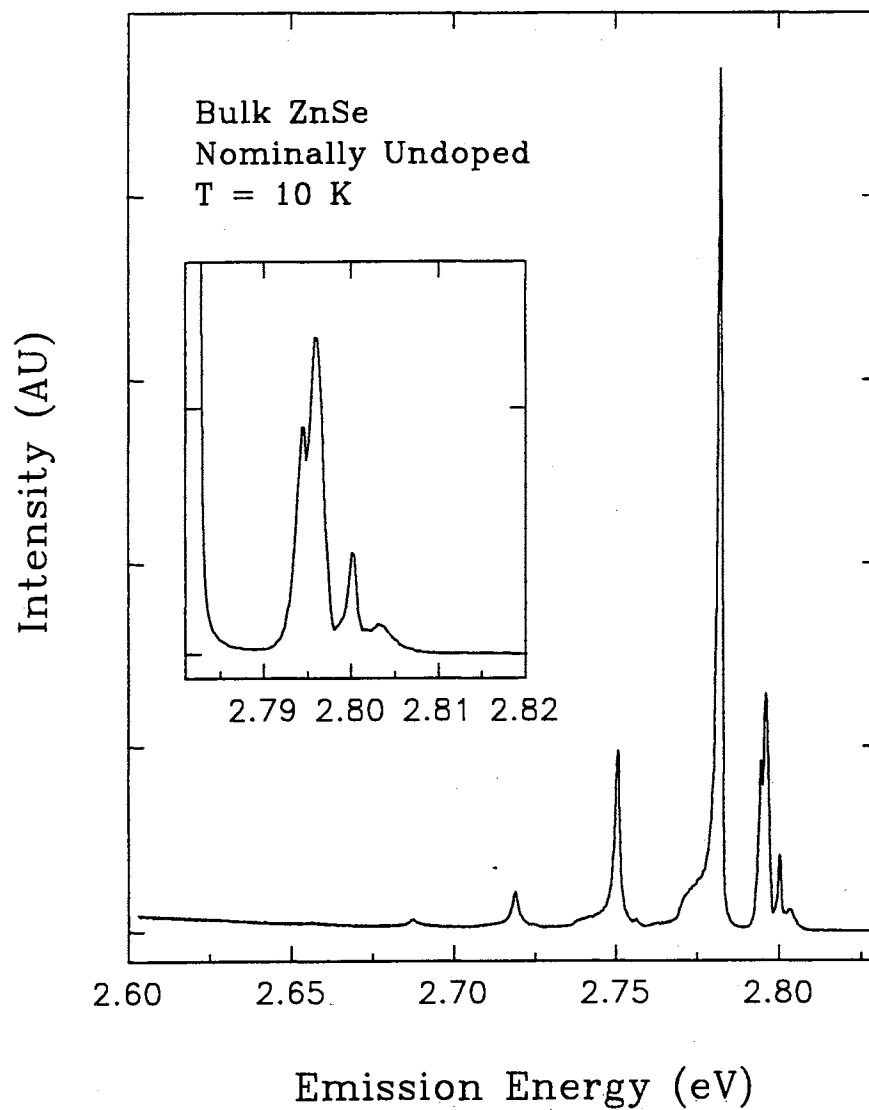


Figure 43. A typical PL spectrum from an as-grown ZnSe sample at 10 K. The strong  $I_1^d$  emission line and its LO phonon replicas are dominant and no DAP spectral features are observable.

sharp  $I_1^d$  emission line at 2.7821 eV and its LO phonon replicas which are observed at lower energies spaced by 31.6 – 31.7 meV. The shallow bound excitons  $I_2$  (2.7960) and  $I_3$  (2.7944 eV) are seen as is emission from the upper and lower polariton branches (2.8002 and 2.8034 eV, respectively). The  $I_2$  and  $I_3$  peak positions vary slightly from sample to sample. Haynes' rule applied to the observed  $I_2$  peaks yields donor ionization energies of 25 – 30 meV, which is consistent with the effective mass approximation as given above. Assuming that  $I_3$  is a deeper donor state, the ionization energy is 38 – 40 meV. The donor-acceptor pair (DAP) recombination spectral signatures [134,109] were not observed from the as-grown samples. The DAP emission band is often a strong feature of melt-grown specimens. The PL spectra of post-growth treated ZnSe samples are very different from those of as-grown samples as shown in Figs. 44 and 45 for Zn-extraction and Se-enrichment treatments, respectively. After the Zn-extraction treatment, the noteworthy spectral changes are that the emission intensity of  $I_1^d$  line is considerably decreased and the  $I_3$  line (2.794 eV) has the strongest emission intensity. If Haynes' rule is applied to this value for  $I_3$ , the binding energy of this donor state is 35.8 meV. A new emission peak appears at 2.7702 eV in Fig. 44. A phonon replica of this new peak is also observable. This spectral feature was previously identified as an LO phonon replica of the emission of free excitons in ZnSe with the acoustic phonon scattering of the  $I_1^d$  peak contributing. [109,136] However, this identification has been challenged recently. [113,137] In a study of ZnSe epilayers grown on GaAs, Shahzad et. al have suggested that this emission (labeled  $I_v^0$ ) is related to structural defects. [137] In this study, no correlation between the emission intensity of  $I_1^d$  and the emission at 2.7702 eV is observed, which is contrary to the identification of acoustic phonon scattering of  $I_1^d$ . The strong emission of  $I_1^d$  in the as-grown samples is most likely to be related to a large number of Zn vacancies and/or substitutional impurities such as  $Cu_{Zn}$ . [116,131,138] The drastic decrease of  $I_1^d$  luminescence intensity indicates that Zn-extraction treatment can reduce the concentrations of those acceptor-like deep centers. This result is consistent with both suggestions of the origin of  $I_1^d$ , that is, Zn vacancies or  $Cu_{Zn}$ . The

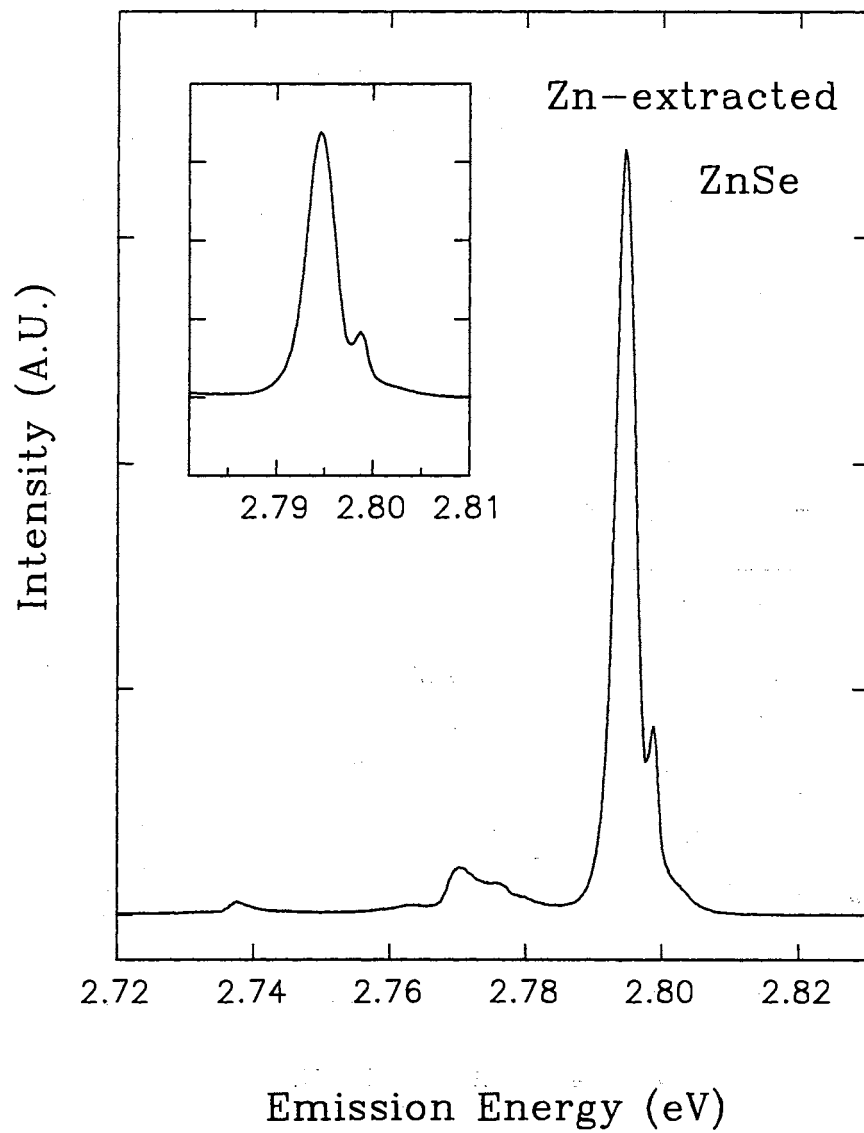


Figure 44. A spectrum of Zn-extracted ZnSe. The Zn-extraction treatment eliminates the  $I_1^d$  emission and  $I_3$  becomes the dominant feature.

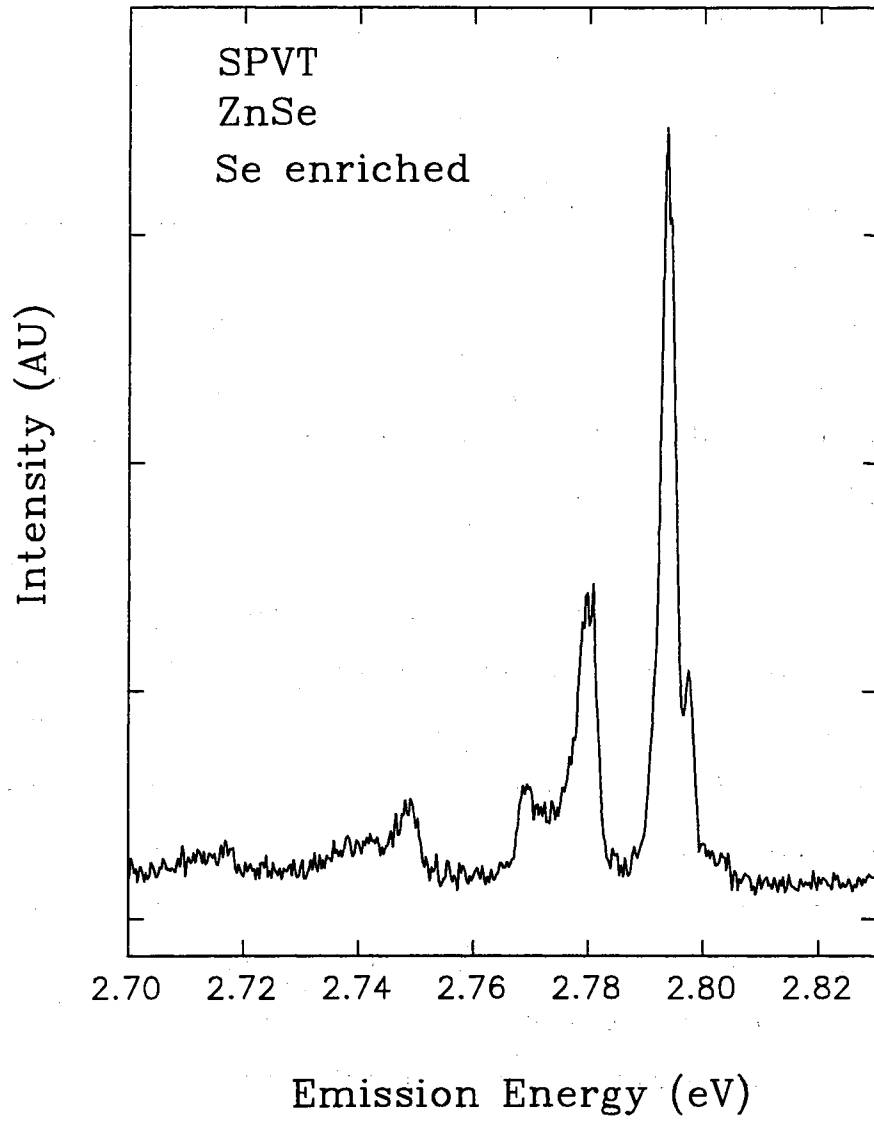


Figure 45. A spectrum of Se-enriched ZnSe. The Se-enrichment reduces  $I_1^d$  emission and  $I_3$  becomes the dominant feature. Note that the  $I_1^d$  peak is not eliminated as in the Zn-extracted samples.



PL spectra from the samples which have undergone Se-enrichment treatment show that  $I_2$ ,  $I_3$  emission lines become the pronounced features, while  $I_1^d$  is reduced but not eliminated. As mentioned above, the reduction of  $I_1^d$  emission in Zn-extracted samples is consistent with the current models for  $I_1^d$ . However, the reduction mechanism of the  $I_1^d$  emission in Se-enriched samples is more difficult to interpret. It is possible that the annealing and not the enrichment process itself is reducing the concentration of Zn vacancies. Samples which were subjected to Zn-extraction and Se-enrichment exhibit DAP peaks in addition to the  $I_2$  and  $I_3$  emission lines. A representative spectra is shown in Fig. 46, which shows a strong DAP peak at 2.706 eV, with 1 and 2LO phonon replicas of this peak at 2.675 and 2.644 eV. A second weaker DAP peak is observed at about 2.690 eV with its LO phonon replica at 2.658 eV.

Figure 47 shows PL spectra from SPVT grown Cl-doped ZnSe. The spectra for the Cl-doped and the N-doped samples are very similar to that from the as-grown samples shown in Fig.43, in that  $I_1^d$  and its LO phonon replicas are the prominent spectral features. The intensities of  $I_2$  and  $I_3$  are changed very little compared with those observed from the as-grown samples. This indicates that there is no significant change in the donor concentration resulting from the SPVT *in situ* Cl-doping process. The PL spectrum of SPVT grown N-doped ZnSe (not shown) does not exhibit the radiative recombination of shallow neutral acceptor bound exciton  $I_1$  emission signature, which is expected to appear if nitrogen is properly incorporated into ZnSe crystal as shallow impurity. The  $I_1^d$  emission line remains the strongest feature. Apparently nitrogen was not properly incorporated into ZnSe as shallow acceptor impurities by growing ZnSe in a nitrogen atmosphere. These results suggest that the current method of intentionally doping Cl and N during SPVT growth process cannot appropriately incorporate the dopant impurities into ZnSe properly as to introduce shallow levels in the near band-gap region.

The PL spectra of the SPVT grown Ga-doped ZnSe samples show very strong, broad emission peaking around 1.9 eV. The near band-gap bound exciton emission is much weaker than these emission bands. Typical spectra are shown in

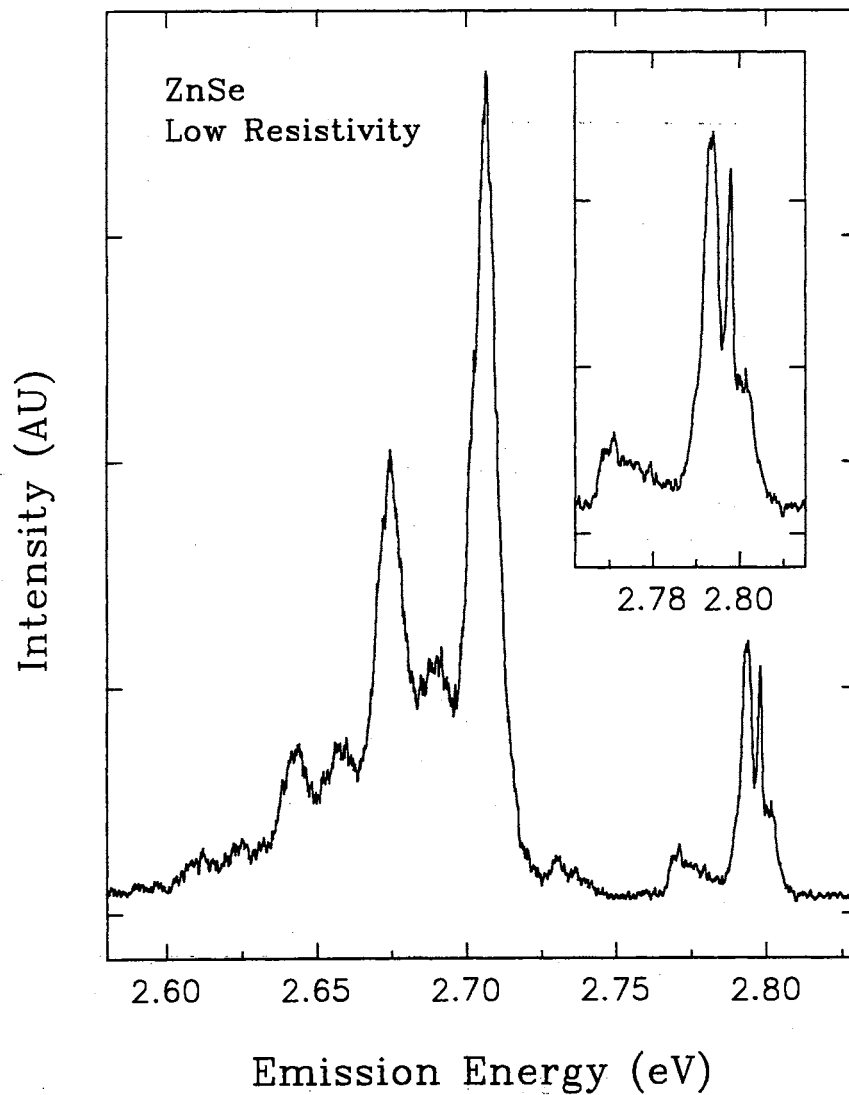


Figure 46. The PL spectrum from low resistivity ZnSe shows a strong DAP peak at 2.706 eV. One and 2LO phonon replicas are also observed at 2.675 and 2.644 eV. This DAP structure is not observed in the undoped SPVT ZnSe.

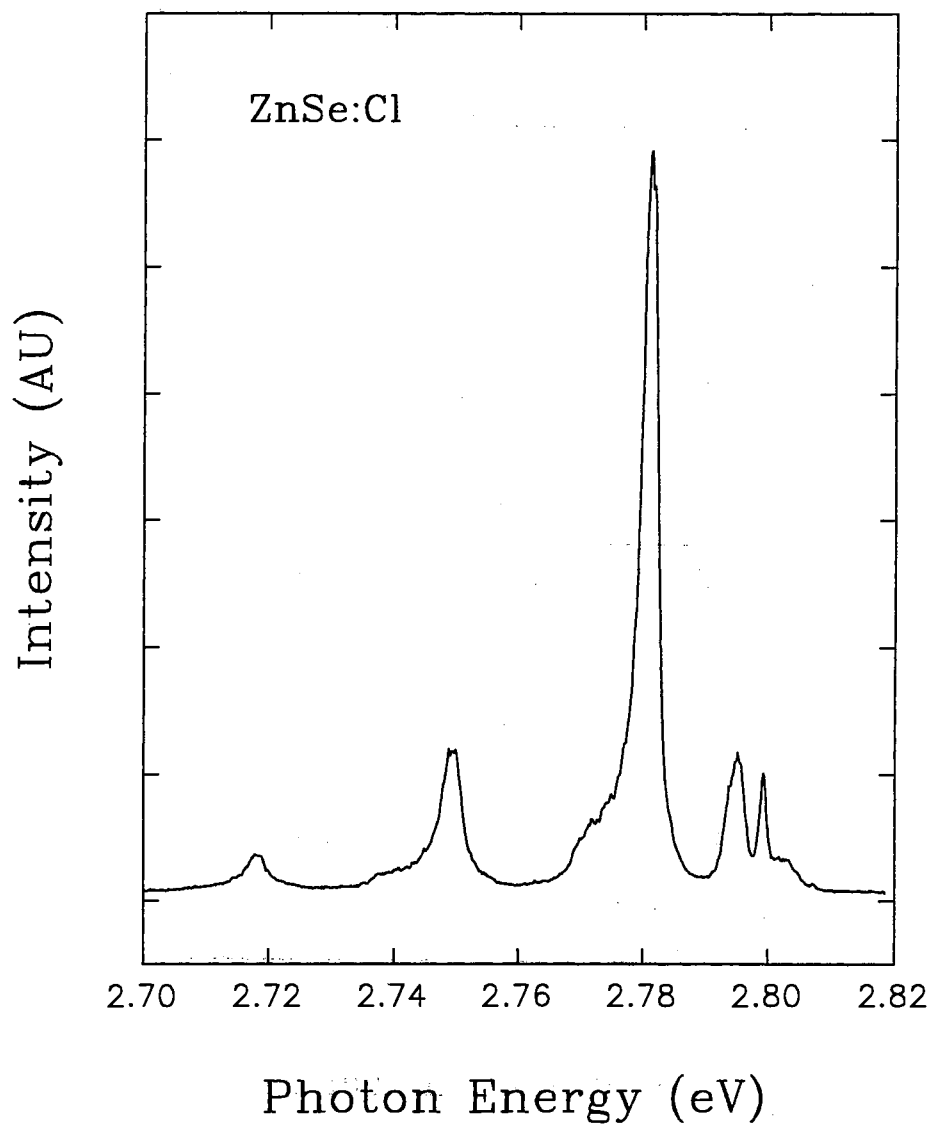


Figure 47. The PL spectrum from Cl-doped ZnSe samples. There is little discernable difference from that of the as-grown undoped ZnSe samples. The donor related  $I_2$  and  $I_3$  BE emission do not appear stonger than in undoped ZnSe, indicating very little change in the donor concentration.

Figs. 48 and 49, for 50 ppm and 100 ppm ZnSe:Ga sources, respectively. The insets on the two figures show the details of the near band-gap emission. The feature with the energy position of 2.794 in the 50 ppm sample is attributed to emission from the  $I_3$  bound exciton. In the 100 ppm sample,  $I_3$  is also observed, as is  $I_1$  and  $I_1^d$ . A broad peak is observed just below  $I_1^d$  at about 2.774 eV. This emission is tentatively assigned to deep acceptor bound excitons. The energy position of this peak closely matches that of  $I_v^o$  [113,137].

Photoluminescence of ZnSe:Li epilayers on GaAs. In addition to doped bulk ZnSe, ZnSe:Li/GaAs samples were also studied by photoluminescence. The PL spectra of an undoped ZnSe epilayer (2  $\mu\text{m}$ ) grown on GaAs is shown in Fig. 50. The peaks  $I_2$  (2.7984 eV) and  $I_3$  (2.7944 eV). Also observed is the peak at 2.770 eV (perhaps  $I_v^o$ ) and an unidentified peak at 2.7731 eV. Introduction of Li into a 1  $\mu\text{m}$  ZnSe epilayer causes the appearance of a peak (see Fig. 51) at 2.789 eV which is ascribed to an acceptor bound exciton ( $I_1$ ). Haynes' rule for acceptors yields an ionization energy of about 130 meV for this transition. Two strong peaks appear at 2.772 and 2.758 eV. The origins of these peaks are unclear, but the origin of the 2.772 eV peak may be similar to that of  $I_v^o$ . Additionally, there is an overall increase in impurity related emission at energies  $< 2.75$  eV. This sample is grown to have a Li concentration of approximately  $1 \times 10^{18} \text{ cm}^{-3}$ , with the net hole concentration measured to be  $1.6 \times 10^{16} \text{ cm}^{-3}$ . The PL from an even more highly doped ( $>10^{19} \text{ cm}^{-3}$ ) sample of thickness 600  $\text{\AA}$  is shown in Fig. 52. This sample shows much less impurity emission, with the largest peak at 2.791 eV, which is ascribed to  $I_1$ . This samples exhibits additional, much weaker peaks at 2.774 and 2.762 eV.

The effect of growth temperature on the spectra of 2  $\mu\text{m}$  thick  $\delta$ -doped ZnSe:Li/GaAs samples was studied. The PL from the 300° C sample is very weak and little excitonic structure is observed. The other samples show more well developed spectral features, with the sample grown at 370° C exhibiting weaker PL than the other samples grown above 300° C. All of these latter samples show

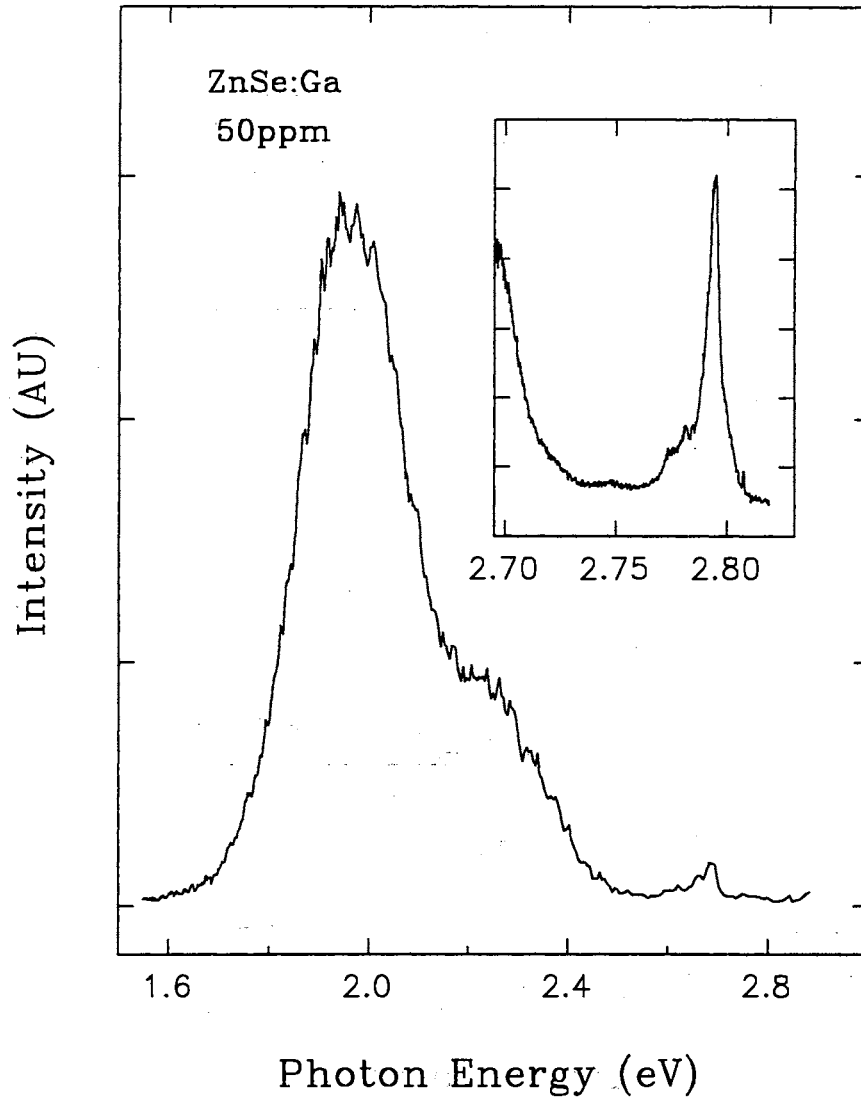


Figure 48. The PL spectra from bulk ZnSe:Ga, with 50 ppm Ga (starting material). The inset shows the near band gap emission. The spectra are dominated by the deep impurity emission  $< 2.5$  eV.

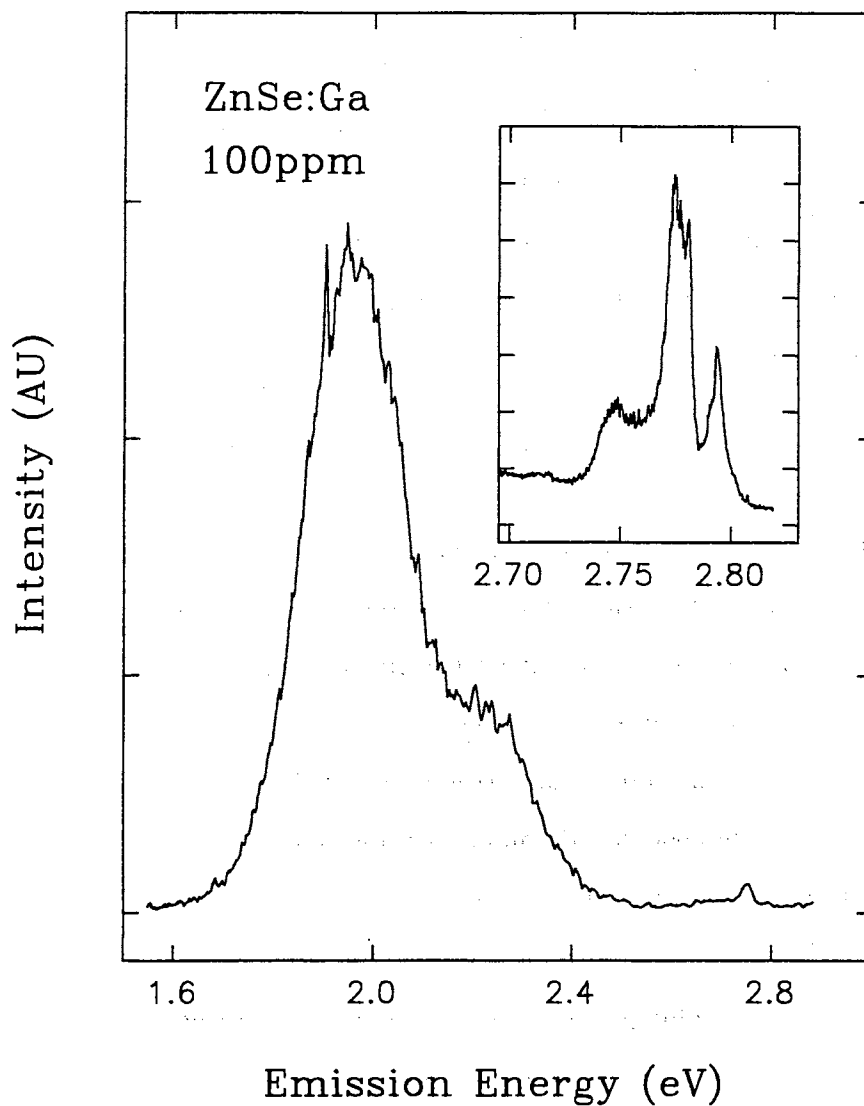


Figure 49. The PL spectra from bulk ZnSe:Ga, with 100ppm Ga (starting material). The inset again shows the near band gap emission. The spectra shows the same deep impurity emission as the 50ppm sample, with additional features seen in the near-band gap emission. The peaks below  $I_1^d$  are ascribed to deep acceptor bound excitons.

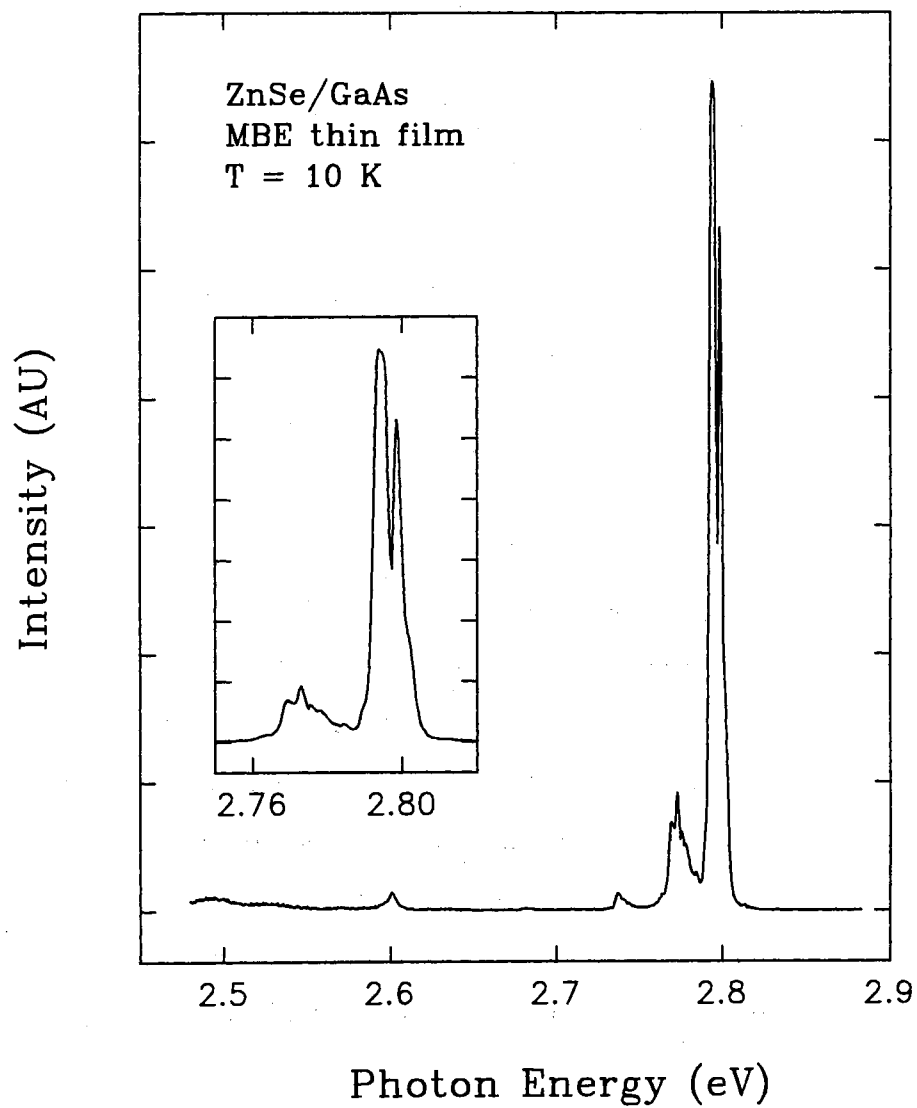


Figure 50. The PL spectra from undoped ZnSe epilayers grown on GaAs. The  $I_2$  (2.7984 eV) and  $I_3$  (2.7944 eV) peaks dominate the spectra.

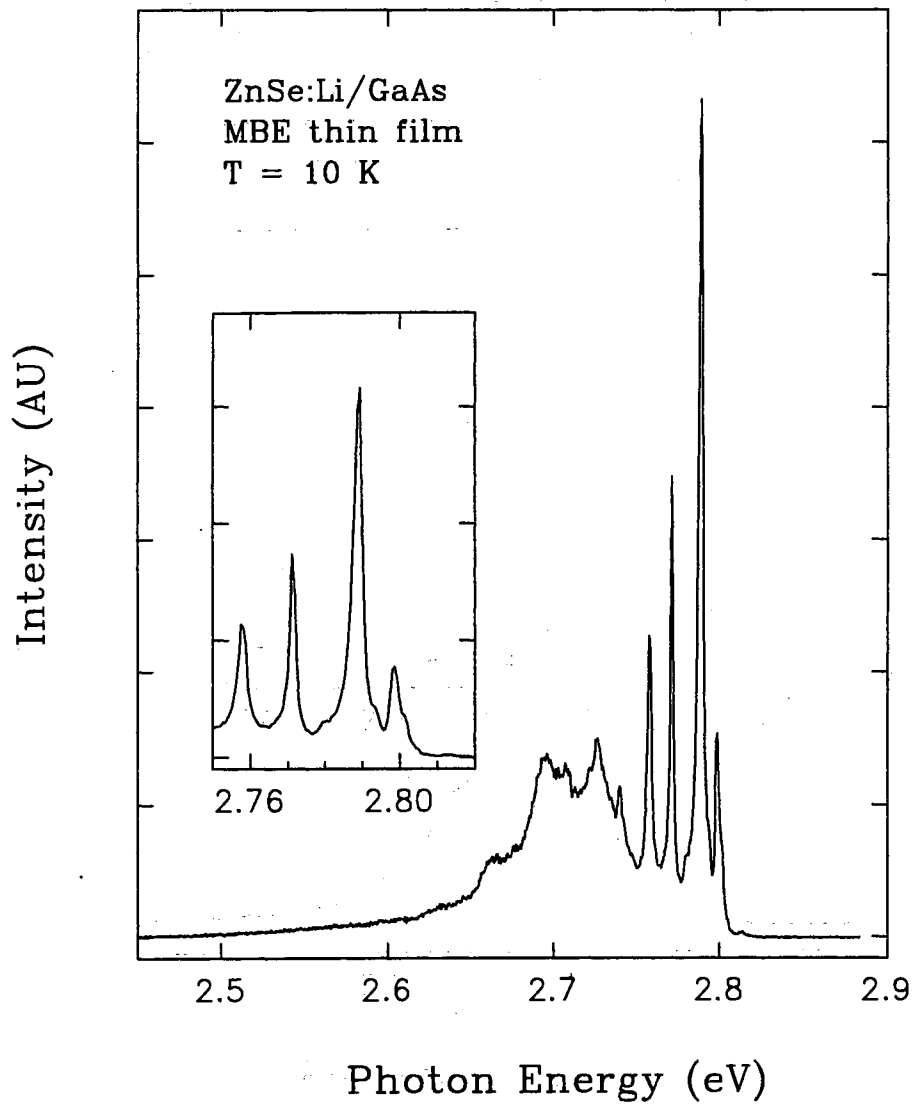


Figure 51. The PL spectra from lithium doped ZnSe epilayers grown on GaAs, showing the acceptor bound exciton ( $I_1$ ) at 2.789 eV. Note the appearance of peaks at 2.772 and 2.758 eV. The peak at 2.772 eV may be due to  $I_0$ .



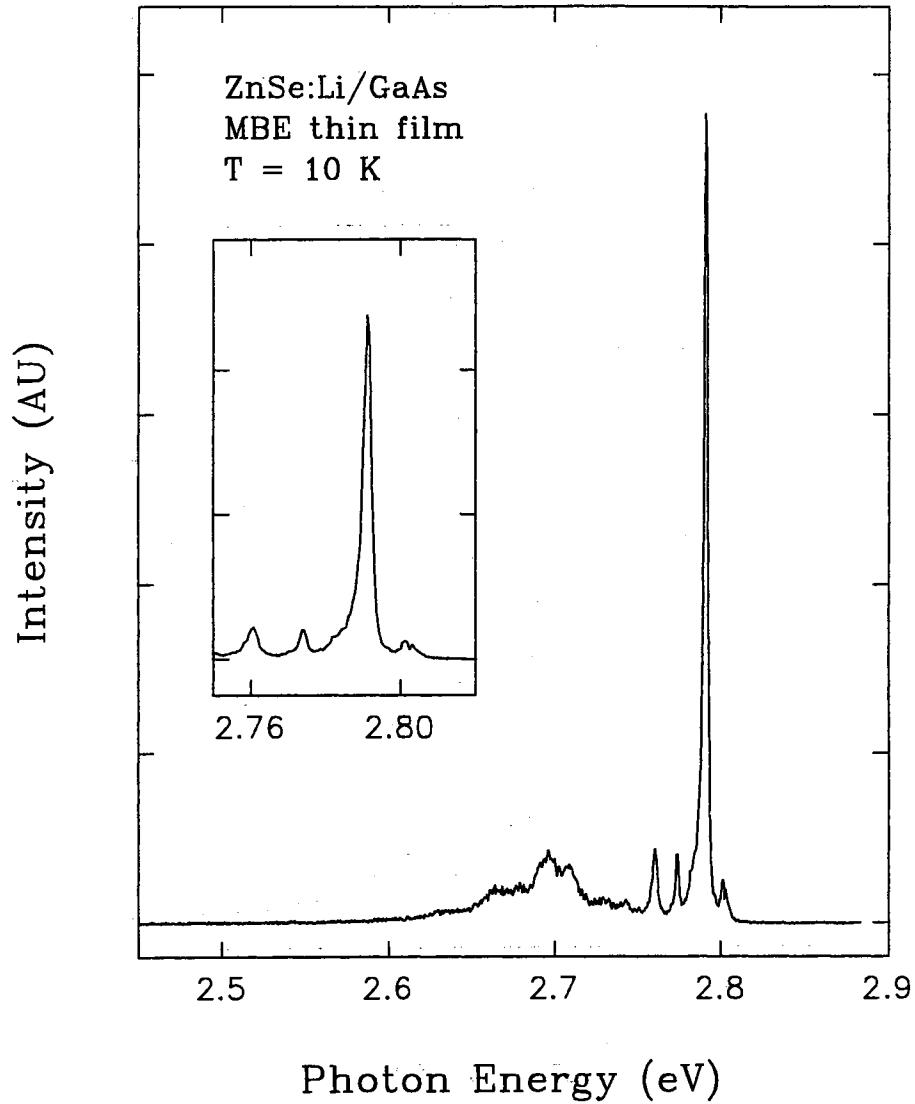


Figure 52. The PL spectra from a more highly Li doped ZnSe grown on GaAs. The  $I_1$  peak is seen at 2.791 eV and less impurity or defect emission is observed than in the previous sample.

$I_1$  peaks in the range of 2.786 – 2.788 eV. They also exhibit peaks in the region 2.797 – 2.799 eV and peaks which are identified with  $I_0^c$  at about 2.770 eV.

The results for all of the Li doped samples are summarized in Table V.

It is interesting to note that the studied samples do not show clear evidence of splitting of the LH and HH states due to the compressive strain due to the thermal mismatch of the expansion coefficient. The double peaked free exciton emission is seen in bulk ZnSe as discussed above, and can be ascribed to the upper and lower polariton branches. Only one of the samples shows any evidence of a double peak which may be interpreted as splitting of the  $I_1$  emission. However, this is not very clear as can be seen in Fig. 53. The splitting of  $I_1$  here is quite small ( $\sim 2.2$  meV) and could also be due to slightly differing acceptor site potentials.

### Conclusions

Large size strain-free ZnSe single crystals have been successfully grown by the newly developed seeded physical vapor phase transport technique. Low-temperature photoluminescence measurements were used to examine the quality of undoped as-grown and post-growth-treated ZnSe samples and characterize the intentionally doped samples by studying the near-band-gap bound exciton emission lines and donor-acceptor-pair emission band. It has been found that Zn-extraction treatment can drastically reduce the density of deep acceptors in SPVT grown ZnSe crystal resulting in suppression of the  $I_1^d$  emission. The PL result from Cl- and N-doped ZnSe samples indicates that the dopants were not properly incorporated into ZnSe crystals as shallow impurities by *in situ* doping during SPVT growth process. The ZnSe:Ga samples were apparently overdoped using the current growth method, causing the formation of deep centers as well as poor crystallinity. However, lower levels of doping in the starting materials may allow controllable doping concentrations.

The ZnSe:Li samples grown on GaAs do show p-type conductivity, and exhibit clear evidence of  $I_1$  emission. The introduction of Li at concentrations which are required to make p-type material apparently causes the generation of deep

TABLE V.

Epilayer thickness	Growth T ( $^{\circ}C$ )	$E_i^A$ (meV)	$N_A - N_D$
$1\mu\text{m}$	320	128	$1.6 \times 10^{16}$
600 Å	320	110	
$2\mu\text{m}$	350	140,160	$3.7 \times 10^{17}$
$2\mu\text{m}$	300	-	
$2\mu\text{m}$	370	160	

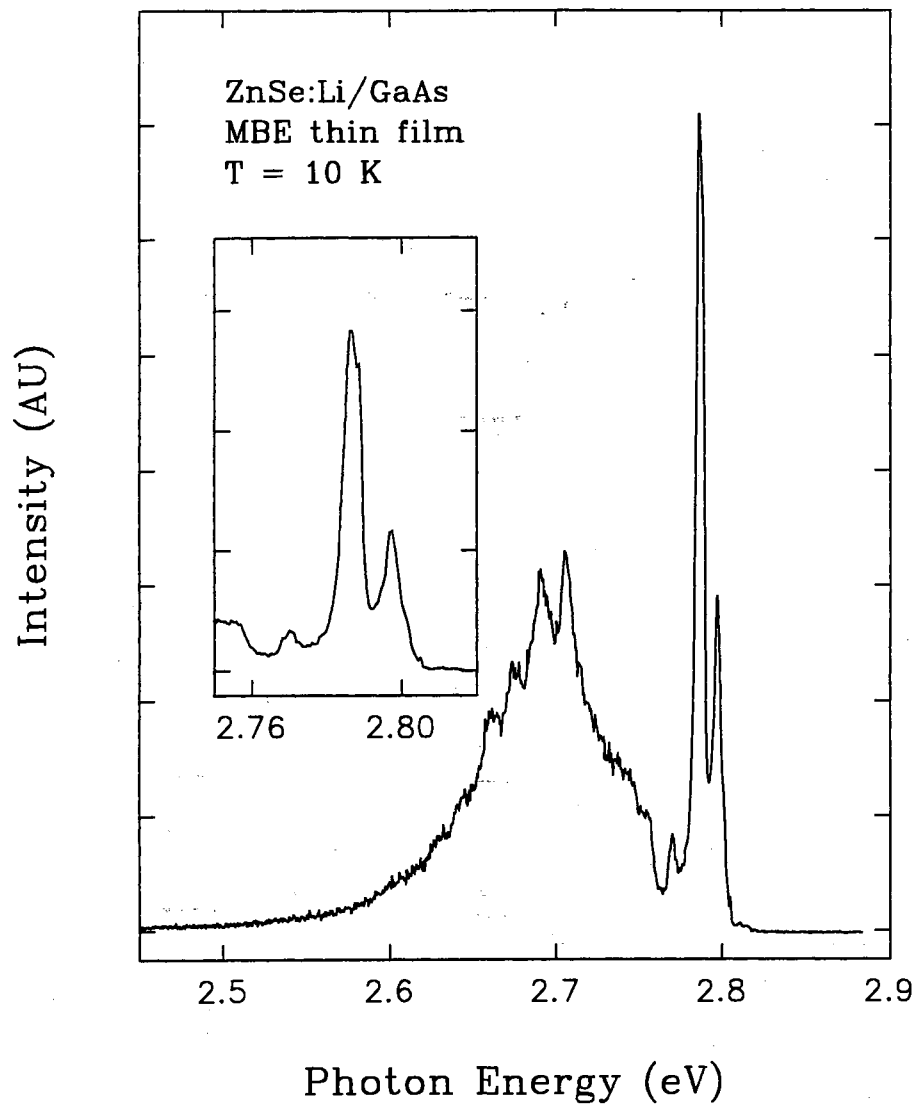


Figure 53. The PL spectrum from lithium doped ZnSe epilayers grown on GaAs. The  $I_1$  emission at 2.86-2.89 eV appears to be a doublet for this sample. This could be due to strain effects or to slightly differing acceptor site potentials.

defect states. These states are observed in the spectra in the region of 2.7 eV in the Li doped samples and are not observed in the undoped ZnSe epilayers.

Haynes' rule for donor states fits the hydrogenic model quite well. The acceptor ionization energies determined by this method, however, are larger than predicted by the hydrogenic model.

## CHAPTER V

### Conclusions

The results presented bear out the comments made in Chapter I about the complimentary nature of linear and nonlinear spectroscopic techniques. As described in Chapter II, the 1HH-1e 1s exciton binding energy could only be determined by linear absorption (reflectance or PLE) and a technique sensitive to the two-photon resonances used in conjunction.

The results for the NDFWM and TP-PLE spectra presented imply that for some systems, the TP-PLE technique can be sensitive and selective. TP-PLE is selective in the sense that the contributions of the TP absorption due to states which are not energetically connected can be separated. This is seen in the TP-PLE data for D58, where the different  $2p$  states are observed for the different wells. Further, the NDFWM spectra is sensitive to  $|\chi^{(3)}|$ , whereas the TP-PLE technique, probing the TP absorption, is sensitive only to  $Im\chi^{(3)}$ . This may account for the lack of the  $2p$  resonance in the NDFWM spectra. Since the NDFWM technique cannot differentiate between the contributions of the two wells, the excitonic features will be obscured. Additionally, the excitonic peaks will be broadened due to the combination of the dispersive and absorptive part of  $\chi^{(3)}$ .

The binding energy of the  $2p$  excitons have been discovered to vary considerably from the bulk value. The bulk unperturbed  $2p$  excitons have binding energies of about 5 – 6 meV. [74] The binding energies of the 1HH-1e  $2p$  excitons in ZnCdSe/ZnSe QW's (for samples D59 and D63A) are twice this value or more. This is in difference to that observed and predicted theoretically for GaAs/AlGaAs QW's, where the  $2p$  binding energies are nearly identical to the bulk values. [39,54]

The 1HH-1e 1s exciton binding energy for the 50 Å ZnCdSe/ZnSe QW's has been determined to exceed the LO phonon energy of about 31 meV. This should

imply that the LO phonon coupling constant is decreased in these samples with respect to bulk ZnSe. However, using coherent transient degenerate four-wave mixing (CT-DFWM) it has been determined [50,139] that the  $\Gamma_{LO}$  for the epilayer and QW (D63A) samples are nearly identical (recall  $\Gamma_{LO} \simeq 80$  meV for epilayer ZnSe). The increase of the binding energy beyond the LO phonon energy does not eliminate all the possible states available for scattering. It is also possible that the  $1s$  state may be scattered into other higher lying excitonic states instead of being disassociated. These effects are illustrated in Fig. 54, where the  $1s$  exciton may be scattered into a  $2s$  (intersubband scattering) or increasing its kinetic energy without changing subbands (intrasubband scattering). The exciton may also be scattered from the HH band into the LH band. For GaAs/AlGaAs QW's, it has been theoretically determined that the dominant excitonic scattering mechanism is  $1HH-1e$   $1s$  exciton scattered into the  $1LH-1e$   $1s$  exciton. [140] This has strong implications for the D63A, with the  $1LH-1e$  and  $1HH-1e$   $1s$  excitons separated by 28 meV. For the higher  $x$  value samples, D58 and D59, the energy difference between these two excitons is larger than  $1LO$  phonon energy. Coherent transient DFWM of these higher Cd concentration samples should establish the importance of this scattering mechanism.

The variation of  $\Gamma_{LO}$  could be measured using CT-DFWM for the different Cd concentrations of the samples presented here. As mentioned above, however, separating out the available scattering mechanisms may not be readily accomplished. Another possible difficulty with this procedure is the variation in coupling due not to the binding energy difference but because of the alloy nature of the samples. The different alloys would have slightly different phonon energies, and possibly, different coupling due to variations in the alloy disorder. It may be feasible to circumvent this last difficulty by use of a single sample and increasing the binding energy by application of hydrostatic pressure. [141] This would eliminate the difficulties due to the variation of  $x$ , and requires the use of both TP-PLE (or similar technique) to measure the binding energy and CT-DFWM to measure  $\Gamma_{LO}$  as a function as a function of pressure. Measurement of the binding energy as a

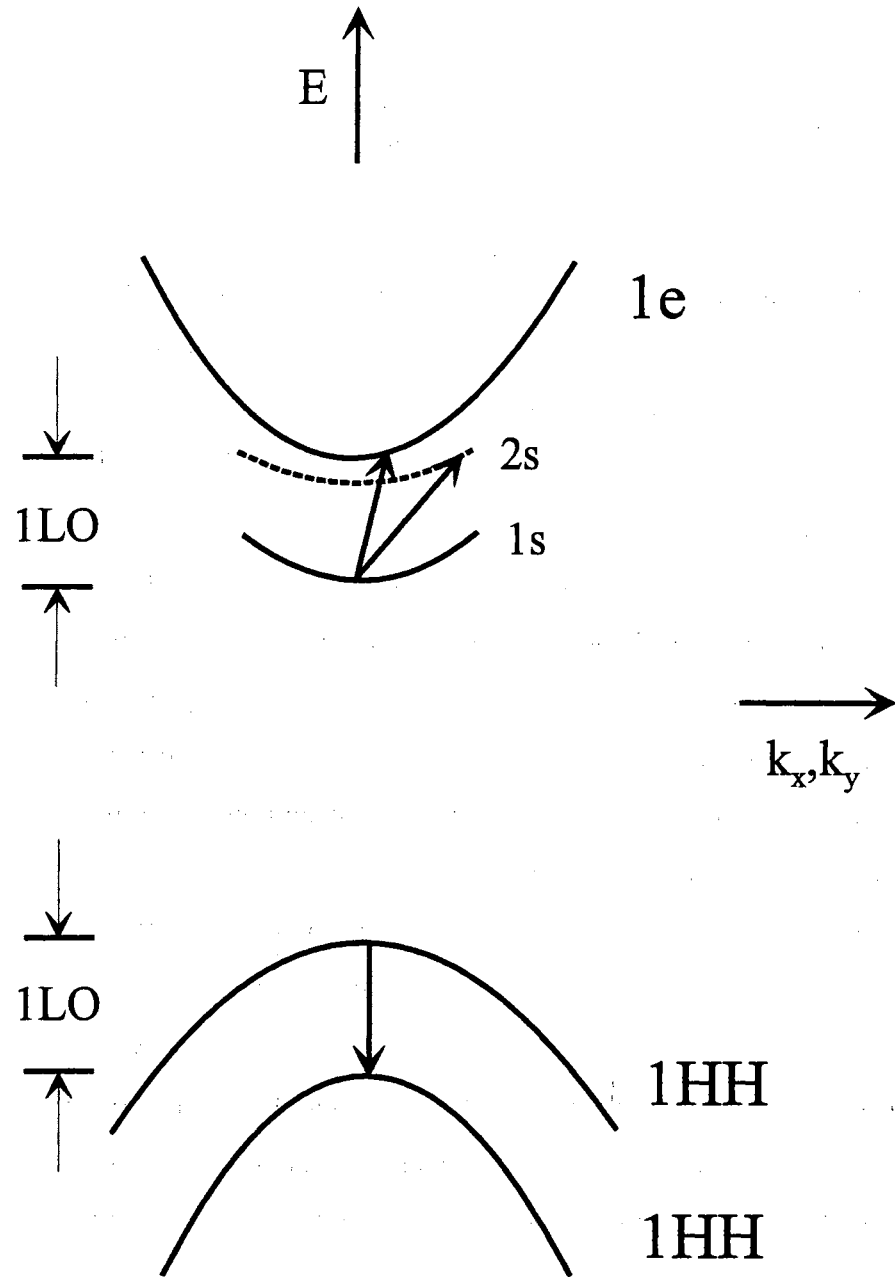


Figure 54. Possible phonon scattering mechanisms in a QW. The absorption of an LO phonon may disassociate the exciton, scatter it into a 2s state or scatter the hole into a higher lying band.



function of pressure for these systems is of interest in its self. The effect of pressure on the binding energy of the  $1s$  excitons has not been treated experimentally nor theoretically for these systems. [142]

Despite the large  $\Gamma_{LO}$  measured for D63A, room temperature (RT) excitons have been observed for this sample structure. Fig. 55 shows the PL and absorption spectra at RT for a ZnCdSe/ZnSe sample grown on a ZnSe substrate. The large Stokes' shift in this sample suggests that the RT PL emission is due to impurities in the wells. Room temperature excitons have also been observed in similar samples grown on GaAs. [75]

The polarization selection rules could be used to study the two-photon allowed electronic states in more detail than given above. The TP-PLE study described in Chapter II was limited to the polarization  $\vec{E} \perp \hat{z}$  for convenience. However, as discussed previously,  $\vec{E} \parallel \hat{z}$  allows the study of other transitions, specifically the  $\Delta n \neq 0$  LH transitions. The TP transitions thus probed are 2LH-1e, 1LH-2e, etc., and the associated  $s$  excitonic states. [54,143,55-57] This polarization can be achieved in a couple of ways, as shown in Fig. 56. The light can be directly coupled into the well as in Fig. 56a. [39,144,42] Another possibility for the ZnSe substrate samples is shown in Fig. 56b., which has been used in linear spectroscopy. [65] In this case, the ZnSe is essentially two-photon transparent ( $\beta \sim 0$ ) in the QW energy region of interest, allowing this configuration. The configuration shown in Fig. 56a increases the interaction length, but restricts the study to waveguide structures. [39,144,42]

Application of an external electric field or an internal electric field along the  $\hat{z}$  direction should allow the  $1s$  states to be observed with the polarization  $\vec{E} \perp \hat{z}$ . The electric field destroys the inversion symmetry with respect to the center of the well, eliminating parity as a good quantum number. This may be what occurred for the 2ML CdSe/ZnSe QW shown in Chapter II. The SP-PLE in Fig. 16 shows oscillations which may be due to the Franz-Keldysh effect. Single-photon PLE has been performed on 1, 2, 3, and 4 ML CdSe/ZnSe samples, and all show this oscillatory behavior. [67,70] This electric field would allow the 1HH-1e  $1s$  exciton

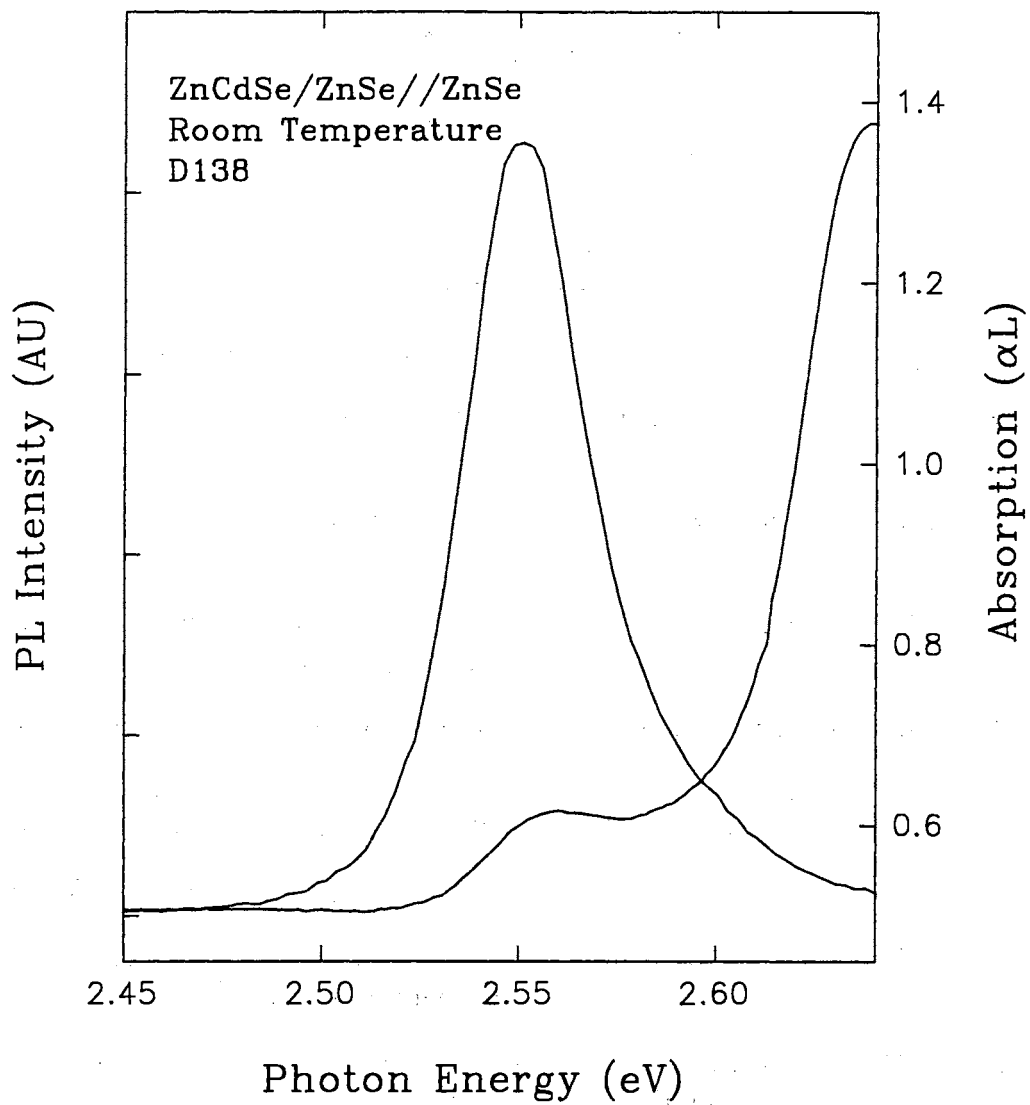


Figure 55. Room temperature absorption and luminescence for a ZnCdSe/ZnSe sample. A 6 period 50Å ZnCdSe/ZnSe QW grown on ZnSe exhibits both RT photoluminescence and RT excitonic absorption.

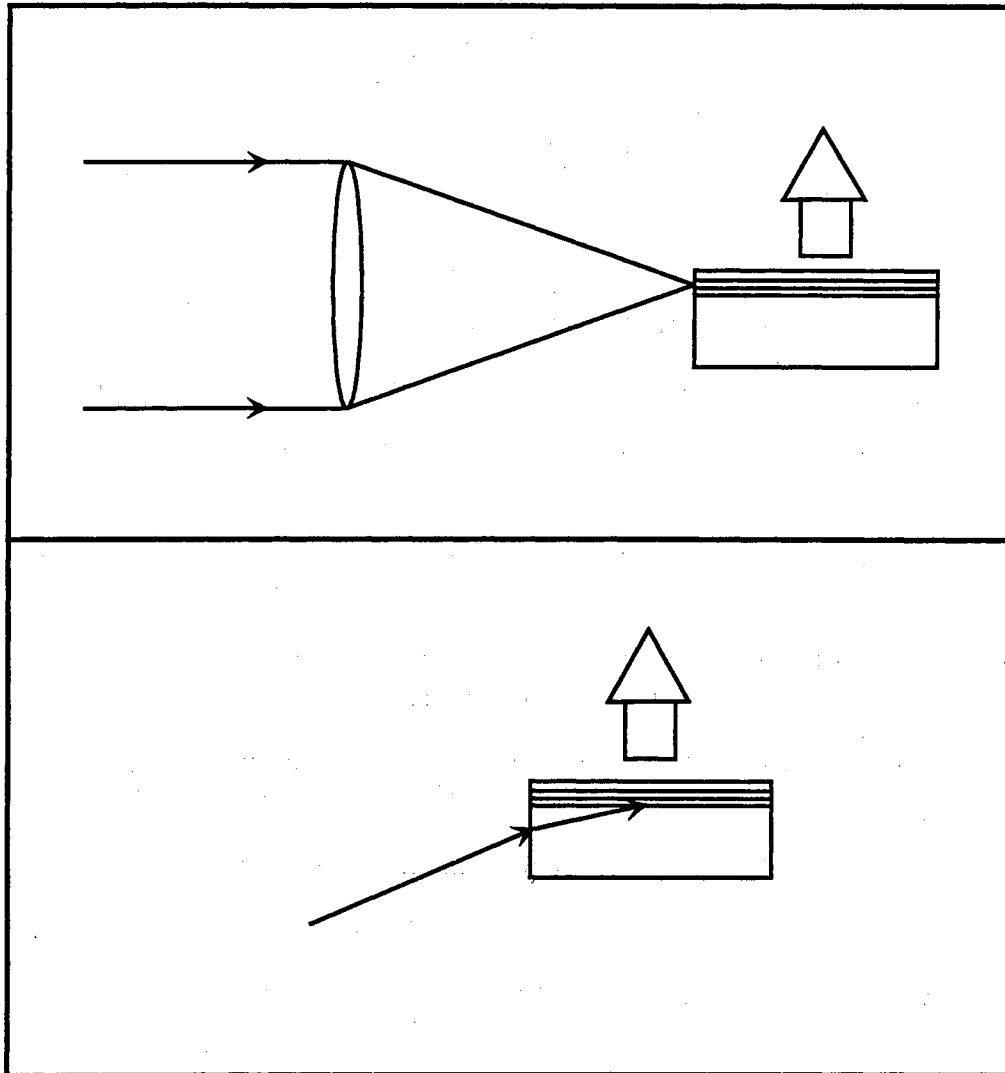


Figure 56. Two different techniques to observe the polarization selection rules. In a), the light is directly coupled into the wells. This technique utilizes a sample with a waveguide structure. For the configuration shown in b), a substrate with minimal TPA coefficient  $\beta$  in the energy range of interest is required.

to become TP allowed. Note that the TP-PLE data for this sample 24 shows a resonance with this transition, while the  $2p$  exciton is not observed. Possible mechanisms for a built-in electric field include unintentional doping and stress effects. Since a zinc blende crystal has only off-diagonal elements of the stress tensor (with  $\hat{z}$  along the (100) direction), the stress must have a shear component in order for the net polarization in the  $\hat{z}$  to be nonzero. However, a QW grown on a (100) substrate will not have any shear components. [145] Another possible source of shear stress may be screw or edge dislocations. [145] The difficulty with this mechanism is that all of the CdSe/ZnSe samples exhibit nearly identical fields ( $10^5$  V/cm [70]), while the dislocation density appears to be much greater in the 4ML sample. [67]

An examination of the TP-PLE spectra shows that all of the samples exhibit emission in the  $1\text{HH-}1e\ 1s$  exciton region. For the ZnCdSe/ZnSe QW's, however, this is not due to absorption but due to resonant second harmonic generation (SHG). This can be seen by the fact that the linewidth of the emission is that of the detection system and not the linewidth of the excitonic peak. The emission is narrower than the exciton in all of these samples. One group has suggested that their observation of a  $1\text{HH-}1e\ 1s$  exciton in TPA (GaAs-based QW's) is due to resonant SHG and subsequent absorption of the SHG photon. This did not occur for the ZnCdSe/ZnSe QW samples. Note that the symmetry of a zinc blende material ( $\bar{4}3m$ ) does not allow SHG along the (100) axis. The creation of a QW reduces the symmetry to  $\bar{4}2m$ , but this does not cause the SHG to become allowed. Resonant SHG of ZnSe epilayers grown on (100) GaAs has been reported. [146] In this case, the strong SHG resonance is with the  $2p$  exciton, while the  $1s$  exciton contributed only weakly. The authors attribute the observation of dipole forbidden SHG to the electric quadrupole term. [146]

The stimulated emission study in CdTe yielded gain values of up to  $750\ \text{cm}^{-1}$ . While this gain is low compared to that reported for GaAs ( $\sim 2000\ \text{cm}^{-1}$  [97]) and other III-V compounds, it is in the same range or higher than other II-VI compounds. For example, CdS exhibits gain values of about  $200\ \text{cm}^{-1}$ , and CdSe

of about  $1000 \text{ cm}^{-1}$ . [97] The simplistic four-level model qualitatively predicts the correct behavior for the SE in the limits of low and excitation. Further study is needed in the behavior of the EHP in CdTe. One such study has been done, by Schweizer and Zielinski, but they did not observe the strong, broad peaks observed in this study. [102] This is probably due to the fact that they were working with bulk CdTe. The epilayers of CdTe grown on CdZnTe enhances the EHP formation due to the confinement of the carriers within the  $2.4 \mu\text{m}$  film. A pump-probe experiment using the reflection geometry could study the temporal behavior of this spectral feature.

The doping of bulk ZnSe is, in many ways, an open question. The preparation of p-type ZnSe epilayers has been accomplished, as has n-doping of bulk material. However, the basic questions of compensation mechanisms have only been sidestepped. Substantial n- and p-type conductivity requires over-doping due to compensation. [147] The lifetime of Li-doped ZnSe has also been of concern. A spatially small ion such as Li can easily occupy an interstitial site, where it will become a donor instead of an acceptor. [148] Currently, nitrogen doping of ZnSe has been accepted as a promising technique. [148][149] Nitrogen, however, also introduces compensating energy levels and deep defects. [149]

## BIBLIOGRAPHY

1. H. Venghaus, *Phys. Rev. B* **19**, 3071 (1979).
2. J. Hays, Unpublished results.
3. M.L. Cohen and J.R. Chelikowsky, *Electronic Structure and Optical Properties of Semiconductors* (Springer-Verlag, Berlin, 1989).
4. Evan O. Kane, *J. Phys. Chem. Solids* **1**, 249 (1957).
5. E.O. Kane, *Semiconductors and Semimetals*, R.K. Willardson and A.C. Beer, eds., (Academic, New York, 1966), Vol. 1, ch. 3.
6. Gerard Bastard, *Wave Mechanics Applied to Semiconductor Heterostructures* (John Wiley, New York, 1988).
7. Franco Bassani, *Semiconductors and Semimetals* (Academic Press, New York, 1966), eds. R.K. Willardson and Albert C. Beer.
8. Walter A. Harrison, *Electronic Structure and the Properties of Solids* (Dover, New York, 1989).
9. Carl A. Baumgardner and Truman O. Woodruff, *Phys. Rev.* **173**, 746 (1968).
10. R.J. Elliot, *Phys. Rev.* **108**, 1384 (1957).
11. P.N. Butcher and D. Cotter, *The Elements of Nonlinear Optics* (Cambridge University Press, Cambridge, 1990).
12. B. Segall, D.T.F. Marple, in *Physics and Chemistry of II-VI Compounds*, edited by M. Aven and J.S. Prener (North-Holland Publishing, Amsterdam, 1967), p. 321-326.
13. Claude Cohen-Tannoudji, Bernard Diu and Franck Laloë, *Quantum Mechanics* (Springer-Verlag, Berlin, 1989), Vol. 1, ch. VII.
14. B.K. Ridley, *Quantum Processes in Semiconductors* (Clarendon Press, Oxford, 1988), Second ed., pp. 59-61, 197.
15. John O. Dimmock, in *Semiconductors and Semimetals*, edited by R.K. Willardson and Albert C. Beer (Academic, New York, 1967), Vol. 3, p. 275.

16. G. Bastard, *Phys. Rev. B* **25**, 7584 (1982).
17. Claude Cohen-Tannoudji, Bernard Diu and Franck Laloë, *Quantum Mechanics* (Springer-Verlag, Berlin, 1989), Vol. 1, ch. VII, pp. 74-78.
18. Rolf G. Winter, *Quantum Physics* (Faculty Publishing, Davis, CA, 1991), Second ed., pp. 60-76.
19. Claude Weisbuch and Borge Vinter, *Quantum Semiconductor Structures* (Academic Press, New York, 1991).
20. Masaki Shinada and Satoru Sugano, *J. Phys. Soc. Jpn.* **21**, 1936 (1966).
21. H.I. Ralph, *Sol. Stat. Comm.* **3**, 303 (1965).
22. B.P. Zakharchenya, D.N. Mirlin, V.I. Perel', and I.I. Reshina, *Sov. Phys. Usp.* **25**, 143 (1982).
23. E.U. Condon and G.H. Shortley, *The Theory of Atomic Spectra* (Cambridge University Press, Cambridge, 1957), p. 149.
24. Ernst O. Göbel and Klaus Ploog, *Prog. Quantum Electr.* **14**, 289 (1991).
25. R. Dingle, W. Wiegmann, and C.H. Henry, *Phys. Rev. Lett.* **33**, 827 (1974).
26. R. People and S.A. Jackson, *Semiconductors and semimetals* (Academic Press, Boston, 1990), Vol. 32., ch. 4.
27. Robert W. Boyd, *Nonlinear Optics* (Academic Press, Boston, 1992), ch. 3.
28. N. Bloembergen, H. Lotem, and R.T. Lynch, *Indian J. Pure Appl. Phys.* **16**, 151 (1978).
29. Y.R. Shen, *The Principles of Nonlinear Optics* (John Wiley and Sons, New York, 1984), ch. 2.
30. Yehiam Prior, *IEEE J. Quantum Electron.* **QE-20**, 37 (1984).
31. Tatsuo Yajima and Yoichi Taira, *J. Phys. Soc. Jpn.* **47**, 1620 (1979).
32. Claude Cohen-Tannoudji, Bernard Diu and Franck Laloë, *Quantum Mechanics* (Springer-Verlag, Berlin, 1989), Vol. 1, ch. VII., p. 1310.
33. D.L. Mills, *Nonlinear Optics*, (Springer-Verlag, Berlin, 1991).
34. Amnon Yariv, *Quantum Electronics* (John Wiley and sons, New York, 1989), 3rd. ed., ch. 18.
35. P.N. Butcher and D. Cotter, *The Elements of Nonlinear Optics* (Cambridge University Press, Cambridge, 1990), ch. 5.

36. S. Schmitt-Rink, D.S. Chemla, and D.A.B. Miller, *Adv. Phys.* **38**, 89 (1989).
37. D.S. Chemla, D.A.B. Miller, and S. Schmitt-Rink, *Optical Nonlinearities and Instabilities in Semiconductors* (Springer-Verlag, Berlin, 1989), ed. Hartmut Haug.
38. P.N. Butcher and D. Cotter, *The Elements of Nonlinear Optics* (Cambridge University Press, Cambridge, 1990), pp. 270-274.
39. K. Tai, A. Mysyrowicz, R.J. Fischer, R.E. Slusher, and A.Y. Cho, *Phys. Rev. Lett.* **62**, 1784 (1989).
40. I.M. Catalano, A. Cingolani, R. Cingolani, and M. Lepore, *Phys. Rev. B* **40**, 1312 (1989).
41. M. Nithisoontorn, K. Unterrainer, S. Michaelis, N. Sawaki, E. Gornik, and H. Kano, *Phys. Rev. Lett.* **62**, 3078 (1989).
42. H.Q. Le, H.K. Choi, and C.A. Wang, *Appl. Phys. Lett.* **57**, 212 (1990).
43. Il Cha, Shigeaki Ohke, Tokuo Umeda, and Yoshio Cho, Sixth record of alloy semiconductor physics and electronics symposium, p. 499.
44. R. Tommasi, M. Lepore, M.C. Netti, I.M. Catalano, and I. Suemune, *Phys. Rev. B* **49**, 14367 (1994).
45. M.A. Haase, J. Qiu, J.M. DePuydt, and H. Cheng, *Appl. Phys. Lett.* **59**, 1272 (1991).
46. H. Jeon, J. Ding, A.V. Nurmikko, H. Luo, N. Samarth, J. Furdyna, *Appl. Phys. Lett.* **59**, 1293 (1991).
47. H. Jeon, J. Ding, A.V. Nurmikko, W. Xie, M. Kobayashi, and R.L. Gunshor, *Appl. Phys. Lett.* **60**, 892 (1992).
48. Charles Kittel, *Introduction to Solid State Physics*, (John Wiley, New York, 1986), p. 298.
49. S. Rudin, T.L. Reinecke, and B. Segall, *Phys. Rev. B* **42**, 11218 (1990).
50. A.J. Fischer, D.S. Kim, J. Hays, W. Shan, J.J. Song, D.B. Eason, J. Ren, J.F. Schetzina H. Luo, J.K. Furdyna, Z.Q. Zhu, T. Yao, J.F. Klem, and W. Schäfer, *Phys. Rev. Lett.* **73**, 2368 (1994).
51. Dai-Sik Kim, Jagdeep Shah, J.E. Cunningham, T.C. Damen, Wilfried Schäfer, Michael Hartmann, and Stefan Scmitt-Rink, *Phys. Rev. Lett.* **68**, 1006 (1992).
52. N.T. Pelekanos, J. Ding, M. Hagerott, A.V. Nurmikko, H. Luo, N. Samarth, and J.K. Furdyna, *Phys. Rev. B* **45**, 6037 (1992).



53. G.D. Mahan, Phys. Rev. Lett. **20**, 332 (1968).
54. Akira Shimizu, Phys. Rev. B **40**, 1403 (1989).
55. Alfredo Pasquarello and Antonio Quattropani, Phys. Rev. B **38**, 6206 (1988).
56. Alfredo Pasquarello and Antonio Quattropani, Phys. Rev. B **42**, 9073 (1990).
57. Alfredo Pasquarello and Antonio Quattropani, Superlatt. Microstruct. **9**, 157 (1991).
58. M. Göppert-Mayer, Ann. Physik **9**, 273 (1931).
59. W. Kaiser and C.G.B. Garrett, Phys. Rev. Lett. **7**, 229 (1961).
60. R. Loudon, Proc. Phys. Soc. **80**, 952 (1962).
61. Rubin Braunstein, Phys. Rev. **125**, 475 (1962).
62. C.C. Lee and H.Y. Fan, Phys. Rev. B **9**, 3502 (1974).
63. F. Bassani and G. Pastori Parravicini, *Electronic States and Optical Transitions in Solids* (Pergamon Press, Oxford, 1975), ed. R.A. Ballinger.
64. J. Burris and T.J. McIlrath, J. Opt. Soc. Am. B **2**, 1313 (1985).
65. Gerard Bastard, *Wave Mechanics Applied to Semiconductor Heterostructures* (John Wiley, New York, 1988), p. 249.
66. R.E. Nahory, M.J.S.P. Brasil and M.C. Tamargo, *Semiconductor Interfaces and Microstructures* (World Scientific, Singapore, 1992), pp. 238-251., ed. Feng J.-Z.
67. W. Shan, S.J. Hwang, J.M. Hays, J.J. Song, Z.Q. Zhu, and T. Yao, J. Appl. Phys. **74**, 5699 (1993).
68. L. Schultheis, A. Honold, J. Kuhl, K. Köhler and C.W. Tu, Phys. Rev. B **34**, 9027 (1986).
69. J.M. Hays, X.H. Yang, S.J. Hwang, W. Shan, J.J. Song, J. Ren, Z. Yu, and J.F. Schetzina, *Bulletin of the American Physical Society* (American Physical Society, College Park, 1994).
70. S.J. Hwang and J. Hays, Unpublished data.
71. S.J. Hwang, Unpublished calculations.
72. G. Bastard, Phys. Rev. B **24**, 5693 (1981).
73. Barbra A. Wilson, IEEE J. Quantum Electron. **24**, 1763 (1988).
74. M. Sondergeld and R.G. Stafford, Phys. Rev. Lett. **35**, 1529 (1975).

75. J. Ding, N. Pelekanos, A.V. Nurmikko, H. Luo, N. Samarth and J.K. Furdyna, *Appl. Phys. Lett.* **57**, 2885 (1990).
76. Claude Weisbuch and Borge Vinter, *Quantum Semiconductor Structures* (Academic Press, New York, 1991), p. 63.
77. Henry Mathieu, Pierre Lefebvre, and Philippe Christol, *Phys. Rev. B* **46**, 4092 (1992).
78. *Landolt-Borstein*, ed. O. Madelung (Springer-Verlag, Berlin, 1982), New Series, Vol. 17.
79. Marc D. Levenson and Satoru S. Kano, *Introduction to Nonlinear Laser Spectroscopy*, (Academic, New York, 1988), Revised ed.
80. M.D. Levenson and N. Bloembergen, *Phys. Rev. B* **10**, 4447 (1974).
81. Robert Adair, L.L. Chase and Stephen A. Payne, *Phys. Rev. B* **39**, 3337 (1989).
82. H.J. Eichler, P. Günter, and D.W. Pohl, *Laser-Induced Dynamic Gratings* (Springer-Verlag, Berlin, 1986).
83. P.D. Maker and R.W. Terhune, *Phys. Rev.* **137**, A801 (1965).
84. R.F. Begley, A.B. Harvey, R.L. Byer, *Appl. Phys. Lett.* **25**, 387 (1974).
85. Marc D. Levenson, *IEEE J. Quantum Electron.* **QE-10**, 110 (1974).
86. Eric W. Van Stryland, H. Vanherzeele, M.A. Woodall, M.J. Soileau, Arthur L. Smirl, Shekhar Guha, and Thomas F. Boggess, *Opt. Eng.* **24**, 613 (1985).
87. K.R. Zanio, in *Semiconductors and Semimetals*, edited by R.K. Willardson and A.C. Beer (Academic, New York, 1973), Vol. 13.
88. I. Melngailis and A.J. Strauss, *Appl. Phys. Lett.* **8**, 179 (1966).
89. K.K. Mahavadi, J. Bleuse, X. Chu, and J.P. Faurie, *Appl. Phys. Lett.* **55**, 1285 (1989).
90. V.S. Vavilov and G.L. Nolle, *Sov. Phys. Solid State* **8**, 42 (1966).
91. G.P. Golubev, V.A. Zheleznyakov, S.N. Maksimovskii, E.L. Nolle, and A. Fazylov, *Sov. Phys. Semicond.* **3**, 240 (1969).
92. H.A. Mar and N. Salansky, *J. Appl. Phys.* **56**, 2369 (1984).
93. T.A. Kuhn, W. Ossau, R.N. Bicknell-Tassius, and G. Landwehr, *Appl. Phys. Lett.* **55**, 2637 (1989).

94. J.M. Hays, J.J. Song, and O.K. Wu, *J. Appl. Phys.* **69**, 6612 (1991).
95. P.W. Milonni and J.H. Eberly, *Lasers*, (John Wiley, New York, 1988), pp. 283-287.
96. Rodney Loudon, *The Quantum Theory of Light* (Oxford, Oxford, 1991).
97. K.L. Shaklee, R.E. Nahory, and R.F. Leheny, *J. Lumin.* **7**, 284 (1973).
98. K.L. Shaklee, R.F. Leheny, and R.E. Nahory, *Appl. Phys. Lett.* **19**, 302 (1971).
99. D.E. Cooper, J. Bajaj, and P.R. Newman, *J. Cryst. Growth* **86**, 544 (1988).
100. J. Jacob, Unpublished data.
101. H.L. Cotal, A.C. Lewandowski, B.G. Markey, S.W.S. McKeever, E. Cantwell, and J. Aldridge, *J. Appl. Phys.* **67**, 975 (1990).
102. H. Schweizer and E. Zielinski, *J. Lumin.* **30**, 37 (1985).
103. K. Bohnert, G. Schmieder, and C. Klingshirn, *Phys. Stat. Solidi B* **98**, 175 (1980).
104. M. Voos, R.F. Leheny, and J. Shah, in *Optical Properties of Solids*, edited by M. Balkanski (North-Holland, Amsterdam, 1980), p.329.
105. J.J. Song and W.C. Wang, *J. Appl. Phys.* **55**, 660 (1984).
106. R.A. Reynolds, *J. Vac. Sci. Technol.* **A7**, 269 (1989).
107. R.N. Bhargava, *J. Cryst. Growth* **59**, 15 (1982).
108. P.J. Dean and J.L. Merz, *Phys. Rev.* **178**, 1310 (1969).
109. J.L. Merz, H. Kukimoto, K. Nassau, and J.W. Shiever, *Phys. Rev. B* **6**, 545 (1972).
110. J.L. Merz, K. Nassau, and J.W. Shiever, *Phys. Rev. B* **8**, 1444 (1973).
111. M. Isshiki, T. Kyotani, K. Masumoto, W. Uchida, and S. Suto, *Phys. Rev. B* **36**, 2568 (1987).
112. K. Akimoto, T. Miyajima, and Y. Mori, *Phys. Rev. B* **39**, 3138 (1989).
113. K. Shahzad, D.J. Olego, and D.A. Cammack, *Phys. Rev. B* **39**, 13016 (1989).
114. D.J. Chadi, *Appl. Phys. Lett.* **59**, 3589 (1991).
115. W. Shan, J.M. Hays, X.H. Yang, J.J. Song, E. Cantwell, and J. Aldridge, *Appl. Phys. Lett.* **60**, 736 (1992).

116. G. Cantwell, W.C. Harsch, H.L. Cotal, B.G. Markey, S.W.S. McKeever, and J.E. Thomas, *J. Appl. Phys.* **71**, 2931 (1992).
117. G.C. Hua, N. Otsuka, D.C. Grillo, Y. Fan, J. Han, M.D. Ringle, R.L. Gunshor, M. Hovinen and A.V. Nurmikko, *Appl. Phys. Lett.* **65**, 1331 (1994).
118. Ziqiang Zhu, Hiroshi Mori, Mitsuo Kawashima and Takafumi Yao, *Proc. Sixth Intl. Conf. II-VI Semicond.*, 1991, San Diego, CA, Aug. 1992.
119. Z.Q. Zhu, H. Yoshihara, K. Takebayashi, and T. Yao, *Appl. Phys. Lett.* **63**, 1678 (1993).
120. Ziqiang Zhu, Kazuhisa Takebayashi, Kiyotake Tanaka, Takashi Ebisutani, Junji Kawamata, and T. Yao, *Appl. Phys. Lett.* **64**, 91 (1994).
121. T. Yao, M. Fujimoto, S.K. Chang, and Tanino, *J. Cryst. Growth* **111**, 823 (1991).
122. J.M. Hays, W. Shan, X.H. Yang, J.J. Song, and E. Cantwell, *J. Appl. Phys.* **69**, 6612 (1991).
123. Alexander O.E. Animalu, *Intermediate Quantum Theory of Crystalline Solids* (Prentice Hall, Englewood Cliffs, 1977), ch. 8.
124. K. Seeger, *Semiconductor Physics* (Springer-Verlag, Berlin, 1991), Fifth ed.
125. G. Hitier, B. Canny and J.F. Rommeluere, *J. Physique* **41**, 981 (1980).
126. Sadao Adachi and Tsunemasa Taguchi, *Phys. Rev. B* **43**, 9569 (1991).
127. Charles Kittel, *Introduction to Solid State Physics*, (John Wiley, New York, 1986).
128. Sidney Perkowitz, *Optical Characterization of Semiconductors* (Academic Press, London, 1993).
129. J.R. Haynes, *Phys. Rev. Lett.* **4**, 361 (1960).
130. R.E. Halsted, M. Aven, *Phys. Rev. Lett.* **14**, 64 (1965).
131. S.M. Huang, Y. Nozue, and K. Igaki, *Jpn. J. Appl. Phys.* **22**, L420 (1983).
132. V.I. Sokolov, T.P. Surkova, M.V. Chukichev, and Vu Zoan M'en, *Sov. Phys. Solid State* **26**, 2215 (1984).
133. T. Steiner and M.L.W. Thewalt and R.N. Bhargava, *Solid State Commun.* **56**, 933 (1985).
134. P.J. Dean and D.C. Herbert, *Phys. Rev. B* **23**, 4888 (1981).

135. H.L. Cotal, J.B. Maxson, S.W.S. McKeever, E. Cantwell, *J. Appl. Phys.* **67**, 975 (1990).
136. N. Shibata, A. Ohki, S. Zembutsu, and A. Katsui, *Jpn. J. Appl. Phys.* **27**, L441 (1988).
137. K. Shahzad, J. Petruzzello D.J. Olego, and D.A. Cammack and J.M. Gaines, *Appl. Phys. Lett.* **57**, 2452 (1990).
138. D.J. Robbins, P.J. Dean, P.E. Simmonds and H. Tews, *Deep Centers in Semiconductors* (Gordon and Breach Science Pub., New York, 1986), ed. S.T. Pantelides, ch.11.
139. D.S. Kim, A.J. Fischer, J. Hays, W. Shan, J.J. Song, D.B. Eason, J. Ren, and J.F. Schetzina, *Appl. Phys. Lett.* **65**, 1534 (1994).
140. Bang-fen Zhu, Kun Huang, and Hui Tang, *Phys. Rev. B* **40**, 6299 (1989).
141. P. Lefebvre, B. Gil, and H. Mathieu, *Phys. Rev. B* **9**, 3502 (1974).
142. R.J. Thomas, H.R. Chandrasekhar, M. Chandrasekhar, N. Samarth, H. Luo, and J. Furdyna, *Phys. Rev. B* **45**, 9505 (1992).
143. Akira Shimizu, Tetsuo Ogawa, and Hiroyuki Sakaki, *Phys. Rev. B* **45**, 11338 (1992).
144. M.N. Islam, C.E. Socolich, R.E. Slusher, A.F.J. Levi, W.S. Hobson, and M.G. Young, *J. Appl. Phys.* **71**, 1927 (1992).
145. Christian Mailhot, and Darryl L. Smith, *Sol. Stat. Mat. Sci.* **16**, 131 (1990).
146. Fujio Minami, Yukio Kato, Kouji Yoshida, and Kuon Inoue, *Phys. Rev. Lett.* **67**, 3708 (1991).
147. E. Cantwell, Private communication.
148. R.M. Park, M.B. Troffer, C.M. Rouleau, J.M. DePuydt, M.A. Haase, *Appl. Phys. Lett.* **57**, 2127 (1990).
149. A. Ohki, Y. Kawaguchi, K. Ando, and A. Katsui, *Appl. Phys. Lett.* **59**, 671 (1991).

VITA

JOHN HAYS

Candidate for the Degree of

Doctor of Philosophy

Thesis: LINEAR AND NONLINEAR SPECTROSCOPY OF SELECTED II-VI COMPOUND BULK AND QUANTUM WELL STRUCTURES

Major Field: Physics

Biographical:

Personal Data: Born in Lebanon, Missouri, on October 1, 1962, the son of James and June Hays.

Married Kathy Swallows, July 11, 1992.

Education: Received a Bachelor of Science Degree in Physics and Mathematics from Southwest Missouri State University, Springfield, Missouri in May 1987. Completed requirements for the Doctor of Philosophy Degree at Oklahoma State University in December 1994.

Professional Experience: Research Assistant at Department of Physics, Southwest Missouri State University, Springfield, Missouri, from August 1986 to July 1987; Teaching Assistant at Department of Physics, Oklahoma State University, Stillwater, Oklahoma from August 1987 to July 1988. Research Assistant at Department of Physics, Oklahoma State University from August 1988 to present.

Professional Memberships: American Physical Society, Optical Society of America,  $\Sigma\Pi\Sigma$ , and *KME*.